to Ed Eloranta

THE MEASUREMENT OF RAINFALL BY LIDAR

BY

SCOTT THOMAS SHIPLEY

Scott Thomas Shipley

A thesis submitted in partial fulfillment of the
requirements for the degree of

DOCTOR OF PHILOSOPHY
(Meteorology)

at the

UNIVERSITY OF WISCONSIN-MADISON

1978

THE MEASUREMENT OF RAINFALL BY LIDAR

SCOTT THOMAS SHIPLEY

Under the supervision of Professor James Adolf Weinman

The University of Wisconsin monostatic lidar system is used to measure the spatial distribution of the optical extinction coefficient during rainfall events. A lidar calibration algorithm which estimates the magnitude of the optical extinction coefficient from uncalibrated monostatic lidar signals obtained from rainfall is presented. The results of this calibration technique are compared to simultaneous independent measurements of the total optical depth along the lidar line of sight, and it is shown that this technique determines the magnitude of the optical extinction coefficient from uncalibrated lidar signals to within $\pm$20% of its actual value. RHI depictions of the rainfall optical extinction coefficient are developed with a spatial resolution $\sim$ 15 m using lidar data obtained from the leading edge of a thunderstorm. It is shown that lidar can track subcloud precipitation features as they fall from cloud base to a rain gage located on the surface.

Both the scattering properties of rainfall and the effects of multiple scattering are determined in order to achieve these results. The scattering properties of rainfall are calculated assuming that rain is composed of spherical water drops following the drop size distributions of Marshall and Palmer (1948) and Joss and Gori (1978). It is found that the forward scatter and backscatter phase functions are uniquely related to the optical extinction coefficient and therefore to the rainfall rate. The mean square angles for forward

scattering and backscattering are found to vary in inverse proportion to the mode of the second moment of the drop size distribution. It is also found that the ratio of the mean square angles for forward scattering and backscattering is independent of the detailed structure of the drop size distribution. In addition, the magnitude of the backscatter phase function in the backscatter direction is found to be independent of the magnitude of the optical extinction coefficient. The results of the Mie theory calculations for the scattering properties of large dielectric spheres with real refractive index $\tilde{m} = 1.333$ are summarized.

A general theory for the contribution of Nth order multiple scattering to the return signal of a monostatic lidar is developed using the previous results of Eloranta (1972) and Weinman (1976). This theory applies to non-coaxial lidar systems with Gaussian transmitter beam patterns, and to spatially inhomogeneous media with scattering phase functions which are characterized by the sum of Gaussian functions. Simple formulas for calculating the multiple scattering contribution are developed. These formulas predict the Nth order scattering contribution as a function of the scattering properties of the atmosphere and the lidar system geometry.

Approved _____

Date _____

ACKNOWLEDGEMENTS

I wish to thank Professor James Adolf Weinman for his assistance, sponsorship and contributions during this research effort. I also wish to thank Assistant Professor W. R. Barchet and Professors C. R. Stearns, W. Schwerdtfeger and F. L. Roesler for serving on my committee.

I especially wish to express my deep respect and appreciation for Dr. Edwin W. Eloranta, without whom this thesis would not have been possible. Many of the ideas in this thesis were originated by Dr. Eloranta, particularly in the area of multiple scattering. In particular, Dr. Eloranta created the ray tracing theory for multiple scattering which is presented in Appendix A. The state of the art UW mobile lidar system was designed and built either by him or under his direction. Ed is my guru.

In addition, I wish to thank Dr. K. E. Kunkel and Jeff Sroga for their assistance in obtaining the measurements of chapter 5, and the Space Astronomy Laboratory of the University of Wisconsin for making their computing facilities available for the computations of chapter 2. Special credit is due to Dr. James Greenwood and Michael Zarnstorff for creating the REBEL*BASIC software, and for convincing us to automate the UW lidar with a PDP 11.

This manuscript was typed by Mrs. Judy Swenson.

Finally, I wish to express my sincere appreciation to mom and dad, for whom my love is deep.

This effort was supported under NSF grant ATM 76-21304.

TABLE OF CONTENTS

LIST OF SYMBOLS

A_N	Dimensionless coefficient which explains variation of multiple scattering with lidar geometry, Eq. 3.6
a	fraction of the total scattered energy which is defined by the forward scattering phase function, Eq. 3.2
$\langle a \rangle$	average value of a(x) over the range x = 0 to $R-R_c$
b	slope of the linear distribution of optical extinction coefficient, Eq. 4.9
C'	magnitude of the glory contribution to the backscatter phase function, Eq. 2.9a
$\langle C'(D) \rangle_{MP}$	average value of C' for the M-P drop size distribution, Eq. 2.19b
c	speed of light
D	spherical drop diameter
D_o	drop diameter of the slope discontinuity in the J-G drop size distribution, Eq. 2.14
D_{max}	drop diameter which provides the greatest contribution to the optical extinction coefficient of a spherical polydispersion, Eqs. 2.15
$1-F_j$	a multiple scattering correction factor for the j^{th} atmospheric scattering component, Eq. 4.16
$f(\alpha,\pi)$	a dimensionless backscattering amplitude, Eq. 2.7
H	modified lidar return, Eq. 5.9b
$I,\tilde{I},\bar{I},\hat{I},\hat{\tilde{I}}$	scattered radiances used in the Neumann solution, Eqs. 3.14, 3.15a and 3.30
$\mathbb{I}_o(\ )$	a modified Bessel function, Eq. 3.36

$\hat{i}_n, \hat{\hat{i}}_{n,m}$ two dimensional Fourier transforms of the radiances $\hat{I}$ and $\hat{\hat{I}}$, Eqs. 3.21 and 3.28a

$J_0(\ ), J_1(\ ), J_2(\ )$ zeroth, first and second order Bessel functions of the first kind

$\hat{J}_n, \hat{\hat{J}}_{n,m}$ radiance source terms used in the Neumann solution, Eqs. 3.24c and 3.28b

$\hat{j}$ imaginary one, $\hat{j}^2 = -1$

$K_{ext}(\tilde{m},\alpha)$ extinction efficiency, Eq. 2.2

K_{sca} scattering efficiency, Eq. 2.4a

k_1, k_2 constants for the relationship between β and $P(\pi)$, Eq. 2.24

K_1, K_2, K_3, K_4 constants used in the approximations for the average backscatter phase function, Eq. 4.11b and Fig. 4.4

L lateral separation between the lidar transmitter and receiver

ℓ transverse displacement of scattered radiation from the lidar axis of propagation, Eq. 3.13a

$\tilde{m}$ refractive index

M, m, N, n integers

$N_j(\alpha)$ particle size distribution of the j^{th} atmospheric scattering component, Eq. 1.4

$N_{MP}(D), N_o$ M-P drop size distribution, where N_o is a constant, Eq. 2.10

$N_{JG}(D), N_1, N_2$ J-G drop size distribution, where N_1 and N_2 are constants, Eq. 2.14

P, P_{total} return signal power which is measured by a monostatic lidar

$P_N, P_{n,m}$ N^{th} order multiple scattering components of the return signal power P, Eq. 3.3

$Prob(\ )$ probability function

$\mathbb{P}_k(\tilde{m},\alpha,\Theta)$ phase function for scattering by a single spherical particle, due to diffraction (k = diff), geometrical optics (k = geom) and the glory (k = glory)

$\mathbb{P}(\tilde{m},\Omega)_j$ phase function for scattering by the j^{th} atmospheric scattering component (a polydispersion), Eq. 1.5

$\mathbb{P}_b(\Theta),\mathbb{P}_f(\Theta)$ phase functions for scattering in the backward and forward directions, Eqs. 3.9 and 3.1

$\langle\mathbb{P}(\tilde{m},\alpha,\Theta)\rangle_{\alpha_o}$ phase function for scattering averaged over the size parameter interval α_o to $\alpha_o + \Delta\alpha_d$

$\langle\mathbb{P}_k(\Theta)\rangle_{MP,JG}$ phase function for scattering by the M-P and J-G drop size distributions, for backscattering (k = b) Eqs. 2.19, and diffraction (k = diff) Eq. 2.16a

p Fourier transform coordinate corresponding to y , Eq. 3.21

Q ratio of the mean square angles for forward scattering and backscattering, Eq. 3.10

q Fourier transform coordinate corresponding to z , Eq. 3.21

$\mathbb{R}$ rainfall rate

R range between the lidar and the location of the backscattering event

R_c range between the lidar and the scattering medium boundary

$\tilde{R}$ lidar receiver function, Eq. 3.31

$\tilde{r}$ Fourier transform of the lidar receiver function, Eq. 3.33

r radial displacement of the forward scattered radiation in the backscattering plane, cf. footnote 2, chapter 3

t time

u	dimensionless range, $u = x/(R-R_c)$
W	liquid water content
w_f, w_b	generalized angles for forward scattering and backscattering by a single spherical particle, Eqs. 2.4b and 2.9b
x	penetration depth into the scattering medium
$\tilde{x}$	distance of radiation from an isotropic point source, cf. section A.2
y	cartesian coordinate
y_o	location of the lidar receiver along the y axis
Z	radar reflectivity factor
z	cartesian coordinate
z_o	location of the lidar receiver along the z axis
α	size parameter for a spherical particle
α_o	characteristic size parameter for which an average is performed, viz. average value over the interval $\alpha_o \leq \alpha \leq \alpha_o + \Delta\alpha_d$
α_{max}	size parameter of a polydispersion which corresponds to D_{max}, Eq. 2.16b
β_j	optical extinction coefficient of the j^{th} atmospheric scattering component
β_{eff}	effective optical extinction coefficient $\leq \beta$ due to multiple scattering, Eq. 4.16
$<\beta>$	average value of $\beta(x)$ over the range $x = 0$ to $R-R_c$
β_{MP}, β_{JG}	optical extinction coefficients for the M-P and J-G drop size distributions
β_π	volume backscattering coefficient
$\Gamma(n,)$	incomplete Gamma function

γ_b $\langle\theta_b^2\rangle^{-1}$

γ_f $\langle\theta_f^2\rangle^{-1}$

γ_t $\langle\theta_t^2\rangle^{-1}$

$\Delta\alpha_a, \Delta\alpha_b, \Delta\alpha_c, \Delta\alpha_d$ period in size parameter for four periodic oscillations of the backscatter phase function, Table 2.1

$\Delta\alpha_e$ period in size parameter for the periodic oscillation of the extinction efficiency

$\delta(x-ct)$ Dirac delta function

$\delta_{n,m}$ Kronecker delta function

$\delta\alpha$ size parameter resolution used in the calculation of scattering properties by Mie theory

δt time delay caused by multiple scattering, Eq. 3.14b

$\delta\tau_{eff}$ change in τ_{eff} observed by variation of the receiver field of view, Eq. 5.2

η, η' components of the scattering angle along the y axis

ζ, ζ' components of the scattering angle along the z axis

Θ scattering angle

$\langle\theta_b^2\rangle$ mean square angle for backscattering

$\langle\theta_f^2\rangle$ mean square angle for forward scattering

$\langle\theta_t^2\rangle$ mean square angle of the transmitter beam pattern

θ, θ' scattering angles

κ a constant in the backscatter phase function for a single spherical particle, Eq. 2.9a

Λ	shape parameter for the M-P drop size distribution, Eq. 2.10
Λ_1, Λ_2	shape parameters for the J-G drop size distributions, Eq. 2.14
λ	wavelength
Ξ	modified volume backscattering coefficient, Eq. 5.6
ξ_2	a constant, after Nussenzveig, Eq. 2.6
ρ	normalized spatial distribution of the optical extinction coefficient, Eq. 3.2
$\sigma(\tilde{m},\alpha)$	differential scattering cross section, Eq. 1.3
τ	optical penetration depth, Eq. 3.2
τ_{eff}	effective optical depth $\leq \tau$ due to multiple scattering
Υ	dimensionless receiver field of view, Eq. 3.7a
Φ	ratio of transmitter beam divergence to receiver field of view, Eq. 3.7b
$\phi, \phi', \tilde{\phi}, \varphi$	azimuthal components of the scattering angle
ψ	lidar receiver half width field of view
Ω	solid angle
$\tilde{\omega}$	albedo for single scattering, Eq. 3.12

ACRONYMS

FWHM	Full Width at Half Maximum
JG	Joss and Gori (1978)
MP	Marshall and Palmer (1948)
PPI	Plan Position Indicator
RHI	Range Height Indicator
RTI	Range Time Indicator

Chapter 1

INTRODUCTION

The problems associated with the measurement of the optical extinction coefficient of rain $\beta_r[km^{-1}]$ by monostatic lidar are examined in this thesis, and a method for the derivation of this quantity from conventional lidar return signals is developed. Previous work indicates that the optical extinction coefficient of rain is a direct measure of such rainfall parameters as the rainfall rate $R\,[mm\ hr^{-1}]$ or liquid water content $W\,[g\ m^{-3}]$, cf. Shipley, Eloranta and Weinman (1974). The utility of lidar applications for the study of rainfall and related phenomena is discussed in section 1.1.

The angular structure and magnitude of the atmospheric backscatter phase function, and the effects of multiple scattering must both be either independently measured or theoretically estimated in order to obtain measurements of β_r from conventional lidar information. An extensive numerical calculation of the scattering properties of large dielectric spheres which characterize raindrops was performed by Shipley and Weinman (1978). The results of this study are used to estimate the scattering phase functions for realistic rainfall drop size distributions in chapter 2. Sassen (1977a) experimentally determined

the intensity of light which is backscattered by large water drops in free-fall at terminal velocity, but these measurements were not performed with sufficient angular resolution to resolve the angular structure of backscattering which was needed for the present study.

Solutions to the multiple scattering problem are currently available only for a few special cases. Eloranta (1972) derives an exact solution for the double scattering contribution to a monostatic lidar signal, and Weinman (1976) presents a Neumann solution for the N^{th} order scattering contribution by a medium which is characterized by a multi-Gaussian phase function. The Weinman solution applies to homogeneous media for a coaxial lidar with zero transmitter beam divergence, and because of an error it is valid only for a large receiver field of view (cf. section 3.2). Several Monte Carlo calculations for the contribution of multiple scattering have also been undertaken, but these results serve only to point out the importance of multiple scattering considerations, cf. Plass and Kattawar (1971), Kunkel and Weinman (1976).

A Neumann solution for the N^{th} order scattering contribution to the return signal of a monostatic lidar is presented in chapter 3. This Neumann solution is based upon the results of Eloranta (1972, 1978) and Weinman (1976), and it applies to spatially inhomogeneous media

with multi-Gaussian phase functions for a non-coaxial lidar with finite transmitter beam divergence. Eloranta (1978) recently derived a ray tracing solution for the N^{th} order scattering contribution from an isotropically backscattering medium. This ray tracing solution has not been published, and it is therefore presented in Appendix A (by permission). The Neumann solution of chapter 3 is used to derive a set of simple approximations for the contribution of N^{th} order scattering to monostatic lidar signals in chapter 4. It is shown that the effect of transmitter beam divergence can be neglected when it is less than ~30% of the receiver field of view, as is frequently the case.

The multiple scattering results of chapters 3 and 4 indicate that alteration of the receiver field of view provides a rough estimate of the drop size distribution. A simple receiver field of view experiment was performed to measure the contribution of drops with diameters ~0.1 mm to the total optical depth by distinguishing the spatial and angular spreading of the transmitted beam caused by multiple scattering. The presence of these drops was independently verified by the simultaneous measurement of the drop size distribution by the filter paper technique. The results of this receiver field of view experiment are discussed in chapter 5.

The results of chapters 2, 3 and 4 are applied to the lidar equation to obtain the range variation of the optical extinction coefficient in chapter 5. The β_r solutions are compared to independent estimates of the total optical depth between the UW lidar and a tower mounted calibration target, and it is shown that an uncalibrated monostatic lidar can estimate the optical extinction coefficient of rainfall to within $\pm$20%. The problems associated with the extraction of the rainfall optical extinction coefficient from lidar signals are also discussed in chapter 5.

1.1 The Utility of Lidar in the Investigation of Rainfall

Previous work indicates that the optical extinction coefficient of rain is directly related to such rainfall parameters as the rainfall rate R [mm hr^{-1}] or liquid water content W [g m^{-3}] . Atlas (1953) examined the relationship of visual range to the drop size distribution during rainfall events, and that study predicted a power law relationship of the optical extinction coefficient to both R and W . Shipley, Eloranta and Weinman (1974) directly measured the optical extinction coefficient using lidar signals from spatially homogeneous rainfall over tipping bucket rain gages. A β_r - R power law

relationship which is nearly identical to that of Atlas was obtained, namely

$$\beta_r = 0.16 \pm 0.04 \quad R^{0.74 \pm 0.12} \tag{1.1}$$

Other lidar strategies provide additional information on the properties of rainfall. Derr et al. (1976) and Sassen (1977b) show that the degree of depolarization of lidar signals from precipitation can be used to characterize the precipitation phase. Sassen obtained unambiguous measurements of the phase transition of precipitation from ice to liquid water as it fell through the freezing level in high plains thunderstorms.

The effects of precipitation on the transmission of highly collimated light beams is also of interest. Chu and Hogg (1968) examined the relationship of rain, fog and snow to the attenuation and spreading of laser radiation to determine the limitation imposed on optical communications. Viezee et al. (1969) investigated the feasibility of employing lidar to determine slant range visibility under airfield approach conditions. Each of these studies relies upon a thorough knowledge of the scattering properties of precipitation and the effects of multiple scattering. This thesis seeks to further the understanding of these phenomena.

The combined use of lidar, radar and rain gages may

provide a more accurate measurement of rainfall parameters than when radar and rain gages are used alone. The remote sensing of precipitation by radar relies upon the measurement of the radar reflectivity factor Z [$mm^6\ m^{-3}$] . The reflectivity factor is empirically related to the rainfall rate and the liquid water content by an equation of the form of Eq. 1.1, where the power and proportionality coefficients of the Z-R relationship are empirically determined constants. The appropriate Z-R relationship is usually determined ad hoc by calibrating the radar measurements with a few rain gages as suggested by Wilson (1970). However, in a study on the accuracy of this radar - gage calibration procedure, Puhakka (1978) shows that 5 min accumulations of rainfall can be estimated to at best 33%. As noted by Battan (1976), such factors as the updraft velocity, wind shear and evaporation will modify the Z-R relationship, and these effects may prevent accurate calibrations.

The remote sensing of rainfall may be performed with greater accuracy when measurements are simultaneously obtained at radio and optical wavelengths. The radar reflectivity factor and optical extinction coefficient are proportional to the sixth and second moments of the

drop size distribution, respectively. The theoretical analysis of Atlas and Ulbrich (1974) suggests that Z and β_r are independent measurements of rainfall, and their simultaneous measurement will therefore provide a more accurate determination of both R and W than by radar measurements alone. In addition, an uncalibrated monostatic lidar produces information on the optical extinction coefficient over an extended path length (several km) with a spatial resolution comparable to that of rain gages (several meters). Most radar observations are performed at heights greater than 0.5 km above the surface with spatial resolutions on the order of 0.5 km.[1] Detailed lidar information on the subcloud spatial structure of rainfall is therefore available over sample volumes comparable to those of radar. Subcloud measurements of rainfall by lidar can also be used to trace precipitation as it falls from cloud base to a rain gage located on the surface. The precipitation tracking capability of lidar can be used to assist the intercomparison of rainfall information which is derived from radar and rain gages.

---

[1] For example, the ISWS CHILL 10 and 3 cm dual wavelength radar has a 150 m minimum range resolution with 1 degree horizontal and vertical beam widths, cf. Mueller and Silha (1978).

1.2 The Lidar Equation

Conventional monostatic lidar systems consist of a pulsed laser transmitter and a collimated receiver telescope with suitable photon detection electronics. In general, the transmitter and receiver optical axes are aligned in parallel such that the receiver field of view overlaps a large portion of the transmitted beam. Those photons which are backscattered through π radians by atmospheric scatterers are collected by the receiver telescope and then converted into an electrical signal for analysis. Lidar systems typically employ photomultipliers with digitization electronics at high levels of signal intensity, or with pulse counting circuitry at low levels of signal intensity.

The monostatic lidar equation which describes the return signal as a function of range is

$$P(R) = E_o \frac{cA_{rec}}{R^2} \left[\sum_j \frac{\mathbf{P}(\pi)_j}{4\pi} \beta_j\right] \exp\left[-2 \int_0^R \sum_k (1-F_k)\beta_k dR\right] \quad (1.2)$$

where

E_o	transmitted energy
c	speed of light
A_{rec}	receiver area
R	range
$\mathbf{P}(\pi)_j$	normalized backscatter phase function of the j^{th} atmospheric scattering component

β_j extinction coefficient of the j^{th} scattering component

$1-F_j$ multiple scattering correction factor.

The return power P, the volume backscattering cross section $\beta_\pi = \sum_j \mathbf{P}(\pi)_j \beta_j$ and the effective extinction coefficient $\sum_j (1-F_j) \beta_j$ are general functions of range. Atmospheric scattering components such as molecular gases, haze, fog or rain are considered separately in Eq. 1.2 since the scattering properties of each component are different. A calculation of the normalized scattering phase function for a spherical polydispersion which is characteristic of rainfall is given in chapter 2. A discussion of the multiple scattering correction factor for rain can be found in chapter 4.

The size of a spherical particle can be characterized by the dimensionless size parameter $\alpha = \pi D/\lambda$, where D is the particle diameter and λ is the wavelength of the scattered radiation. Letting $\sigma_j(\tilde{m},\alpha)$ $[m^2]$ represent the total scattering cross section for a single spherical particle with refractive index $\tilde{m}$, then the structure in solid angle Ω[sr] of the scattered intensity is given by the differential scattering cross section $\frac{d\sigma_j(\tilde{m},\alpha)}{d\Omega}$ $[m^2\ sr^{-1}]$. The differential and total scattering cross sections are related by

$$\sigma_j(\tilde{m},\alpha) = \int_{4\pi} \frac{d\sigma_j(\tilde{m},\alpha)}{d\Omega} \cdot d\Omega \quad [m^2] \tag{1.3}$$

where the integral is taken over 4π steradians. Letting $N_j(\alpha)$ $[m^{-3}]$ represent the number concentration of spherical particles with size parameter α, then the volume scattering cross section (or extinction coefficient) for a polydispersion of spherical particles is

$$\beta_j = \int_0^\infty N_j(\alpha)\sigma_j(\tilde{m},\alpha)d\alpha \quad [m^{-1}] \tag{1.4}$$

The phase function for scattering by an ensemble of spherical particles is then defined by

$$\frac{\mathbf{P}(\tilde{m},\Omega)_j}{4\pi} = \frac{1}{\beta_j}\int_0^\infty N_j(\alpha)\frac{d\sigma_j(\tilde{m},\alpha)}{d\Omega}d\alpha \quad [sr^{-1}] \tag{1.5}$$

The parameter $\mathbf{P}(\tilde{m},\Omega)_j$ is called the normalized scattering phase function since the integral of this quantity over all directions is 4π. Referring to the definitions of Deirmendjian (1969), $\mathbf{P}(\tilde{m},\Omega)_j = \frac{1}{2}[\mathbf{P}_1(\tilde{m},\Omega)_j + \mathbf{P}_2(\tilde{m},\Omega)_j]$, where $\mathbf{P}_1(\tilde{m},\Omega)_j$ and $\mathbf{P}_2(\tilde{m},\Omega)_j$ are the first two elements of the Stokes scattering matrix for the j^{th} atmospheric scattering component. Note that the phase function subscripts in this thesis refer primarily to the <u>composition</u> of the atmospheric scattering components.

1.3 Instrumentation

Specifications for the University of Wisconsin mobile lidar facility are given in Table 1.1. A ruby laser transmitter and Pockells cell Q-switch are used to achieve 20 ns pulses of up to 1.5 Joules each at a maximum pulse repitition frequency of 1 s^{-1} . The laser beam is expanded by a Galilean telescope to decrease the output beam width to approximately 1 mrad (FWHM). A photodiode energy monitor is located along the transmitter optic axis to measure the output energy, and this information is recorded on a per shot basis.

An astronomical quality Newtonian telescope is mounted in parallel with the laser transmitter with a transmitter - receiver lateral separation of 0.35 m (1.67 m before 10 Feb 77). The telescope assembly is configured with micrometer adjustment screws to facilitate laser beam mapping and optic axis alignment. The lidar system is also equipped with an automatic scanning capability with allows positioning of the lidar sample volume to 0.1° angular resolution under computer control.

The UW lidar achieves 1 Hz operation through the use of a Digital Equipment PDP 11/40 minicomputer. A highly interactive Lidar Operating System (LOS) is implemented using the BASIC/REBEL software package (©ERDA) of James Greenwood. The BASIC/REBEL system is a real time

Table 1.1

UW Lidar Specifications (1975 to present)

Transmitter	
Wavelength	694.3 nm
Beam divergence	1 mrad (FWHM)
Maximum output energy	1.5 joule
Pulse length	20 ns
Maximum PRF	1 s^{-1}
Transmitter-receiver lateral separation	0.35 m 1.67 m (before 10 Feb 77)
Receiver	
Telescope	0.31 m diameter Newtonian reflector (astronomical quality)
Half width field of view	1 to 5 mrad, adjustable
Interference filter passband	1 nm
Detector	RCA C70024K Photomultiplier Q.E. = 6.8% at 694.3 nm
Video amplifier	Logarithmic, 80 dB dynamic range, 10 MHz
Lidar Scanning	
Elevation	0.0° to 50.0°, computer controlled
Azimuth	0.0° to 90.0°, computer controlled
Angular resolution	0.1°
Data Acquisition System	
A/D conversion	10 bit words, 10 MHz (Biomation 1010) 8 bit words, 10 MHz (American Astrionics 1000, before 1 Jun 77)
Sample time interval	100 ns (15 m range resolution)
Buffer length	1024 words
Minicomputer	DEC PDP 11/40
Software package	BASIC/REBEL (©ERDA)

interpreter, and it allows for real time ordering of lidar related tasks in the form of BASIC subroutines or assembly level code. In addition to data logging, the LOS program performs user defined analysis and display of lidar and supplemental information in real time.

The real time data display capabilities include an A-scope format X-Y CRT and a variable persistence X-Y-Z storage monitor. The storage monitor device is programmed to provide both RHI (Range-Height) and PPI (Plan-Position) display formats. The McIDAS system is also available on an off-line basis for display in high quality false color formats, cf. Smith (1975). Examples of McIDAS generated RHI displays are given in Chapter 5.

The transmission of the atmosphere between a calibration target and the lidar system was obtained along the lidar line of sight. The calibration target consisted of a 7.5 cm diameter bicycle reflector mounted on a radio tower at a range of 2.7 km from the UW lidar. The target was mounted in a protective shroud to prevent any change in target reflectivity due to wetting by rain, and it was located at a height ~30 m above the local terrain. A very large signal was obtained from this target under clear atmospheric conditions, and this signal was reduced to a measureable intensity by inserting neutral density filters into the receiver optical path on alternate lidar

firings. The decrease in the target reflection signal with increasing atmospheric turbidity was used to directly measure the two way total optical depth.

Drop size distributions were obtained at the target site using the filter paper collection technique. The drop collection was accomplished using methylene blue powder on 24 cm diameter blanks of Whatman No. 1 filter paper. This technique provides estimates of the drop size distribution for drop diameters greater than 0.3 mm over time intervals ~1 min. The rainfall rate was also measured at the target site by two Weathermeasure P501 tipping bucket rain gages. The bucket tip events were recorded on strip chart recorders with chart speeds of 15.24 cm hr^{-1} to achieve high temporal resolution.

Chapter 2

THE SCATTERING PROPERTIES OF RAIN

This chapter presents theoretical calculations for the scattering properties of spherical raindrop polydispersions. The scattering properties of rainfall are derived to assist the analysis of lidar signals which are obtained from rain showers. The scattering properties which are particularly relevant to the lidar problem are the total extinction cross section or extinction coefficient, and the angular structure and magnitude of the scattering phase function in the forward and backward scattering directions. The magnitude of the scattering phase function in the backscatter direction is needed to characterize the relationship between the backscattering efficiency and the total extinction cross section. The angular structure of the scattering phase function in the forward and backward scattering directions is needed to characterize the effects of multiple scattering on signals obtained by monostatic lidar systems.

The scattering properties of a single homogeneous spherical particle can be readily calculated using Mie theory. It is assumed in this paper that rainfall is composed of homogeneous spherical particles with real refractive index $\tilde{m} = 1.333$, and the scattering phase

function is then obtained using the Mie theory infinite series solution. Average values of these scattering properties are calculated over finite intervals of droplet size because lidar signals are obtained from droplet populations which are polydisperse. Estimates of the scattering properties of rain are then calculated by convolution of the Mie theory results with the size distributions of Marshall and Palmer (1948) and Joss and Gori (1978).

As shown by Shifrin and Rabinovich (1957) and by Volz (1961), the backscatter phase function magnitude for a spherical water drop due to geometrical optics is $P_{geom}(\tilde{m},\pi) \simeq 0.05 \pm 0.01$. The geometrical optics contribution to backscattering is isotropic in angle from the backscattering direction. However, the backscatter phase function of large water spheres is complicated by an enhanced backscattering phenomenon or "glory", and the backscatter phase function of a large water sphere cannot be described by geometrical optics alone. Fahlen and Bryant (1968) observed the glory from water drops with diameters between 0.6 and 1.5 mm. These authors found good agreement between their observations and the Mie theory predictions for the intensity of the glory ray. The contribution of the glory to backscattering is approximately one order of magnitude greater than that

due to geometrical optics.

An anomalous contribution to backscattering was found by Sassen (1977a) for very large drops which are not spherical in shape. Sassen measured the light which was backscattered by large water drops as they fell through a scattering chamber at terminal velocity. This measurement was not capable of detecting the glory since the scattering cell was configured to accept light which was backscattered at $\pm 2°$ about the backscatter direction. An increase in the backscattering efficiency above the value determined by geometrical optics was observed by Sassen for drops with diameters greater than 4 mm, however. Jones (1959) showed that such large water drops oscillate about a preferred oblate shape, and the mean ratio of principle axes ranges from 0.98 for 2 mm diameter drops to 0.60 for 5 to 6 mm diameter drops. Given a Marshall-Palmer size distribution corresponding to a rainfall rate $R = 100$ mm/hr , the fraction of the optical extinction coefficient which is explained by drops with diameters greater than 4 mm is approximately 4%.[1] The

---

[1] The Marshall-Palmer size distribution is given by Eq. 2.10, where the parameter Λ is related to R by Eq. 2.11. Substituting R=100 mm/hr, Eq. 2.12 can be used to estimate the extinction coefficient fraction $\Delta\beta_{MP}$ which is explained by drops with diameters greater than $D_o' = 4$ mm, such that

$$\Delta\beta_{MP}/\beta_{MP} = \frac{\Lambda^3}{4} \int_{D_o'}^{\infty} \exp[-\Lambda D] D^2 dD = \frac{1}{4} \Gamma\,(3, \Lambda D_o')$$

where Γ is the incomplete Gamma function. It follows that $\Delta\beta_{MP}/\beta_{MP} \sim 0.04$ for $\Lambda \sim 1.8$ mm^{-1} .

backscattering due to non-spherical drops is therefore expected to have a small effect on the optical extinction coefficient, and the effects of droplet nonsphericity are therefore neglected in this paper.

The following two sections summarize Mie theory computations of the scattering properties of large dielectric spheres with real refractive index $\tilde{m} = 1.333$. Mie theory computations for the scattering properties of large water spheres have been performed by other authors, cf. Bryant and Cox (1966), Dave (1968), Fahlen and Bryant (1968). Such studies have been understandably limited in their coverage of scattering properties for very large spheres due to the extensive computing time required for these calculations. Modern scattering theory has been successful in predicting the existence of several periodic oscillations in the backscattering phase function for spherical scatterers, and it has been able to identify the physical effects which are responsible for the glory, cf. Nussenzveig (1969), Khare and Nussenzveig (1977). However, the magnitude for backscattering from large spheres can at present be reliably obtained only from direct calculations by Mie theory.

The computation of phase function average values is complicated by a high degree of variability in the phase function values. As shown by van de Hulst (1957), Bryant

and Cox (1966) and Nussenzveig (1969), however, these phase function undulations are periodic over relatively small intervals of the size parameter. Estimates of phase function average values can therefore be calculated over these periods in size parameter.

The phase function calculations are performed at discrete values of the size parameter. Since the phase function displays high variability with size parameter, meaningful phase function averages can be obtained only when the size parameter resolution is sufficiently high to prevent aliasing. Bryant and Cox (1966) calculated the backscatter phase function with a resolution of $\delta\alpha = 10^{-3}$ at $\alpha = 200$ and 500. Fahlen and Bryant (1968) also calculated the backscatter phase function with the same resolution at $\alpha = 3000$. The results of these authors indicate that a size parameter resolution of $\delta\alpha = 10^{-2}$ is sufficient to resolve the details of the backscatter phase function. Scattering properties are therefore calculated with a resolution of $\delta\alpha = 10^{-2}$ in this study.

The computational procedure utilizes a forward recursion algorithm similar to that of the DAMIE subroutine of Dave (1968). These computations were performed with a FORTRAN program using double precision arithmetic (11 significant decimal digits). The results of this program

and the DAMIE subroutine for a test case with refractive index $\tilde{m} = 1.342$ and size parameter $\alpha = 500\,\pi$ agree to three significant figures. Agreement was also found with the numerical results of Bryant and Cox.

2.1 Comparison with Analytical Approximations

2.1a Extinction Efficiency

Van de Hulst (1957) provides an approximation to the extinction efficiency

$$K_{ext}(\tilde{m},\alpha) = \frac{4\pi}{\lambda^2}\,\frac{\sigma(\tilde{m},\alpha)}{\alpha^2} \tag{2.2}$$

for a homogeneous dielectric sphere with refractive index $1.20 < \tilde{m} < 1.60$ and size parameter $\alpha > 5$. This approximation is

$$K_{ext}(\tilde{m},\alpha) = \mathrm{Re}\{2 - \frac{8\hat{j}\tilde{m}^2}{(\tilde{m}+1)(\tilde{m}^2-1)}\,\alpha^{-1}\,\exp[-2\hat{j}(\tilde{m}-1)\alpha] + 4(0.46-0.8\hat{j})\alpha^{-2/3} + \text{"ripple"}\} \tag{2.3}$$

where $\hat{j}^2 = -1$. The values for $K_{ext}(\tilde{m},\alpha)$ obtained from Mie theory for $\tilde{m} = 1.333$ have been compared to Eq. 2.3 for several size parameter domains in the range $\alpha = 200$ to 4520. The numerical results for K_{ext} near $\alpha \sim 200$, 500, 1000 and 4520 are shown with Eq. 2.3 in Figs. 2.1. These results show a dominant extinction efficiency period

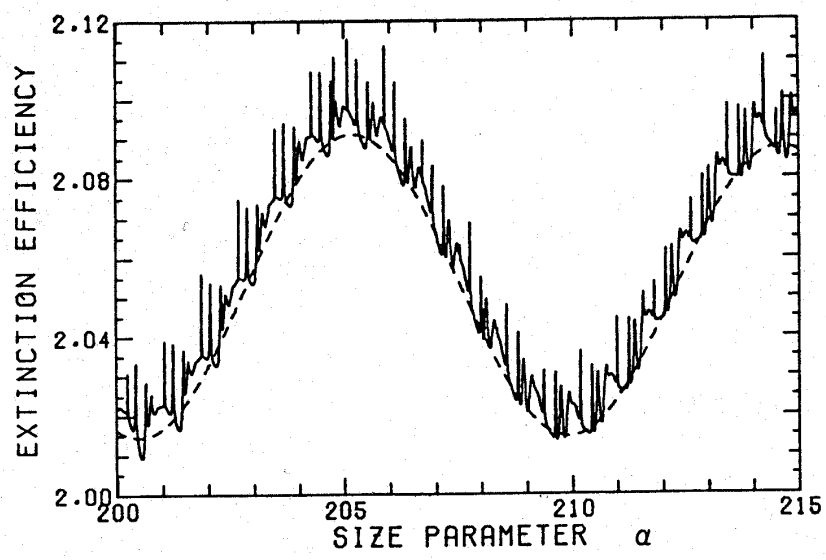

Fig. 2.1a The extinction efficiency $K_{ext}(\tilde{m},\alpha)$ for a homogeneous dielectric sphere with refractive index $\tilde{m} = 1.333$ and size parameters in the range $200 \leq \alpha \leq 215$. The dashed line gives the approximation of van de Hulst (1957), Eq. 2.3.

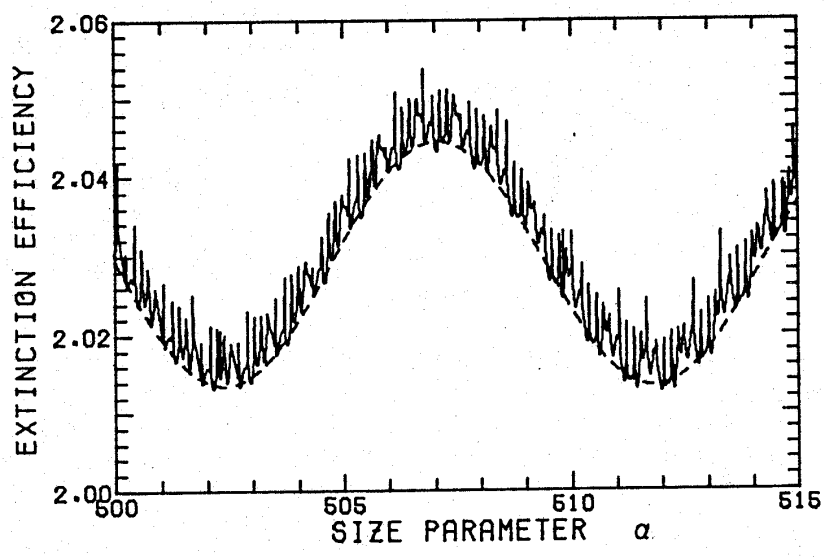

Fig. 2.1b The extinction efficiency for size parameters in the range $500 \leq \alpha \leq 515$.

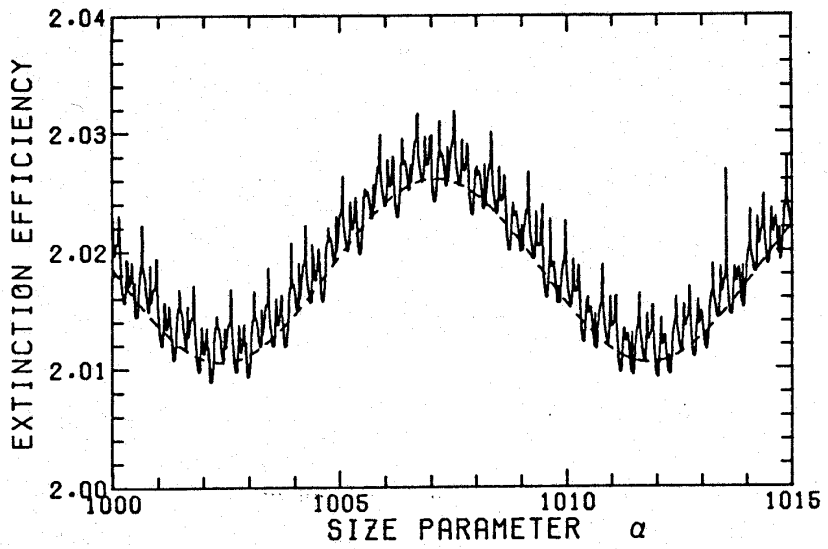

Fig. 2.1c The extinction efficiency for size parameters in the range $1000 \leq \alpha \leq 1015$.

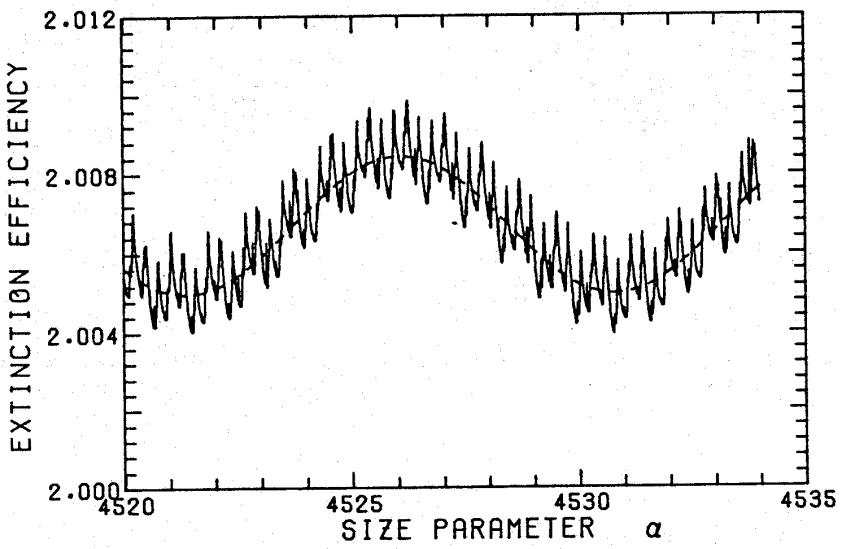

Fig. 2.1d The extinction efficiency for size parameters in the range $4520 \leq \alpha \leq 4535$.

of oscillation of $\Delta\alpha_e = \pi/(\tilde{m}-1)$ for large α. The subscript e is used to identify the size parameter period $\Delta\alpha_e$ with the extinction efficiency. Other subscripts are used to represent periods of oscillation in the backscatter phase function in section 2.2.

2.1b The Diffraction Formula

The normalized phase function for forward scattering from diffraction theory is

$$P_{diff}(w_f) = \frac{4\alpha^2}{K_{sca}} \left[\frac{J_1(w_f)}{w_f}\right]^2 \qquad (2.4a)$$

where

$$w_f = \alpha \sin(\Theta) \qquad (2.4b)$$

and $J_1(w_f)$ is the first order Bessel function of the first kind. K_{sca} represents that portion of the extinction efficiency which is due to scattering only. The numerical results of Mie theory averaged over the interval $\Delta\alpha_e = \pi/(\tilde{m}-1) \simeq 9.4$ for $\tilde{m} = 1.333$ can be compared with the quantity

$$\frac{P_{diff}(w_f)K_{sca}}{\alpha^2} = 4\left[\frac{J_1(w_f)}{w_f}\right]^2 \qquad (2.4c)$$

The calculated forward phase function for $\alpha \sim 500$ and $\alpha \sim 4520$ averaged over the size parameter period $\Delta\alpha_e$

is compared to Eq. 2.4c in Fig. 2.2. The numerical values of Eq. 2.4c at particular values of w_f display a fractional variability in magnitude $\lesssim 10^{-3}$ in the interval $\Delta\alpha_e$.

2.1c Geometrical Optics

Shifrin and Rabinovich (1957) and Volz (1961) have calculated the geometrical optics contribution to scattering from a large homogeneous dielectric sphere. A comparison of the Mie theory results with geometrical optics is given in Fig. 2.3. The geometrical optics results have been shifted downward by a factor of 2 for ease in reading the figure. The Mie theory results have been averaged over the size parameter period $\Delta\alpha_e = \pi/(\tilde{m}-1)$ and they are shown with an angular resolution of 1° for $125° \leq \Theta \leq 145°$ and 5° elsewhere. The geometrical optics results agree with the averaged Mie theory results, but they predict neither the forward diffraction peak nor the glory phenomenon in the backscatter direction.

2.2 The Backscatter Phase Function

2.2a Magnitude of the Glory

The normalized backscatter phase functions for $\alpha \sim 500$ and $\alpha \sim 4520$ are shown in Figs. 2.4 and 2.5. The data of Fig. 2.4 expands the case previously

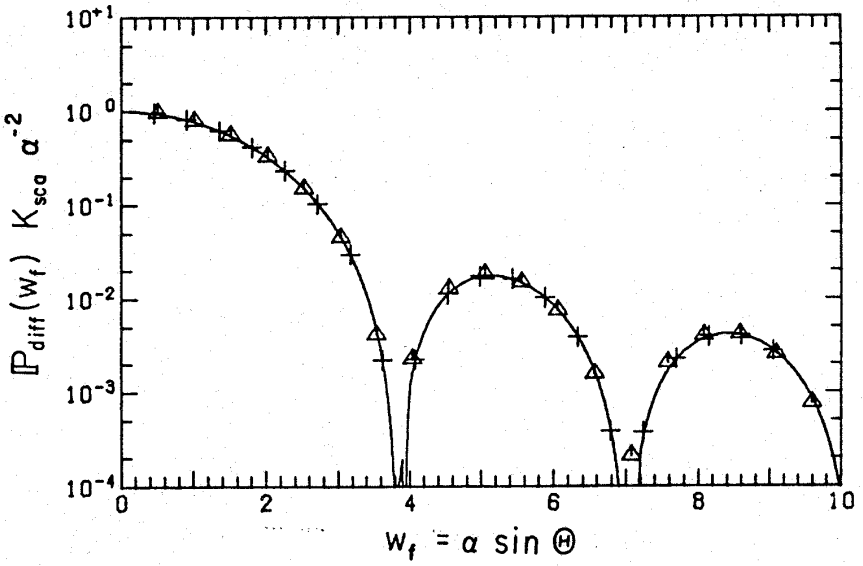

Fig. 2.2 A comparison of the phase function for diffraction (solid, Eq. 2.4c) with the Mie theory results for size parameters near 500 (Δ) and 4520 (+). The numerical results were averaged over the extinction efficiency period $\Delta\alpha_e = \pi/(\tilde{m}-1)$ with $\tilde{m} = 1.333$.

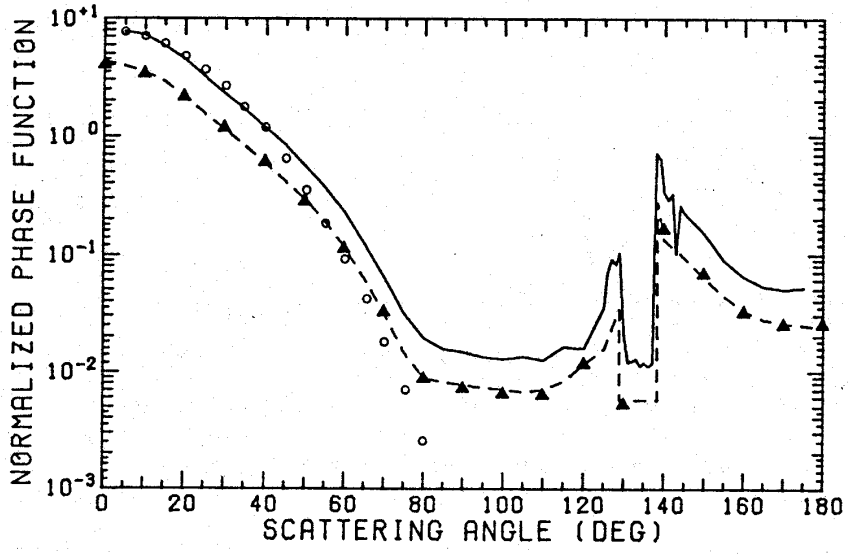

Fig. 2.3 The normalized phase function from geometrical optics according to Shifrin and Rabinovich (1957,▲) and Volz (1961, dash), compared to the Mie theory results for $\alpha_o \sim 4520$ (solid). The geometrical optics results have been divided by two to clarify the comparison. The Mie theory results were averaged over the extinction efficiency period $\Delta\alpha_e = \pi/(\tilde{m}-1)$ for $\tilde{m} = 1.333$. Note that neither the diffraction peak nor glory are shown in this figure. The open circles represent a single Gaussian function approximation to the geometrical optics contribution in the forward direction, cf. Eq. 2.21a.

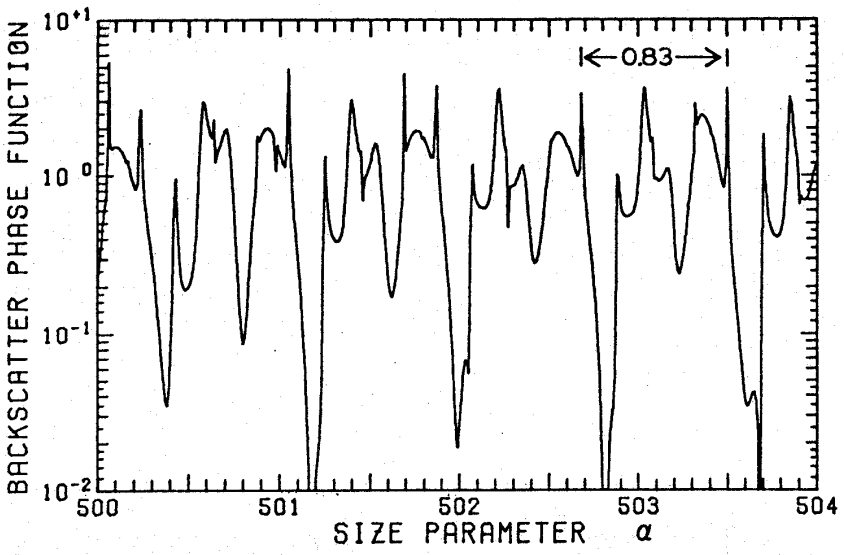

Fig. 2.4 The normalized backscatter phase function for $\tilde{m} = 1.333$ and size parameters near 500, showing the quasi-periodic structure with period $\Delta\alpha_b \simeq 0.83$. This data is an extension of the results of Bryant and Cox (1966).

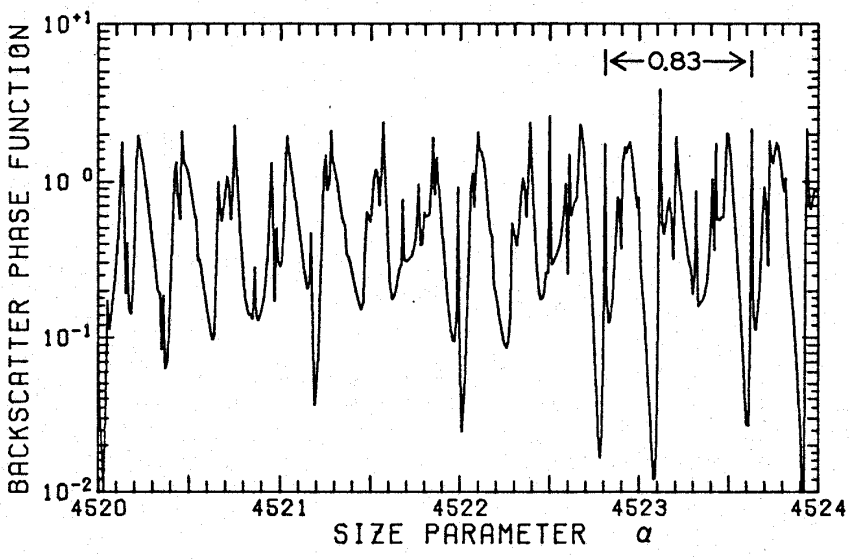

Fig. 2.5 The normalized backscatter phase function for $\tilde{m} = 1.333$ and size parameters near 4520, showing the quasi-periodic structure with $\Delta\alpha_b \simeq 0.83$.

investigated by Bryant and Cox (1966), and it displays the quasi-periodic structure with period $\Delta\alpha_b \simeq 0.83$ which was reported by these authors. The data of Fig. 2.5 shows a much more complicated backscattering structure in size parameter, although that structure is also quasi-periodic and the period $\Delta\alpha_b \simeq 0.83$ is evident.

A search for periods of oscillation in the backscatter phase function other than $\Delta\alpha_b \simeq 0.83$ was performed. A running mean in size parameter of the backscatter phase function was taken with an averaging interval of $\Delta\alpha_b = 0.83$. The resulting average normalized backscatter phase function for $500 \leq \alpha \leq 550$ and $\tilde{m} = 1.333$ is shown in Fig. 2.6. Two quasi-periodic oscillations with periods of $\Delta\alpha_c \simeq 1.1$ and $\Delta\alpha_d \simeq 14$ are apparent in Fig. 2.6. A Fourier transform of the unsmoothed data was performed to estimate the amplitudes of these periodic oscillations. A discrete Fourier transform determines the coefficients $\tilde{A}_n$ and $\tilde{B}_n$ of the backscatter phase function expansion

$$P(\tilde{m},\alpha,\pi) = \frac{1}{2}\tilde{A}_o + \sum_{n=1}^{M}\left[\tilde{A}_n \cos\left(\frac{2\pi\alpha}{\Delta\alpha_n}\right) + \tilde{B}_n \sin\left(\frac{2\pi\alpha}{\Delta\alpha_n}\right)\right] \qquad (2.5a)$$

where

$$\Delta\alpha_n = n\delta\alpha \qquad (2.5b)$$

is the period of each oscillation and $\delta\alpha$ is the size parameter resolution of the data set. The spectra of the

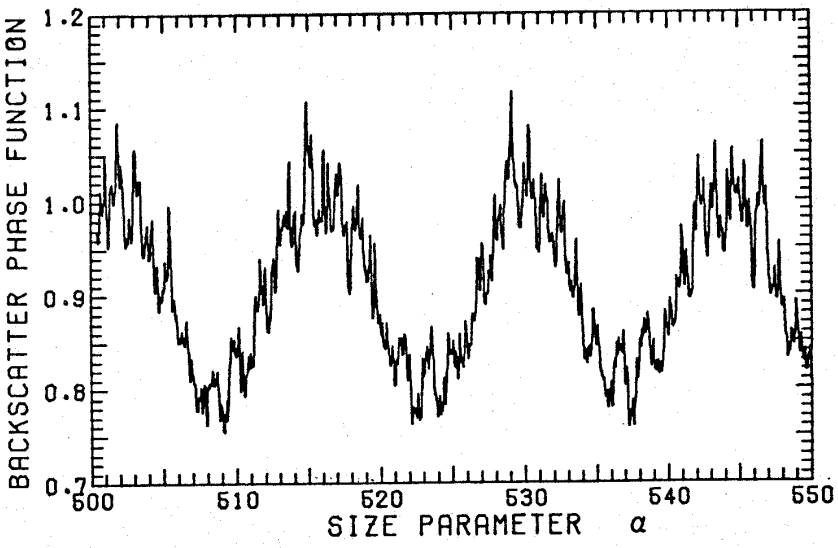

Fig. 2.6 Running mean of the normalized backscatter phase function for size parameters near 500. The running mean was taken over the averaging interval $\Delta\alpha_b \simeq 0.83$. Two periodic oscillations with periods $\Delta\alpha_c \simeq 1.1$ and $\Delta\alpha_d \simeq 14$ are apparent.

average amplitude $\tilde{C}_n = (\tilde{A}_n^2 + \tilde{B}_n^2)^{1/2}$ for $\alpha_o \leq \alpha \leq \alpha_o + 2\Delta\alpha_d$ are shown in Figs. 2.7 as a function of the size parameter period of oscillation $\Delta\alpha_n$ for several values of α_o. The spectra of Figs. 2.7a through 2.7h demonstrate the presence of backscatter phase function oscillations with periods $\Delta\alpha_a \simeq 0.41$, $\Delta\alpha_b \simeq 0.83$, $\Delta\alpha_c \simeq 1.1$ and $\Delta\alpha_d \simeq 14$. The average amplitudes for these four periods of oscillation are given in Table 2.1 for several size parameter intervals in the range $200 \leq \alpha \leq 3000$. Note that the amplitudes of these oscillations decreases with increasing size parameter.

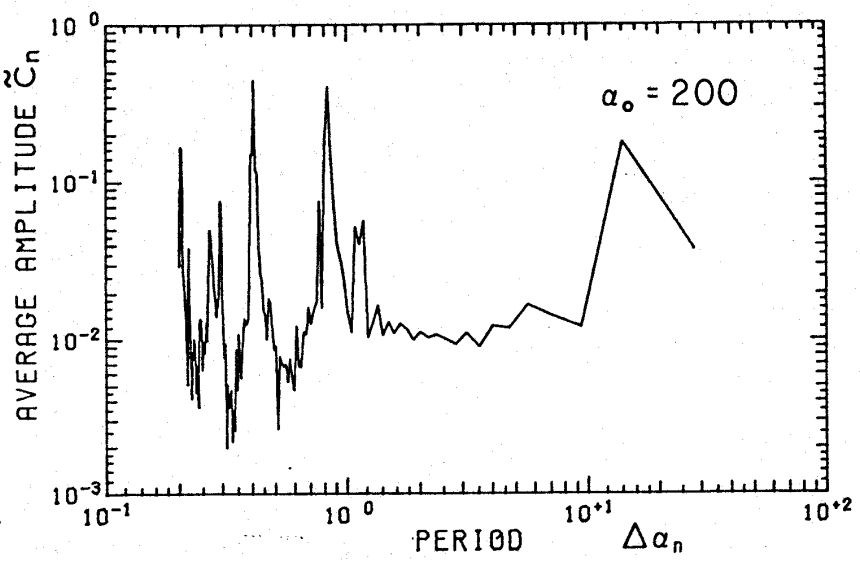

Fig. 2.7a Average amplitude spectrum $\tilde{C}_n$ as a function of the period $\Delta\alpha_n$ of the Mie theory results for back-scattering with $200 \leq \alpha \leq 228$.

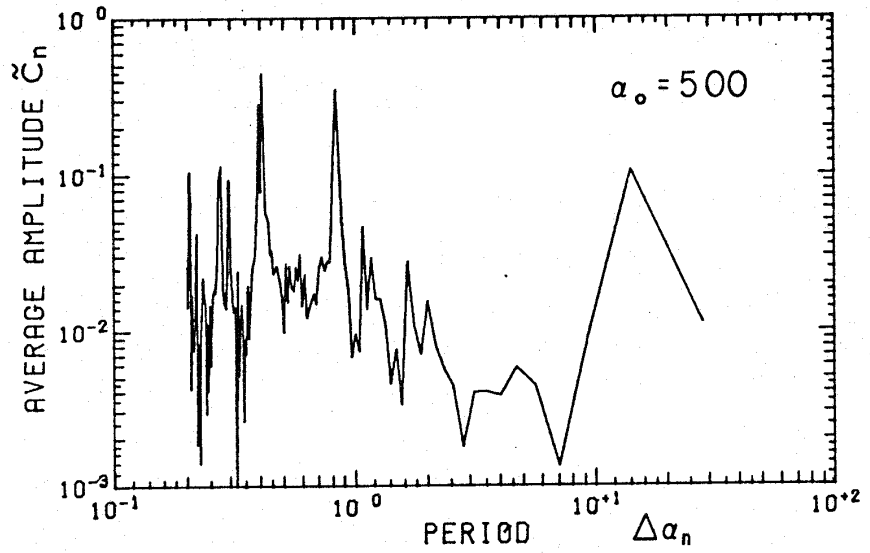

Fig. 2.7b Average amplitude spectrum $\tilde{C}_n$ as a function of the period $\Delta\alpha_n$ of the Mie theory results for back-scattering with $500 \leq \alpha \leq 528$.

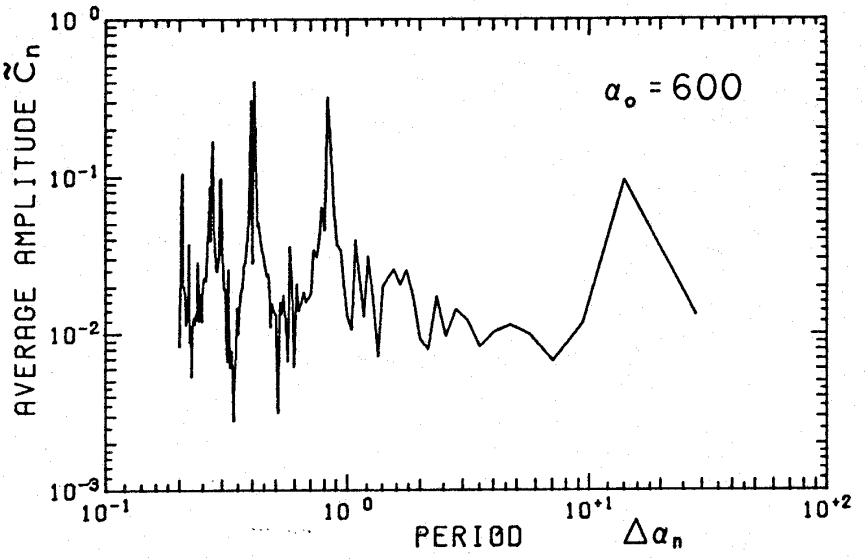

Fig. 2.7c Average amplitude spectrum $\tilde{C}_n$ as a function of the period $\Delta\alpha_n$ of the Mie theory results for back-scattering with $600 \leq \alpha \leq 628$.

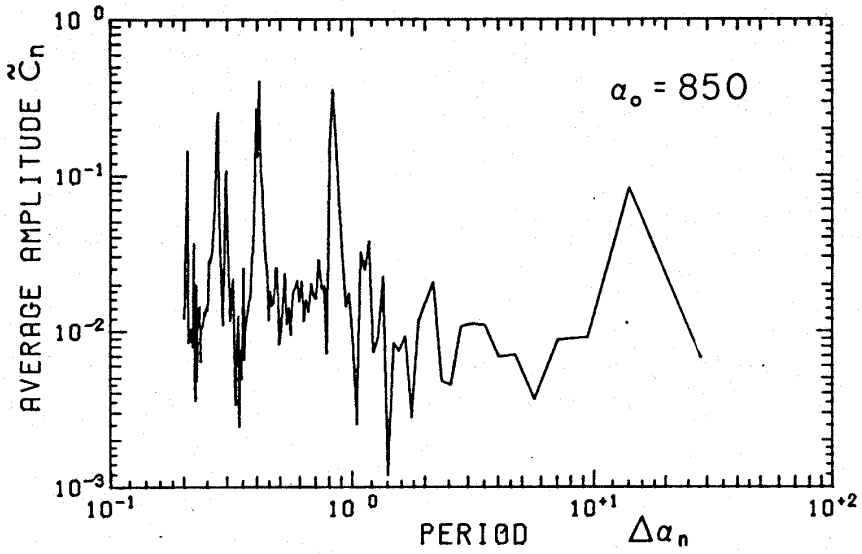

Fig. 2.7d Average amplitude spectrum $\tilde{C}_n$ as a function of the period $\Delta\alpha_n$ of the Mie theory results for back-scattering with $850 \leq \alpha \leq 878$.

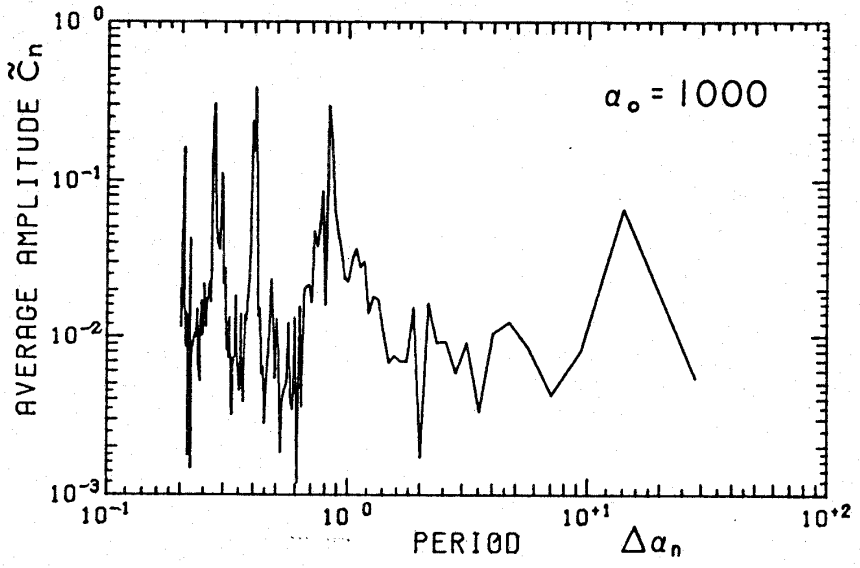

Fig. 2.7e Average amplitude spectrum $\tilde{C}_n$ as a function of the period $\Delta\alpha_n$ of the Mie theory results for back-scattering with $1000 \leq \alpha \leq 1028$.

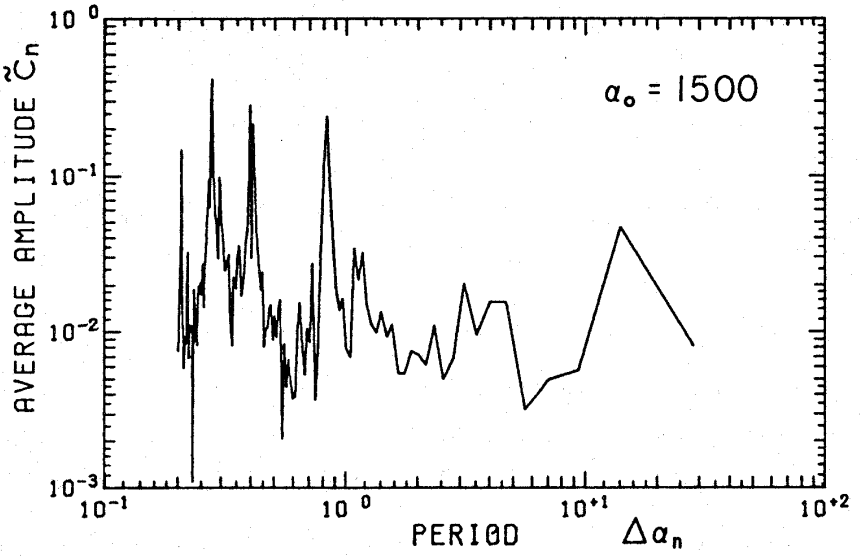

Fig. 2.7f Average amplitude spectrum $\tilde{C}_n$ as a function of the period $\Delta\alpha_n$ of the Mie theory results for back-scattering with $1500 \leq \alpha \leq 1528$.

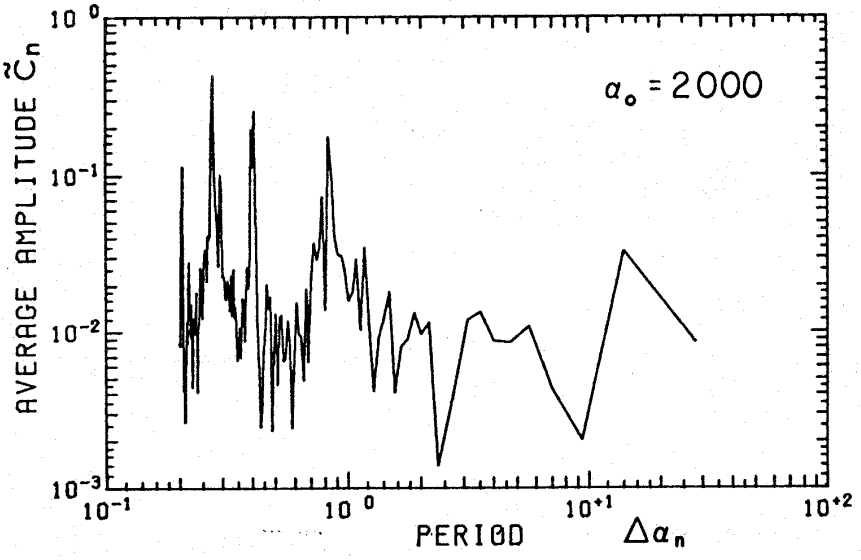

Fig. 2.7g Average amplitude spectrum $\tilde{C}_n$ as a function of the period $\Delta\alpha_n$ of the Mie theory results for back-scattering with $2000 \leq \alpha \leq 2028$.

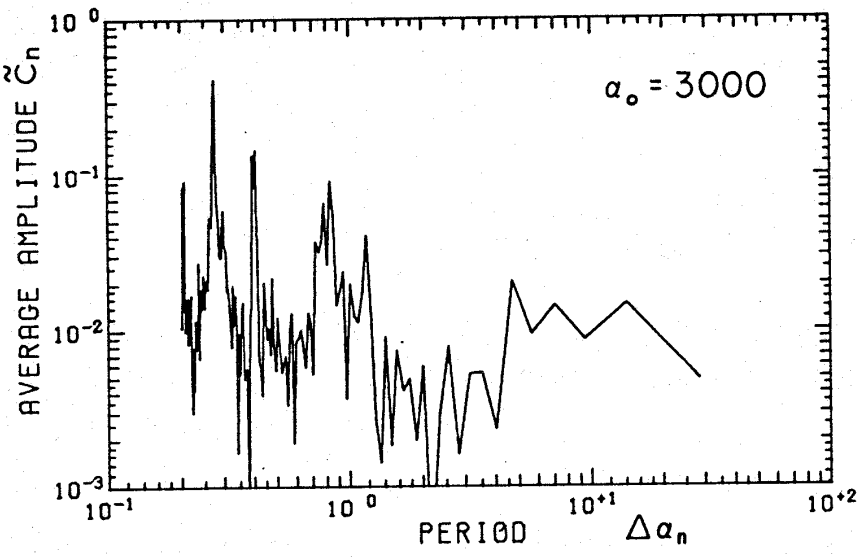

Fig. 2.7h Average amplitude spectrum $\tilde{C}_n$ as a function of the period $\Delta\alpha_n$ of the Mie theory results for back-scattering with $3000 \leq \alpha \leq 3028$.

TABLE 2.1

Average Amplitudes for the Normalized Backscatter Phase Function for $\tilde{m} = 1.333$ in Several Size Parameter Ranges

	Normalized Backscatter Phase Function Amplitudes					
α_o	Average Value[a] $\langle P(\tilde{m},\alpha,\pi)\rangle_{\alpha_o}$	$\tilde{C}_a$ for $\Delta\alpha_a \simeq .41$	$\tilde{C}_b$ for $\Delta\alpha_b \simeq .83$	$\tilde{C}_c$ for $\Delta\alpha_c \simeq 1.1$	$\tilde{C}_d$ for $\Delta\alpha_d \simeq 14$	C' of Eq. 2.9a
200	0.72 ± .02	0.45	0.41	0.052	0.18	0.55 ± .07
500	0.90 ± .01	0.45	0.35	0.047	0.11	0.70 ± .07
600	0.923 ± .008	0.41	0.32	0.040	0.095	0.72 ± .07
850	0.943 ± .006	0.40	0.36	0.032	0.083	0.74 ± .07
1000	0.928 ± .005	0.39	0.30	0.037	0.065	0.73 ± .07
1500	0.860 ± .005	0.22	0.24	0.034	0.047	0.67 ± .07
2000	0.781 ± .005	0.26	0.18	0.030	0.033	0.60 ± .07
3000	0.673 ± .005	0.15	0.092	ND[b]	ND[b]	0.51 ± .07
4520[c]	0.636 ± .005	--	--	--	--	0.48 ± .07

[a] Average values are determined over size parameter intervals from α_o to $\alpha_o + 2\Delta\alpha_d$.

[b] The amplitudes $\tilde{C}_c$ and $\tilde{C}_d$ are not detected (ND) for $\alpha_o \simeq 3000$.

[c] The $\alpha_o \simeq 4520$ data was obtained in the interval from α_o to $\alpha_o + \Delta\alpha_d$, and a Fourier transform was not taken.

Nussenzveig (1969) used a modified Watson transformation for $\alpha^{1/3} >> 1$ and $1 < \tilde{m} < \sqrt{2}$ to theoretically approximate the rainbow and the glory for a transparent homogeneous sphere. Nussenzveig showed that the period $\Delta\alpha_b$ of the backscatter oscillation for large α is approximately [his Eq. 6.73, p. 162]

$$\Delta\alpha_b = \frac{\pi}{4(\tilde{m}^2-1)^{1/2}+\xi_2} = .83 \tag{2.6}$$

where the parameter $\xi_2 \simeq 0.262$ for $\tilde{m} = 1.330$ has a weak dependence on α. Nussenzveig also derived a dimensionless backscattering amplitude $f(\alpha,\pi)$ in the form of a Taylor expansion about some large size parameter α_o for $\tilde{m} = 1.330$ such that [his Eq. 5.27, p 152]

$$f(\alpha-\alpha_o,\pi) \simeq \hat{A}\{1 + \hat{B}\exp[-0.45\,\hat{j}\,(\alpha-\alpha_o)] + \hat{C}\exp[-5.77\,\hat{j}\,(\alpha-\alpha_o)]\} \tag{2.7}$$

where $\hat{A}$, $\hat{B}$, $\hat{C}$ are complex parameters which are functions of α_o but which remain relatively constant in the size parameter interval $(\alpha-\alpha_o) << \alpha_o$. Eq. 2.7 predicts that the backscatter phase function undergoes periodic oscillations in size parameter with periods

$$\Delta\alpha_c \simeq \frac{2}{5.77} = 1.1 \tag{2.8a}$$

and

$$\Delta\alpha_d \simeq \frac{2\pi}{0.45} = 14\ . \tag{2.8b}$$

Even though the Nussenzveig theory was applied to computations of the lowest order terms of the Debye expansion of the Mie theory solution, his prediction of the two backscattering periods $\Delta\alpha_c$ and $\Delta\alpha_d$ is verified by the present results.

The averaged normalized backscatter phase function is shown in Fig. 2.8 as a function of the size parameter. The backscatter phase function was averaged over the interval $\Delta\alpha_d$. The vertical bars represent the standard deviation of the backscatter phase function magnitude in the interval $\Delta\alpha_d$. The data of Fig. 2.8 show a systematic variation of the average magnitude for backscattering, with a distinct maximum near $\alpha_o \sim 10^3$. These average values are presented in Table 2.1.

2.2b Angular Structure of the Glory

Van de Hulst (1957, pp 249-258) presents an asymptotic approximation based upon the Debye expansion of the Mie theory solution which estimates the angular structure of the backscattering phase function. Only those terms with orders near the value of the size parameter are retained, which implies that this approximation considers only the contribution of "surface waves" to the scattering amplitudes. The result of van de Hulst is modified such that the average value of the normalized phase function near

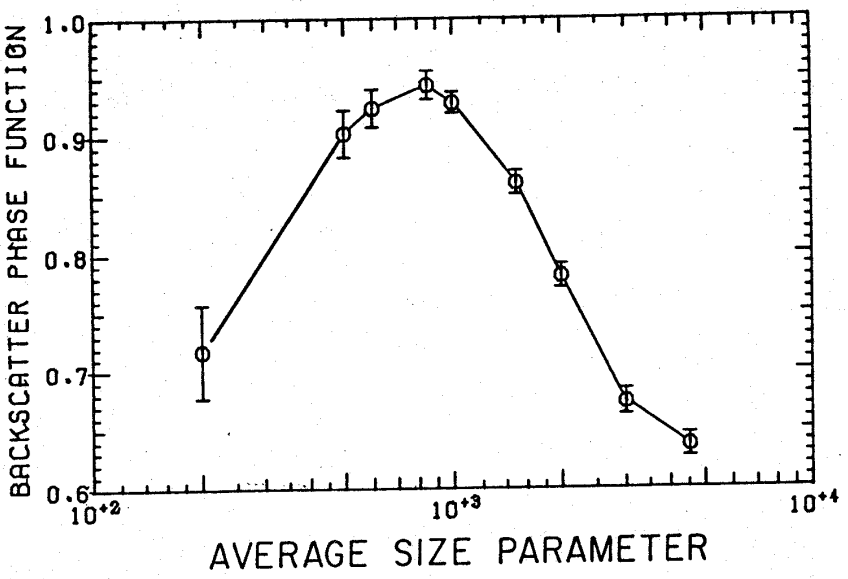

Fig. 2.8 Magnitude of the normalized backscatter phase function averaged over the size parameter interval $\Delta\alpha_d = 14$, as a function of size parameter.

the backscattering angle in a size parameter interval $\Delta\alpha \ll \alpha_o$ is

$$\langle \mathbb{P}(\tilde{m},\alpha,\Theta\rangle_{\alpha_o} = \mathbb{P}_{geom}(\tilde{m},\pi) + C'\{(1+\kappa)^2 J_o^2(w_b)+(1-\kappa)^2 J_2^2(w_b)\} \qquad (2.9a)$$

where

$$w_b = \alpha \sin(\pi-\Theta) \qquad (2.9b)$$

and where C' and κ are undetermined constants. $J_o(w_b)$ and $J_2(w_b)$ are the zero and second order Bessel functions of the first kind. The term $\mathbb{P}_{geom}(\tilde{m},\pi)$ accounts

for the contribution of geometrical optics to backscattering.

The numerical results for the angular structure of the averaged backscatter phase function for $\alpha_o \sim 500$ and $\alpha_o \sim 4520$ are shown in Fig. 2.9. The phase function was averaged over one cycle of the backscatter oscillation period $\Delta\alpha_d = 14$. These results can be represented by Eq. 2.9a when the contribution of geometrical optics to backscattering is $P_{geom}(\tilde{m},\pi) \simeq 0.05 \pm 0.005$. This value for the geometrical optics contribution is identical to that determined by Shifrin and Rabinovich (1957) and by Volz (1961).

A least squares regression of Eq. 2.9a with the averaged numerical results gives a constant value for κ such that $\kappa = 0.10 \pm 0.05$ for all $\alpha_o \gtrsim 500$. This result suggests that the average backscatter phase function can be represented by Eq. 2.9a for large spheres with refractive index $\tilde{m} = 1.333$, $P_{geom}(\tilde{m},\pi) \simeq 0.05$ and $\kappa \simeq 0.10$ for $\alpha_o \gtrsim 500$. Values for the constant C' of Eq. 2.9a were also determined, and they are included in Table 2.1.

2.3 Summary of the Scattering Properties of a Large Dielectric Sphere

The approximations of van de Hulst (1957) for the

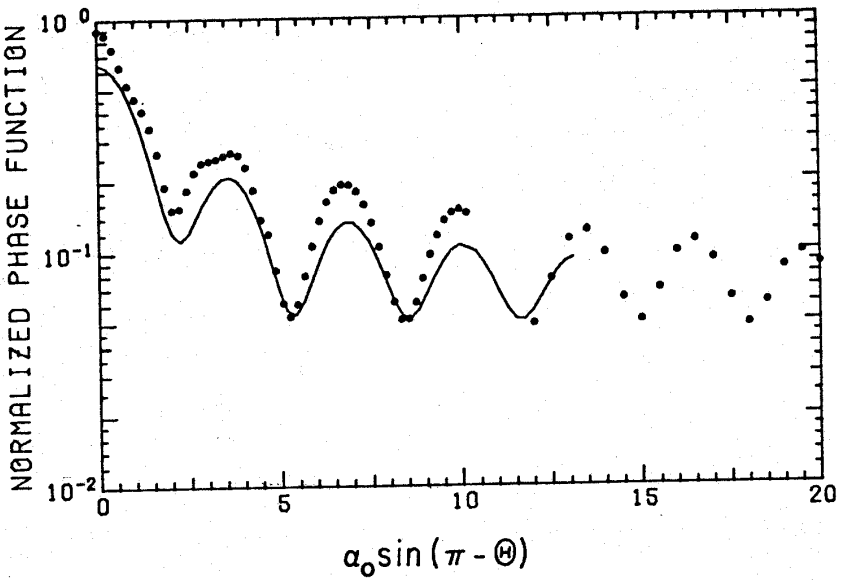

Fig. 2.9 Angular variation of the average normalized backscatter phase function for $\alpha_o \sim 500$ (dots) and $\alpha_o \sim 4520$ (solid). The phase function was averaged over the backscattering oscillation period $\Delta\alpha_d = 14$.

extinction efficiency [Eq. 2.3] and the angular structure of the glory [Eq. 2.9a] agree with the Mie theory results for the scattering properties of large homogeneous dielectric spheres with real refractive index $\tilde{m} = 1.333$. For $\alpha_o \sim 4520$, the phase function of geometrical optics agrees with the Mie theory phase function values, except in the vicinity of the forward diffraction peak and the glory. The average backscatter phase function calculations indicate that the glory can be represented by Eq. 2.9a for $500 \leq \alpha_o \leq 4520$ and $\tilde{m} = 1.333$, with $P_{geom}(\tilde{m},\pi) \simeq 0.05 \pm 0.005$ and $\kappa \simeq 0.10 \pm 0.05$. The factor C' of Eq.

2.9a is a function of the size parameter, and representative values of this proportionality factor are given in Table 2.1. It was found that the average backscatter phase function reaches a maximum near $\alpha_o \sim 10^3$ for $\tilde{m} = 1.333$.

These results demonstrate the existence of a large contribution to backscattering by non-geometrical optics sources for non-absorbing spheres with size parameters up to $\alpha_o \approx 4520$. The angular width of this contribution diminishes in inverse proportion to the size parameter, and its importance to backscattering measurements will therefore depend upon the geometry of the measuring instrument. The non-geometrical optics components of the forward scatter and backscatter phase functions for a monodispersion of spherical scatterers are shown in Fig. 2.10. These scattering phase functions are normalized to unity in the forward and backward directions, and the abscissa is given in terms of the dimensionless angles $\alpha_o \sin(\Theta)$ for forward scattering and $\alpha_o \sin(\pi-\Theta)$ for backscattering.

2.4 The Scattering Phase Function for Rainfall

The rainfall scattering phase function is computed in this section by convoluting the spherical particle phase function for a single droplet with the drop size

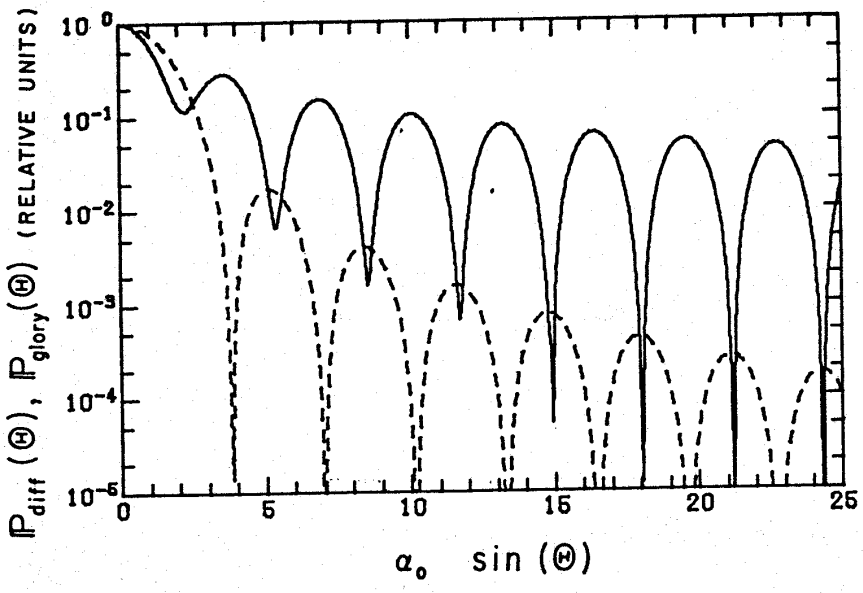

Fig. 2.10 Relative angular variation of the non-geometrical optics components of the forward scatter (dash) and backscatter (solid) phase functions. The abscissa is given in terms of $\alpha_o \sin(\Theta)$ for forward scatter and $\alpha_o \sin(\pi-\Theta)$ for backscatter.

distributions of Marshall and Palmer (1948) and Joss and Gori (1978). The phase functions for forward scattering and backscattering are calculated by convolution of these drop size distributions with the phase function results of sections 2.1 and 2.2. A summary of the resulting averages for the scattering phase function of rainfall is presented in section 2.5.

The Marshall-Palmer (M-P) drop size distribution for rainfall is

$$N_{MP}(D) = N_o \exp[-\Lambda D] \tag{2.10}$$

where D [mm] is drop diameter, Λ [mm^{-1}] is a shape factor which varies with either the rainfall rate R [$mm\ hr^{-1}$] or the optical extinction coefficient of rain β_r [km^{-1}], and $N_o = 8000\ m^{-3}mm^{-1}$ is a constant. The shape factor Λ of the M-P size distribution is empirically related to the rainfall rate by

$$\Lambda = 4.1\ R^{-0.21} \tag{2.11}$$

The optical extinction coefficient of the M-P size distribution is given by

$$\beta_{MP} = \int_0^\infty N_{MP}(D) K_{sca} \frac{\pi D^2}{4}\, dD = \pi N_o \Lambda^{-3} \tag{2.12}$$

where $K_{sca} = 2$. It therefore follows that the shape factor Λ is related to β_{MP} by

$$\Lambda = \left(\frac{\pi N_o}{\beta_{MP}}\right)^{-1/3} \tag{2.13}$$

As discussed by Joss and Gori (1978), the M-P drop size distribution applies to measured drop spectra when these size distributions are accumulated over long time intervals or large volumes under differring rainfall conditions. Joss and Gori obtained the "instantaneous" size distribution over one minute sequential time intervals

using the Distromet RD-69 Size Distrometer. The averages of one minute distributions obtained at $R = 1$, 10 and 100 mm hr^{-1} during thunderstorm rain at Locarno, Switzerland on 14 July, 1974 depart significantly from Eq. 2.10, however. These "instantaneous" measured distributions can be adequately modeled by pairs of exponential functions, such that

$$N_{JG}(D) = \begin{cases} N_1 \exp(-\Lambda_1 D); & D \leq D_o \\ N_2 \exp(-\Lambda_2 D); & D > D_o \end{cases} \qquad (2.14)$$

Values for $N_1, N_2, \Lambda_1, \Lambda_2$ and D_o can be obtained directly from Joss and Gori (1978) [their Fig. 2], and these values are given in Table 2.2 as a function of the rainfall rate. The resulting size distributions $N_{JG}(D)$ for the Joss and Gori (J-G) data are shown in Fig. 2.11 together with the corresponding size distributions of Marshall and Palmer at $R = 1$, 10 and 100 mm hr^{-1}.

It is useful to characterize the rainfall scattering phase function as though it were produced by a monodispersion of raindrops having some characteristic size. The drop diameter D_{max} which gives rise to the greatest contribution to the total optical extinction of a droplet polydispersion can be used as the characteristic drop size. The maximum contribution to optical extinction by the M-P drop size distribution occurs at the drop

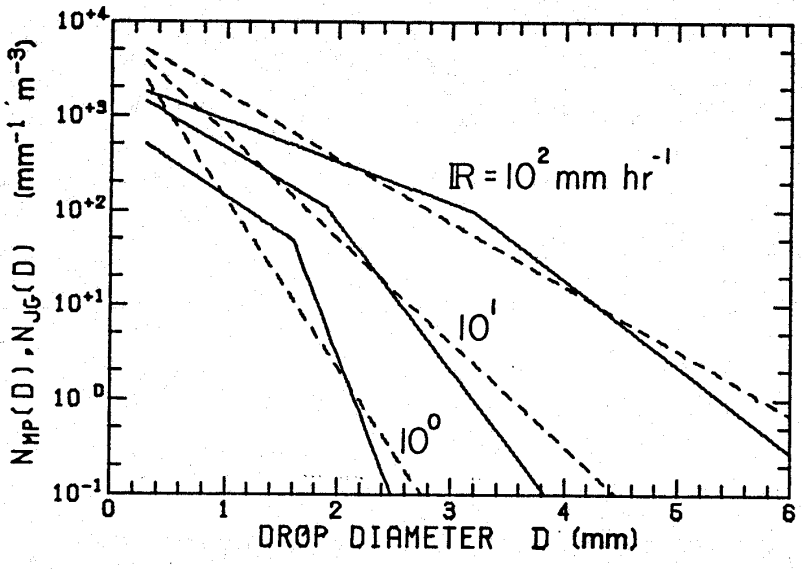

Fig. 2.11 The "instantaneous" size distributions of Joss and Gori (1978, solid). These size distributions were measured over one minute time intervals in thunderstorm rain at rainfall rates of 1, 10 and 100 mm hr^{-1}. The Marshall-Palmer size distributions of Eq. 2.10 (dash) are shown at the same rainfall rates for comparison.

TABLE 2.2

Values of the Parameters for the Size Distribution of Joss and Gori (1978)

R	D_o	D_{max}	N_1	N_2	Λ_1	Λ_2
(mm hr^{-1})	(mm)	(mm)	($mm^{-1}m^{-3}$)	($mm^{-1}m^{-3}$)	(mm^{-1})	(mm^{-1})
1	1.6	0.83	843	3.5E+6	1.8	7.0
10	1.9	1.02	2240	1.0E+5	1.6	3.6
100	3.2	1.67	2400	8.1E+4	1.0	2.1

diameter

$$D_{max} = 2\Lambda^{-1} \qquad \text{(M-P)} \tag{2.15a}$$

As proposed by Joss and Gori, the mode of the second moment of measured drop size distributions can be approximated by

$$D_{max} = \frac{\int_0^\infty N(D)D^2dD}{\int_0^\infty N(D)DdD} \tag{2.15b}$$

The value of D_{max} for the measured distributions of Joss and Gori can be calculated using Eqs. 2.14 and 2.15b with reference to Table 2.2. The resulting values for D_{max} for the J-G size distributions are included in Table 2.2.

The forward scattering phase function of a polydispersion due to diffraction using the small angle approximation is

$$\langle P_{diff}(\alpha_{max}\Theta)\rangle = \frac{1}{\beta_r}\int_0^\infty N(D)K_{sca}\frac{\pi D^2}{4}P_{diff}(w_f)dD \tag{2.16a}$$

where w_f is given by Eq. 2.4b, and

$$\alpha_{max} = \frac{\pi D_{max}}{\lambda} \tag{2.16b}$$

The forward scattering phase function for diffraction can be obtained for the M-P size distribution by substituting Eqs. 2.4a and 2.10 into Eq. 2.16a, such that

$$\langle P_{diff}(\alpha_{max}\Theta)\rangle_{MP} = \frac{8}{\alpha_{max}^3\Theta^5}\int_0^\infty \exp(-2\frac{w_f}{\alpha_{max}\Theta})\, w_f^2\, J_1^2(w_f)dw_f \qquad (2.17)$$

The value of the scattering phase function for diffraction in the forward direction by the M-P size distribution is then

$$\langle P_{diff}(\Theta=0)\rangle_{MP} = \frac{3}{2}\alpha_{max}^2 = \frac{6\pi^2}{\lambda^2}\Lambda^{-2} \qquad (2.18)$$

The universal diffraction phase function of the M-P size distribution is shown as a function of the generalized angle $\alpha_{max}\Theta$ in Fig. 2.12. The diffraction phase function for the J-G size distributions can be similarly calculated using Eq. 2.16a. The results for R = 1, 10 and 100 mm hr^{-1} are included in Fig. 2.12 for comparison to the universal M-P diffraction phase function. The diffraction phase functions of the J-G size distributions differ from the M-P diffraction phase function for scattering angles near zero, but these phase functions agree elsewhere. These results imply that the peak value of the diffraction phase function at zero scattering angle will not be known for real size distributions unless these

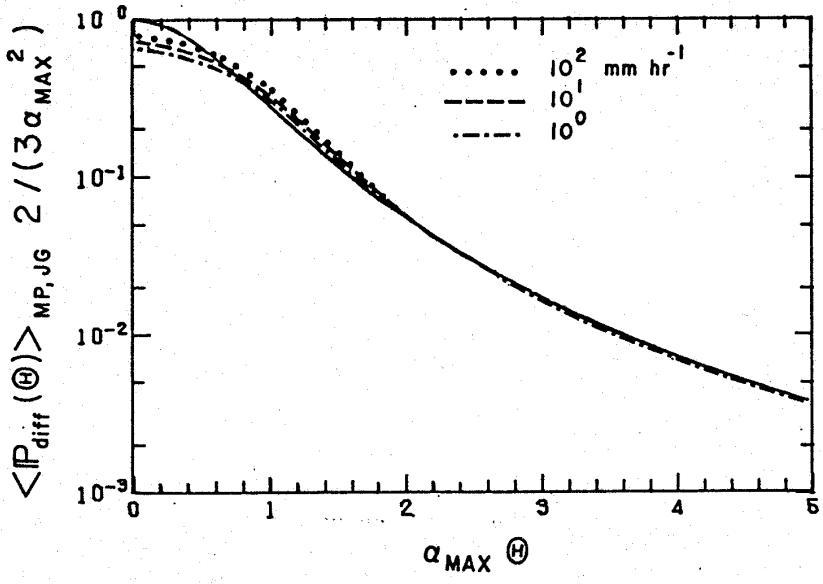

Fig. 2.12 The average diffraction phase function for the Marshall-Palmer (solid) and Joss-Gori (dash and dot) size distributions of spherical water drops. The results for the Joss-Gori distributions are shown at rainfall rates of 1, 10 and 100 mm hr^{-1}. The diffraction phase functions agree at all angles except those near $\Theta = 0$.

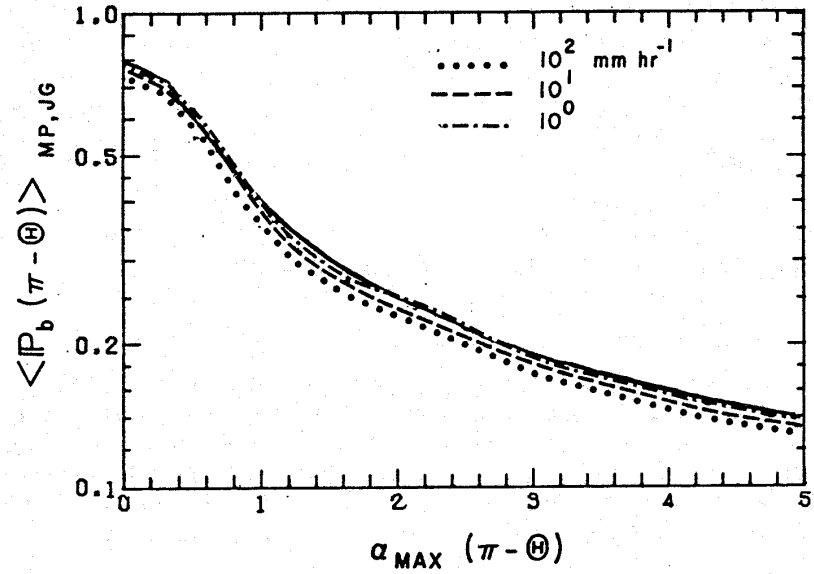

Fig. 2.13 The average backscatter phase function for the Marshall-Palmer (solid) and Joss-Gori (dash and dot) size distributions of spherical water drops. The results for the Joss-Gori distributions are shown at rainfall rates of 1, 10 and 100 mm hr^{-1}. The result for the M-P distribution is shown at R = 10 mm hr^{-1}. These backscatter phase functions include the contributions of the "glory" and geometrical optics, and they differ primarily by a multiplicative constant.

distributions are independently measured. The mean square angle for forward scattering $\langle\theta_f^2\rangle$, on the other hand, is not sensitive to the value of the phase function near $\theta \sim 0$. It can therefore be expected that $\langle\theta_f^2\rangle$ for both the real "instantaneous" drop size distributions and the distribution of Marshall and Palmer will be similar functions of the characteristic drop size D_{max}.

The average backscatter phase function can be found using Eqs. 2.9, such that

$$\langle \mathbf{P}_b(\alpha_{max}[\pi-\theta])\rangle = \mathbf{P}_{geom}(\tilde{m},\pi) + \frac{1}{\beta_r}\int_0^\infty N(D)K_{sca}\frac{\pi D^2}{4}C'(D)\cdot$$

$$\cdot[(1+\kappa)^2 J_o^2(w_b)+(1-\kappa)^2 J_2^2(w_b)]dw_b \qquad (2.19a)$$

where w_b is given by Eq. 2.9b. The backscatter phase function for the M-P drop size distribution is then

$$\langle \mathbf{P}_b(\alpha_{max}[\pi-\theta])\rangle_{MP} = \mathbf{P}_{geom}(\tilde{m},\pi) + \frac{4\langle C'(D)\rangle_{MP}}{\alpha_{max}^3(\pi-\theta)^3}\int_0^\infty \exp\left[\frac{-2w_b}{\alpha_{max}(\pi-\theta)}\right]\cdot w_b^2$$

$$[(1+\kappa)^2 J_o^2(w_b)+(1-\kappa)^2 J_2^2(w_b)]dw_b \qquad (2.19b)$$

where the average value for $C'(D)$ has been removed from the integral using the mean value theorem.[2] The value

---

[2] The factor $\langle C'(D)\rangle_{MP}$ has a slight functional dependence on the generalized angle $\alpha_{max}(\pi-\theta)$. When $C'(D)$ is linearly interpolated from Table 2.1, then the fractional variation of $\langle C'(D)\rangle_{MP}$ over the range $0 < \alpha_{max}(\pi-\theta) \leq 25$ is approximately $\pm 5\%$. If this variation is neglected, then the average backscatter phase function of the M-P size distribution is a universal function of the generalized angle $\alpha_{max}(\pi-\theta)$.

of the scattering phase function for the M-P size distribution in the backscattering direction is

$$\langle P_b(\Theta=\pi)\rangle_{MP} = \langle C'(D)\rangle_{MP} \cdot (1+\kappa)^2 \qquad (2.20)$$

The backscatter phase function for the M-P size distribution with $R = 10$ mm hr^{-1} is shown in Fig. 2.13 as a function of the generalized angle $\alpha_{max}(\pi-\Theta)$. Backscatter phase functions for the J-G size distributions were also calculated for $R = 1$, 10 and 100 mm hr^{-1}, and these results are included in Fig. 2.13 for comparison to the M-P backscatter phase function at $R = 10$ mm hr^{-1}. It can be noted from Fig. 2.13 that the M-P and J-G backscatter phase functions differ primarily by a multiplicative constant. When the backscatter phase functions are normalized to unity at $\Theta = \pi$, then the fractional variation of these phase functions from the M-P result for $R = 10$ mm hr^{-1} is less than $\pm 5\%$. The backscatter phase functions for both the M-P and J-G size distributions at $\Theta = \pi$ are shown as a function of the total optical extinction coefficient in Fig. 2.14.

The multiple scattering theory which is developed in Chapter 3 can be applied to media with phase functions which are described by sums of Gaussian functions. It is therefore useful to approximate the rainfall scattering phase functions by such a sum of Gaussian functions.

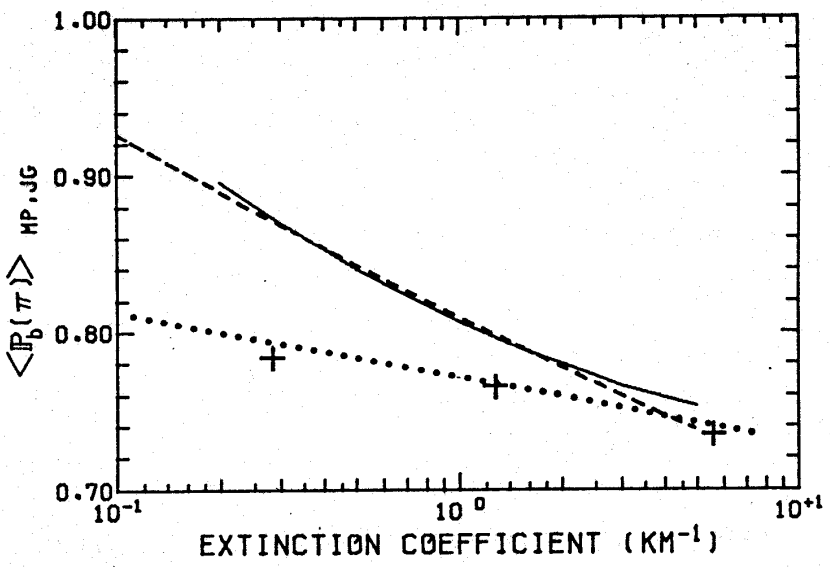

Fig. 2.14 The value of the backscatter phase function for Marshall-Palmer (solid) and Joss-Gori (+) size distributions of spherical water drops as a function of the total optical extinction coefficient. The power law fits of Eq. 2.26 for the backscatter phase functions of the M-P (dash) and JG (dot) size distributions are included.

Quadruple Gaussian approximations were determined for both the forward scattering and backscattering phase functions for Marshall-Palmer rainfall, such that

$$\bar{P}_{geom}(\tilde{m}=1.333,\theta) = 7.9 \exp(-4.1 \text{rad}^{-2}\theta^2) \qquad (2.21a)$$

$$\langle \bar{P}_{diff}(\alpha_{max}\theta)\rangle_{MP} = \frac{3}{2}\alpha_{max}^2\{0.72 \exp(-2.2\,\alpha_{max}^2\theta^2) + 0.273 \exp(-0.38\,\alpha_{max}^2\theta^2) + 0.007 \exp(-0.024\,\alpha_{max}^2\theta^2)\} \qquad (2.21b)$$

$$\langle \bar{P}_b(\alpha_{max}[\pi-\theta])\rangle_{MP} = 0.05 + 0.76\,\beta^{-0.06}\{0.55 \exp(-2.3\,\alpha_{max}^2\theta^2) + 0.30 \exp(-0.20\,\alpha_{max}^2\theta^2) + 0.15 \exp(-0.008\,\alpha_{max}^2\theta^2)\} \qquad (2.22)$$

The Eq. 2.21 and 2.22 approximations for the diffraction and backscatter phase functions are compared to the exact phase functions for the M-P size distribution in Figs. 2.15a and 2.15b, respectively. The geometrical optics portion of the forward scattering phase function is included in Fig. 2.3 for comparison to the exact results of geometrical optics.

The multiple scattering solution of Chapter 3 becomes very time consuming when the forward phase function is described by more than two Gaussian functions. It is therefore useful to apply a single Gaussian approximation to the diffraction phase function. The single Gaussian function which has the same value at $\Theta = 0$ and the same area as the diffraction phase function is

$$\langle P_{diff}(\alpha_{max}\Theta)\rangle_{MP} = \frac{3}{2}\,\alpha_{max}^2\,\exp[-0.75\,\alpha_{max}^2\Theta^2] \qquad (2.23)$$

This single Gaussian approximation is included in Fig. 2.15a for comparison to the triple Gaussian approximation for the diffraction phase function.

The optical extinction coefficient can be obtained from a backscattered lidar signal when the relationship between the volume backscattering cross section and the extinction coefficient is known a priori or is obtained by an independent measurement. Viezee, Uthe and Collis (1969) show that range profiles of the extinction coefficient can be obtained analytically from backscattered lidar signals when the relationship between $P_b(\pi)$ and β is

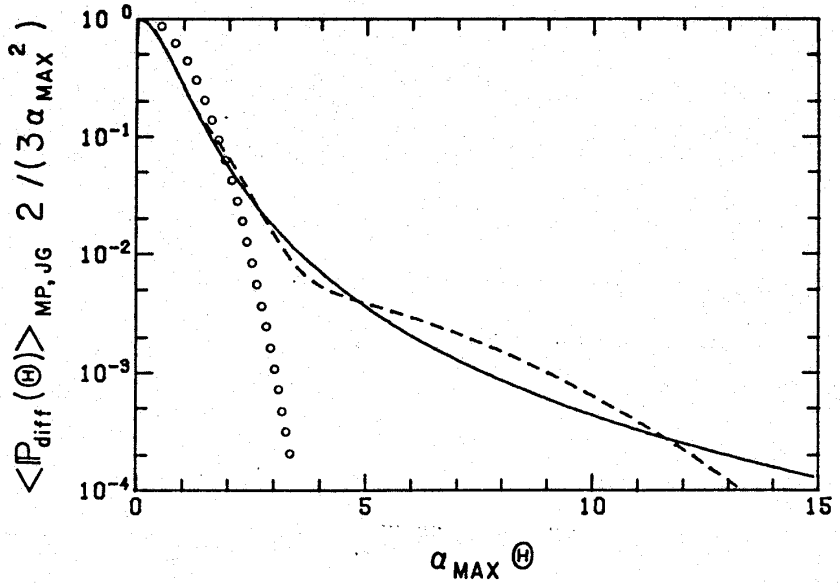

Fig. 2.15a The average diffraction phase function for the Marshall-Palmer size distributions of spherical water drops (solid). The triple Gaussian approximation of Eq. 2.21b is included for comparison (dash). A single Gaussian approximation to the diffraction phase function which has the same area and same value at $\Theta = 0$ is also shown (dots).

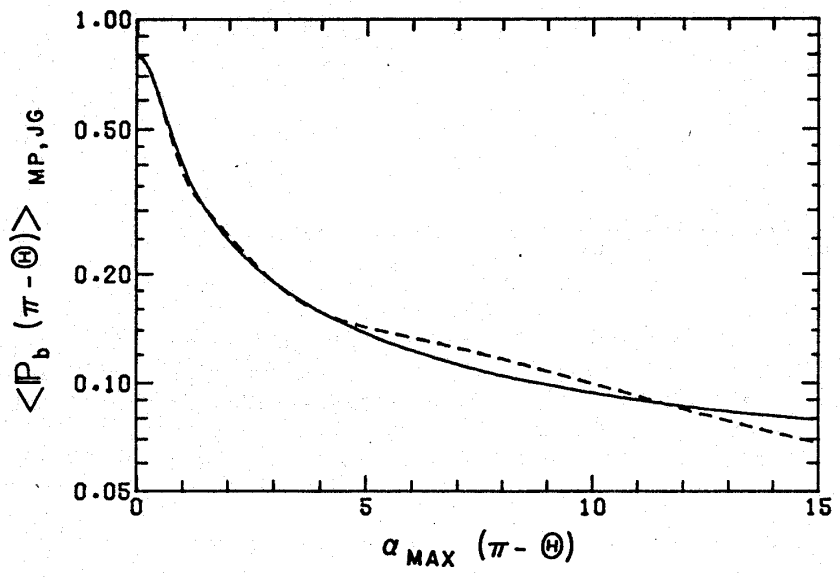

Fig. 2.15b The average backscatter phase function for the Marshall-Palmer size distribution of spherical water drops (solid). The triple Gaussian approximation of Eq. 2.22 is included for comparison (dash). These backscatter phase functions include the contributions of the "glory" and geometrical optics.

of the form

$$P_b(\pi) = k_1 \beta^{k_2} \tag{2.24}$$

where k_1 and k_2 are constants. A relationship between $P_b(\pi)$ and β in the form of Eq. 2.24 was experimentally determined by Curcio and Knestrick (1958). These authors correlated atmospheric transmission and the backscattering of visible light in clear weather, fog, drizzle and rain, with the result

$$P_b(\pi) \propto \beta^{-0.33} \tag{2.25}$$

The backscattering measurements were obtained using a source and receiver with 3 degree beam widths, and these measurements should therefore reflect the geometrical optics phase function in the cases involving drizzle or rain. When the data of Curcio and Knestrick for drizzle and rain [their Fig. 5] is separated from that for clear weather and fog, then it is no longer obvious that Eq. 2.25 should hold. The Curcio and Knestrick data for rain and drizzle is consistent with a constant backscatter phase function due to geometrical optics, however.

A relationship between $P_b(\pi)$ and β in the form of Eq. 2.24 was determined by regression using the calculated values of Fig. 2.14, with the results

$$\langle P_b(\pi) \rangle_{MP} \simeq 0.05 + 0.76\ \beta^{-0.06} \tag{2.26a}$$

$$\langle P_b(\pi) \rangle_{JG} \simeq 0.05 + 0.72\ \beta^{-0.025} \tag{2.26b}$$

where β is given in units of km^{-1}. The Eq. 2.26 approximations

for the backscatter phase function are included in Fig. 2.14 for comparison. This figure shows that the more realistic "instantaneous" drop size distributions of Joss and Gori yield a backscatter phase function value which for all practical purposes is independent of the optical extinction coefficient.

2.5 Summary of the Scattering Properties of Rainfall

This section summarizes the scattering properties for rainfall which is characterized by a Marshall-Palmer (M-P) size distribution of spherical water drops with real refractive index $\tilde{m} = 1.333$. The M-P size distribution is

$$N_{MP}(D) = N_o \exp[-\Lambda D] \tag{2.10}$$

where D is drop diameter, $N_o = 8000\ m^{-3}$ is a constant and

$$\Lambda = \begin{cases} 4.1\ \mathbb{R}^{-0.21} & (2.11) \\ \left(\frac{\pi N_o}{\beta}\right)^{-1/3} & (2.13) \end{cases}$$

$\mathbb{R}$ [mm hr^{-1}] is the rainfall rate and β [km^{-1}] is the optical extinction coefficient. The "instantaneous" drop size distributions of Joss and Gori (1978, cf. Fig. 2.11 and Table 2.2) give phase functions for diffraction and backscattering which are sufficiently similar to those

for the M-P size distributions so that no further reference need be made to J-G phase functions, cf. Figs. 2.12 and 2.13. The scattering phase functions are given in terms of the generalized scattering angle $\alpha_{max}\Theta$, where

$\alpha_{max} = \frac{2\pi}{\lambda}\Lambda^{-1}$ size parameter of the drop size which gives the largest contribution to the optical extinction coefficient

Θ scattering angle

λ wavelength of the scattered light.

The phase function due to geometrical optics is shown in Fig. 2.3. The forward portion of the geometrical optics phase function can be approximated by a single Gaussian function, such that

$$P_{geom}(\tilde{m}=1.333,\Theta) \simeq 7.9 \exp(-4.1 \text{ rad}^{-2}\Theta^2) \qquad (2.21a)$$

The diffraction phase function for the M-P size distribution is shown in Fig. 2.15a together with the triple Gaussian approximation

$$\langle P_{diff}(\alpha_{max}\Theta)\rangle_{MP} \simeq \frac{6\pi^2}{\lambda^2}\Lambda^{-2}\{0.72 \exp(-2.2\,\alpha_{max}^2\Theta^2) + 0.273 \exp(-0.38\,\alpha_{max}^2\Theta^2) + 0.007 \exp(-0.024\,\alpha_{max}^2\Theta^2)\} \qquad (2.21b)$$

The phase functions are characterized by sums of Gaussian functions since these approximations can be used with the

multiple scattering theory of chapter 3 to estimate the N^{th} order scattering contribution to the return signal of a monostatic lidar. This multiple scattering solution is very time consuming when the number of forward Gaussians is large, however, and it is useful to characterize the diffraction phase function by a single Gaussian function, such that

$$\langle P_{diff}(\alpha_{max}\Theta)\rangle_{MP} \simeq \frac{6\pi^2}{\lambda^2}\,\Lambda^{-2}\,\exp(-0.75\,\alpha_{max}^2\Theta^2) \qquad (2.23)$$

The Eq. 2.21b and 2.23 approximations to the diffraction phase function give identical results when the multiple scattering theory of chapter 3 is applied to the operation of the UW lidar in rainfall (cf. footnote 1 of chapter 4).

The backscatter phase function for the M-P size distribution is shown in Fig. 2.15b together with the triple Gaussian approximation

$$\langle P_b(\alpha_{max}[\pi-\Theta]\rangle_{MP} \simeq 0.05 + 0.76\,\beta^{-0.06}\{0.55\,\exp(-2.3\,\alpha_{max}^2\Theta^2) +$$
$$0.30\,\exp(-0.20\,\alpha_{max}^2\Theta^2) + 0.15\,\exp(-0.008\,\alpha_{max}^2\Theta^2) \qquad (2.22)$$

The constant 0.05 is included to account for the contribution of geometrical optics. The value of the backscatter phase function for the M-P distribution in the backscatter direction is

$$\langle P_b(\pi)\rangle_{MP} \simeq \underbrace{0.05}_{\text{geometrical optics}} + \underbrace{0.76\ \beta^{-0.06}}_{\text{"glory"}} \qquad (2.26a)$$

The value of the backscatter phase function for the "instantaneous" drop size distributions of Joss and Gori is more independent of β, such that

$$\langle P_b(\pi)\rangle_{JG} \simeq \underbrace{0.05}_{\text{geometrical optics}} + \underbrace{0.72\ \beta^{-0.025}}_{\text{"glory"}} \qquad (2.26b)$$

The application of these scattering phase functions for the estimation of the effects of multiple scattering on lidar signals which are obtained from rainfall is discussed in section 4.3.

Chapter 3

SOLUTION FOR MULTIPLE SCATTERING

This chapter presents a general solution for the N^{th} order scattering contribution to the return signal of a monostatic lidar. This solution considers all combinations of N-1 small angle forward scatterings and one large angle scattering, and it applies to media with phase functions which can be characterized by the sum of Gaussian functions. The general solution accounts for the effects of spatially inhomogeneous media for a non-coaxial lidar system with a Gaussian transmitter beam divergence. This theory is based upon the earlier results of Eloranta (1972) and Weinman (1976), and upon the ray tracing solution of Eloranta (1978).

Solutions to the multiple scattering problem have been generally available for a few special cases. Eloranta (1972) derives an exact solution for the double scattering contribution to a monostatic lidar signal. An algebraic error has been found in Eloranta (1972) for the derivation of a special case.[1] Weinman (1976) presents a Neumann solution for the N^{th} order scattering contribution from

---

[1] In the notation of the Eloranta paper, his Eqs. 5.10 and 5.11 should read

a spatially homogeneous medium which is characterized by a multi-Gaussian phase function. The Neumann solution of Weinman applies for a coaxial monostatic lidar system with zero transmitter beam divergence, and due to an error it is correct only in cases where the receiver field of view is larger than the mean square angle for forward scattering. The Weinman error is examined in section 3.2 (cf. footnote 4).

Several Monte Carlo calculations for the contribution of multiple scattering have also been undertaken. However, these studies serve only to point out the importance of multiple scattering considerations, cf. Plass

$$\frac{1}{2} G_I = \frac{2\pi}{L} \cdot \frac{P_1(0)}{4\pi} \int_0^{\theta_*} \frac{P_1(\pi-\theta_1)}{4\pi} \cdot e^{-\frac{\theta_1^2}{\langle\theta^2\rangle}} \cdot \theta_1 d\theta_1 + \frac{2\pi\rho_r}{L} \cdot \frac{P_1(0)}{4\pi} \int_{\theta_*}^{\infty} \frac{P_1(\pi-\theta_1)}{4\pi} \cdot e^{-\frac{\theta_1^2}{\langle\theta^2\rangle}} \cdot d\theta_1 \tag{5.10}$$

and

$$\frac{1}{2} G_I = \frac{d}{L^2} \frac{\langle P_1(\pi)\rangle_2}{4\pi} \left[1-\exp\left(-\frac{L^2\rho_r^2}{4d^2\langle\theta^2\rangle}\right)\right] + \frac{1}{2}\frac{\rho_r}{L} \frac{\langle P_1(\pi)\rangle_2}{4\pi} \sqrt{\frac{\pi}{\langle\theta^2\rangle}} \left[1-\operatorname{erf}\left(\frac{\rho_r L}{2d\sqrt{\langle\theta^2\rangle}}\right)\right] \tag{5.11}$$

where $d = (L-2x_c)/2$. The effect of this error on solution results is not significant in cases where the receiver field of view is less than the mean square angle for forward scattering. This error is significant when it is applied to problems involving rain, however.

and Kattawar (1971), Kunkel and Weinman (1976).

A ray tracing solution for the N^{th} order scattering contribution from an isotropically backscattering medium has been derived by Eloranta (1978). This ray tracing solution is presented in Appendix A, and the results of this solution for isotropic backscattering are summarized in section 3.1. A revised Neumann solution is derived in section 3.2 following the original procedure of Weinman (1976). This revised Neumann solution is generalized in this section so that it applies to spatially inhomogeneous media for non-coaxial lidar systems with a Gaussian transmitter beam divergence. A summary of the revised Neumann solution is given in section 3.3.

3.1 Ray Tracing Theory for Multiple Scattering

3.1a N^{th} Order Forward Scattering with One Isotropic Backscattering

The ray tracing theory of Eloranta (1978) for the contribution of N^{th} order multiple scattering to the return signal of a coaxial monostatic lidar is examined in this section. This ray tracing theory considers all combinations of N-1 small angle forward scatterings and one isotropic backscattering to characterize the multiple scattering contribution, and it neglects any contribution due to multiple large angle scattering. The solution

utilizes single Gaussian functions to characterize both the transmitter beam width and the forward scattering phase function. These results can be applied to phase functions which are characterized by sums of Gaussian functions using the procedure outlined in section 4.2b. A derivation of the ray tracing solution of Eloranta is presented in Appendix A.

Eloranta (1972) investigated the error which is caused by the neglect of multiple large angle scattering in the case of double scattering. Using the cloud model C-1, Eloranta showed [his chapter 7] that the contribution of multiple large angle scattering to the doubly scattered return signal of a monostatic lidar is less than a few percent and it need not be considered. The small angle scattering theories which are discussed in this paper also neglect the contributions of multiple large angle scattering, and they therefore provide a lower bound estimate for the total multiple scattering contribution. An analysis of the multiple large angle scattering contribution is left for later study.

The forward scattering phase function is characterized by a Gaussian function in scattering angle Θ, such that

$$\frac{P_f(\Theta)}{4\pi} = \frac{a}{\pi\langle\Theta_f^2\rangle} \exp\left[-\frac{\Theta^2}{\langle\Theta_f^2\rangle}\right] \qquad (3.1)$$

where $\langle\theta_f^2\rangle$ is the mean square angle for forward scattering and a is the fraction of the total scattered energy which is defined by the forward phase function. Referring to the geometry of Fig. 3.1, the parameters a and $\langle\theta_f^2\rangle$ of Eq. 3.1 are general functions of the penetration depth x. These parameters are not allowed to vary in a plane normal to the lidar propagation axis, however.[2] The angular distribution of the lidar transmitter beam pattern is also characterized by a Gaussian function similar to Eq. 3.1 where the mean square angle of the angular distribution is $\langle\theta_t^2\rangle$. The backscattering phase function is assumed to be isotropic in angle and the transmitter and receiver are coaxial.

The component of the lidar return signal $P_{n,m}$ due to N^{th} order scattering is determined for n small angle forward scatterings up to a single backscattering event, followed by $m = N-n-1$ small angle forward scatterings

---

[2] The mean square radial departure $\langle r^2\rangle$ from the propagation axis at range R due to multiple forward scattering can be estimated from the result for single small angle forward scattering $\langle r^2\rangle \sim \frac{1}{3}\beta R \cdot R^2 \langle\theta_f^2\rangle$, where βR is the average number of scatterings [Fermi (1950), p 53]. For operation of a typical lidar system in light fog, $\beta = 2$ km^{-1}, $R = 1$ km and $\langle\theta_f^2\rangle \sim 4\times10^{-3}$ rad^2, so that the radial departure from the axis of propagation is $r \sim 0.05$ km $\ll R$.

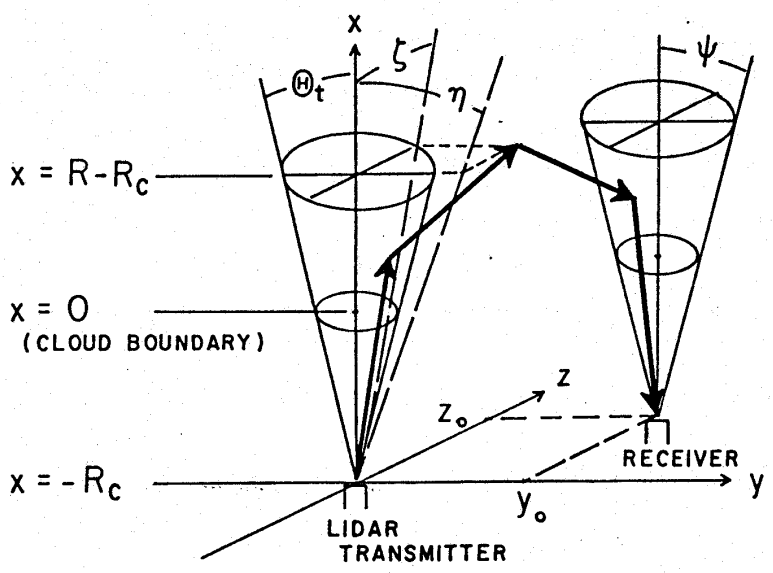

Fig. 3.1 Monostatic lidar geometry convention. The variable R represents the range of the backscattering event location from the lidar along the axis of propagation. The scattering medium boundary is located at range R_c and x is penetration depth into the scattering medium. The lidar receiver is located off axis at the coordinates $x = -R_c$, $y = y_o$ and $z = z_o$.

on the return path to the receiver. The solution to this problem (cf. Appendix A, Eq. A.30) can be written in terms of a dimensionless distance parameter $u = x/(R-R_c)$ such that

$$\frac{P_{n,m}}{P_1} = \tau^{n+m} \int_0^1 du_1 \int_0^{u_1} du_2 \cdots \int_0^{u_{n-1}} du_n \cdot \int_0^1 du_{n+1} \int_{u_{n+1}}^1 du_{n+2} \cdots \int_{u_{n+m-1}}^1 du_{n+m} \cdot$$

$$\prod_{i=1}^{n+m} a(u_i)\rho(u_i)\left\{1-\exp\left[\frac{-\psi^2}{\langle\theta_t^2\rangle+\left(\frac{R-R_c}{R}\right)^2 \sum_{j=1}^{n+m}\langle\theta_f^2\rangle_j u_j^2}\right]\right\} \qquad (3.2)$$

where

$\tau = \int_{R_c}^{R} \beta(R)dR$ one way optical depth between the lidar and the backscattering event location

$a(u)$ range variation of the fraction of total scattered energy which is defined by the forward scattering phase function

$\rho(u) = \beta(u)/\langle\beta\rangle$ spatial structure of the optical extinction coefficient β about the mean value $\langle\beta\rangle = \tau/(R-R_c)$

$R-R_c$ penetration depth, where R_c is the distance between the scattering medium boundary and the lidar

$\langle\theta_t^2\rangle$ mean square angle of the transmitter beam pattern

$\langle\theta_f^2\rangle$ mean square angle for forward scattering.

Eq. 3.2 can be used to estimate the contribution of multiple scattering to the lidar return signal from a spatially inhomogeneous medium of isotropically backscattering particles. The total return signal P_N due to N^{th} order multiple scattering from such a medium can be obtained by summing the various combinations $P_{n,m}$, such that

$$\frac{P_N}{P_1} = \sum_{n=0}^{N-1} \frac{P_{n,m}}{P_1} \qquad (3.3)$$

where $m = N-n-1$. When $\psi^2 \gg \langle\theta_f^2\rangle$ and $\rho(u) = 1$, the integrand of Eq. 3.2 is unity and the multiple integrals

can be readily evaluated. It can then be seen by inspection of Eq. 3.2 in this limit that the components $P_{n,m}$ are related by $P_{n+m,0}$ by

$$P_{n,m} = \frac{(n+m)!}{n!m!} P_{n+m,0} \tag{3.4}$$

Eq. 3.4 has been empirically found to hold for smaller values of the ratio $\psi^2/\langle\theta_f^2\rangle$ as well as for several spatially inhomogeneous distributions of the optical extinction coefficient.[3]

Assuming that Eq. 3.4 holds in general, then the total return signal due to N^{th} order multiple scattering from a spatially inhomogeneous medium of isotropically backscattering particles is

$$\boxed{\frac{P_N}{P_1} = 2^{N-1}\langle a\rangle^{N-1} \frac{\langle P(\pi)\rangle^N}{P(\pi)} A_N \frac{\tau^{N-1}}{(N-1)!}} \tag{3.5}$$

where the non-dimensional coefficient $A_N(\psi^2, \langle\theta_f^2\rangle, \langle\theta_t^2\rangle, \frac{R-R_c}{R})$ is given by

$$A_N = (N-1)! \int_0^1 du_1 \int_0^{u_1} du_2 \cdots \int_0^{u_{N-2}} du_{N-1} \prod_{i=1}^{N-1} \frac{a(u_i)\rho(u_i)}{\langle a\rangle} \cdot$$

$$\cdot \left\{1 - \exp\left[\frac{-\psi^2}{\langle\theta_t^2\rangle + (\frac{R-R_c}{R})^2 \sum_{j=1}^{N-1} \langle\theta_f^2\rangle_j u_j^2}\right]\right\} \tag{3.6}$$

---

[3] Eq. 3.2 was solved numerically to verify Eq. 3.4 to $\pm 0.1\%$ for $\frac{d}{dR}\langle\theta_f^2\rangle = 0$ and $10^{-4} \leq \psi^2/\langle\theta_f^2\rangle \leq 10^{1}$ with $\rho(u) = 1$, $\rho(u) = 2u$ and $\rho(u) = 2 - 2u$.

The average value of the backscatter phase function $\frac{\langle P(\pi)\rangle_N}{P(\pi)}$ is included in Eq. 3.5 to account for the effects of anisotropic backscattering, and it must be estimated independently in this formulation for isotropic backscattering. The backscatter phase function average value is calculated in chapter 4 using the Neumann solution of section 3.2.

The coefficients A_N are shown for a spatially homogeneous medium with zero transmitter beam divergence in Figs. 3.2 and 3.3 as a function of the dimensionless receiver field of view T^2, where

$$T^2 = \frac{\psi^2}{\langle\theta_f^2\rangle} \cdot \left(\frac{R}{R-R_c}\right)^2 \qquad (3.7a)$$

Note that $0 \leq A_N \leq 1$ in the case of a spatially homogeneous medium where $\frac{da}{dR} = \frac{d\rho}{dR} = \frac{d}{dR}\langle\theta_f^2\rangle = 0$. The coefficients A_N are also given in Table 3.1. The effects of spatial inhomogeneity on multiple scattering are discussed in section 4.1c.

Eqs. 3.5 and 3.6 allow an investigation of the effect of finite transmitter beam divergence on the contribution of multiple scattering to the return signal of a monostatic lidar. Eq. 3.6 was solved numerically for several values of the square ratio of transmitter beam divergence to receiver field of view Φ^2, where

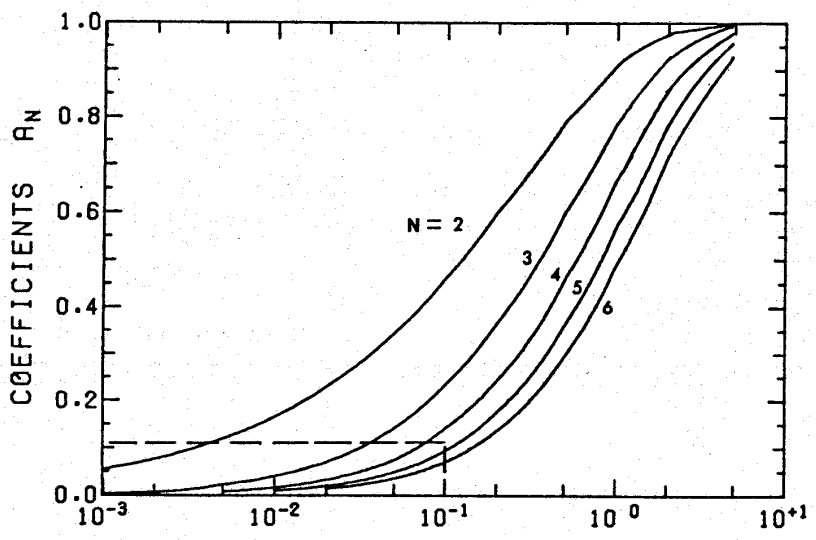

$$T^2 = \frac{\psi^2}{\langle \Theta_f^2 \rangle} \left(\frac{R}{R-R_c} \right)^2$$

Fig. 3.2 Variation of the coefficients A_N as a function of the parameter T^2 for $2 \leq N \leq 6$. These coefficients can be used with Eq. 3.5 to estimate the contribution of multiple scattering to a coaxial monstatic lidar signal from a spatially homogeneous medium of isotropic backscatterers. The area enclosed by the dashed line is shown in an expanded view in Fig. 3.3.

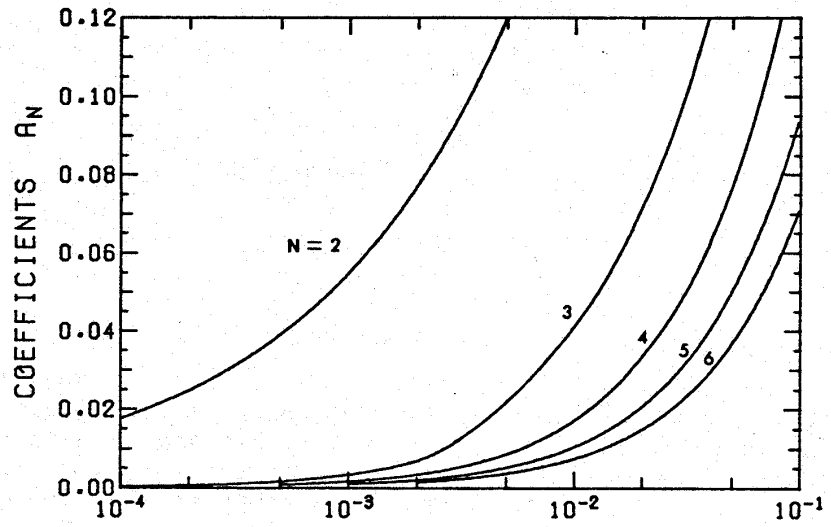

$$T^2 = \frac{\psi^2}{\langle \Theta_f^2 \rangle} \left(\frac{R}{R-R_c} \right)^2$$

Fig. 3.3 An expanded view of the coefficients A_N for small values of the parameter T^2 for $2 \leq N \leq 6$. See caption for Fig. 3.2.

Table 3.1

Values for the Coefficients A_N for $2 \leq N \leq 6$ and $\langle\theta_t^2\rangle = 0$ as a Function of $T^2 = \frac{\psi^2}{\langle\theta_f^2\rangle}\left(\frac{R}{R-R_c}\right)^2$.

T^2	A_2	A_3	A_4	A_5	A_6
1.0-4	1.76-2	3.52-4	1.77-4	1.07-4	7.66-5
2.0-4	2.49-2	7.03-4	3.54-4	2.14-4	1.53-4
5.0-4	3.91-2	1.76-3	8.84-4	5.35-4	3.82-4
1.0-3	5.50-2	3.50-3	1.77-3	1.07-3	7.64-4
2.0-3	7.73-2	6.98-3	3.52-3	2.14-3	1.53-3
5.0-3	1.20-1	2.34-2	8.74-3	5.32-3	3.81-3
1.0-2	1.67-1	4.13-2	1.73-2	1.06-2	7.59-3
2.0-2	2.31-1	7.18-2	3.37-2	2.09-2	1.51-2
5.0-2	3.47-1	1.44-1	7.68-2	5.04-2	3.70-2
1.0-1	4.62-1	2.35-1	1.43-1	9.54-2	7.20-2
2.0-1	5.99-1	3.66-1	2.43-1	1.76-1	1.37-1
5.0-1	7.91-1	6.00-1	4.60-1	3.64-1	2.97-1
1.0	9.11-1	7.87-1	6.68-1	5.69-1	4.90-1
2.0	9.79-1	9.26-1	8.58-1	7.85-1	7.16-1
5.0	9.99-1	9.95-1	9.83-1	9.64-1	9.37-1

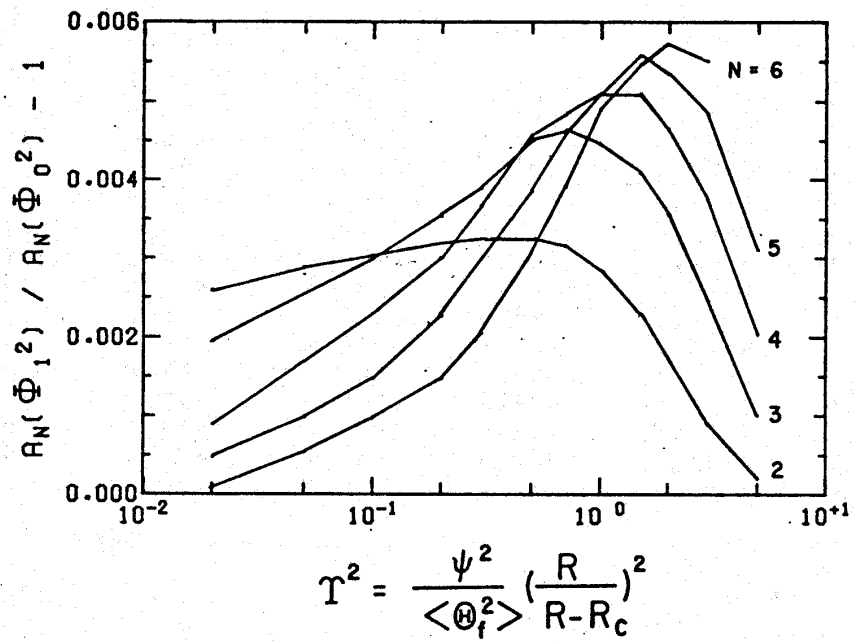

Fig. 3.4 Fractional error in the estimate of the coefficients A_N which is incurred when the effects of finite transmitter beam width are neglected. The fractional difference is shown for $\Phi_1^2 = \langle\theta_t^2\rangle\psi^{-2} = 0.01$ and $\Phi_0^2 = 0$ for the case of a spatially homogeneous scattering medium.

$$\Phi^2 = \frac{\langle \Theta_t^2 \rangle}{\psi^2} \qquad (3.7b)$$

It can be seen by inspection of Eq. 3.6 that the A_N will decrease in value as the magnitude of Φ^2 is increased. Typical monostatic lidar systems operate with half angle transmitter beam divergences $\langle \Theta_t^2 \rangle^{1/2} \sim 0.5$ mrad and receiver fields of view $\psi \sim 5$ mrad such that $\Phi^2 \sim 0.01$. The fractional difference $A_N(\Phi_1^2)/A_N(\Phi_0^2) - 1$ in the magnitude of A_N for $\Phi_0^2 = 0$ and $\Phi_1^2 = 0.01$ is shown in Fig. 3.4 as a function of the dimensionless receiver field of view T^2 for a spatially homogeneous medium and $2 \leq N \leq 6$. Fig. 3.4 indicates that an overestimate of less than 1% in the magnitude of the multiple scattering contribution would occur if the effects of finite transmitter beam width are neglected for a lidar with $\Phi^2 = 0.01$. As shown in Fig. 3.4, this fractional error increases with scattering order N at values of the dimensionless receiver field of view $T^2 > 1$. As indicated in Fig. 3.2, however, the multiple scattering coefficients A_N decrease with increasing N , and the total error which is incurred by the neglect of transmitter beam divergence can be explained by the results for the first few orders of scattering. Similar results were obtained for the spatially inhomogeneous scattering distributions $\rho(u) = 2u$ and $\rho(u) = 2 - 2u$. A neglect of

the transmitter beam divergence is therefore justified for lidar systems with $\Phi^2 \lesssim 0.01$, at least in cases for relatively isotropic backscatter phase functions.

Eq. 3.6 can be solved analytically for $N = 2$ with $\langle\theta_t^2\rangle = 0$ in the case of a spatially homogeneous scattering medium, such that

$$A_2 = 1 - \exp(-T^2) + \sqrt{\pi}\, T\, \mathrm{erfc}(T) \qquad (3.8)$$

where $\mathrm{erfc}(T) = \frac{2}{\sqrt{\pi}} \int_T^\infty \exp(-t^2)dt$ is the error function and T^2 is given by Eq. 3.7a. Eq. 3.8 is identical to the exact result of Eloranta (1972) for the contribution of double scattering to the return signal of a monostatic lidar with zero transmitter beam divergence in the case of a spatially homogeneous isotropic backscattering medium.

3.1b Second Order Scattering with One Anisotropic Backscattering

A ray tracing solution for the contribution of second order scattering with anisotropic backscattering is also presented by Eloranta (1978). The forward scattering phase function is given by Eq. 3.1, and the backscattering phase function is similarly characterized by a Gaussian function in scattering angle θ , such that

$$\frac{\mathbf{P}_b(\theta)}{4\pi} = \frac{\mathbf{P}(\pi)}{4\pi} \exp\left[-\frac{(\pi-\theta)^2}{\langle\theta_b^2\rangle}\right] \qquad (3.9)$$

where $\langle\theta_b^2\rangle$ is the mean square angle for backscattering at the penetration depth $R-R_c$. This double scattering result is obtained for a transmitter beam pattern which is characterized by a Dirac delta function in angle [$\lim \langle\theta_t^2\rangle \to 0$] .

The ratio of second order scattering to single scattering with anisotropic backscattering is

$$\frac{P_2}{P_1} = \tau \int_0^1 du\ 2a(u)\rho(u)\ \frac{1 - \exp\left\{-\dfrac{1+Q\left(1-\frac{R-R_c}{R}u\right)^2}{u^2}\dfrac{\psi^2}{\langle\theta_f^2\rangle}\right\}}{1+Q\left(1-\frac{R-R_c}{R}u\right)^2} \qquad (3.10)$$

where $Q = \langle\theta_f^2\rangle/\langle\theta_b^2\rangle$. Eq. 3.10 reduces to the exact result of Eq. 3.8 in the case of a spatially homogeneous medium with isotropic backscattering [$\lim \langle\theta_b^2\rangle \to \infty$] . With an additional limit of large receiver field of view, Eq. 3.10 is readily integrated such that

$$\lim_{\psi\to\infty} \frac{P_2}{P_1} = 2\langle a\rangle\tau\ \frac{R}{R-R_c}\ \frac{1}{\sqrt{Q}}\left\{\tan^{-1} Q - \tan^{-1}\left(\frac{R_c}{R}\sqrt{Q}\right)\right\} \qquad (3.11)$$

A comparison of Eqs. 3.5 and 3.11 provides an estimate of the effect of anisotropic backscattering on the coefficient A_2 in the limit of large receiver field of view. An inspection of these equations indicates that the value of A_2 is <u>decreased</u> when a Gaussian backscattering phase

function of the form of Eq. 3.9 is introduced.

3.2 Neumann Solution for the Contribution of Multiple Small Angle Scattering

Weinman (1976) outlines a Neumann solution for the contribution of N^{th} order multiple scattering to the return signal of a coaxial monostatic lidar with zero transmitter beam divergence. This Neumann solution considers all combinations of $N-1$ small angle forward scatterings and one large angle scattering, and it neglects any contribution due to multiple large angle scattering. The forward and backward scattering phase functions are characterized by sums of Gaussian functions in scattering angles θ and $\pi-\theta$, respectively, and these phase functions are assumed to be independent of the penetration depth $x = R-R_c$. Weinman chose to average the transverse displacements of the multiply scattered radiances rather than evaluate them explicitly at each scattering event location. In addition, this average was performed incorrectly so that the solution is correct when the lidar receiver field of view is greater than the mean square angle for forward scattering.[4] A revised Neumann solution

---

[4]Referring to Weinman (1976), the average squared displacement [his Eq. 10] is summed over all deflections due to scattering events at fixed penetration depths. This sum is then incorrectly interpreted

is presented in this section.

The original derivation of Weinman is further generalized to include scattering by a spatially inhomogeneous medium, a Gaussian function transmitter beam pattern and a non-coaxial lidar system geometry. The noncoaxial lidar geometry is defined with transmitter and receiver axes aligned in parallel with an axial separation distance L.

Referring to the lidar geometry of Fig. 3.1, the radiance I must satisfy the following time dependent three dimensional radiative transfer equation:

$$\frac{1}{c}\frac{\partial I}{\partial t} + \cos\theta\,\frac{\partial I}{\partial x} + \sin\theta\cos\phi\,\frac{\partial I}{\partial y} + \sin\theta\sin\phi\,\frac{\partial I}{\partial z} + \beta I = \tilde{\omega}\beta\int_0^{2\pi} d\phi' \int_0^{\pi} \sin\theta' d\theta' I(x,y,z,\theta',\phi',t)\,\frac{P(\theta',\phi';\theta,\phi)}{4\pi} \qquad (3.12)$$

where

c speed of light

t time

$x = R - R_c$ penetration depth and coordinate axis along the direction of propagation

y,z coordinate axes perpendicular to the propagation axis

---

as an integration over penetration depth [his Eq. 12]. The correct average squared displacement for scattering events at fixed penetration depths is $\langle y^2\rangle + \langle z^2\rangle = (R-R_c)^2\,\Theta^2$ where Θ is the scattering angle [cf. his Eq. 13]. A factor of 3 was introduced at this point and subsequently carried through to the final solution [his Eqs. 25].

$\beta(x)$ extinction coefficient

$\tilde{\omega}$ albedo for single scattering

θ propagation angle with respect to the x axis

ϕ propagation azimuth angle

$P(\theta',\phi';\theta,\phi)$ scattering phase function which describes scattering from angles (θ',ϕ') to (θ,ϕ) .

The radiance $I(x,y,z,\theta,\phi,t)$ originates as a narrow pulse in time and as a narrowly collimated beam at $x = -R_c$ with a Gaussian transmitter beam divergence.

Detours from the propagation axis caused by small angle scattering give rise to a temporal spreading of the return lidar signal. An estimate of this time delay can be obtained using the result cited by Fermi (1950) [cf. footnote #1] for the average radial displacement caused by single small angle forward scattering of a collimated beam. The average distance ℓ traversed by the singly scattered radiance to the location of the backscattering event at penetration depth x is approximately

$$\ell \sim [x^2+\langle \Delta r^2 \rangle]^{\frac{1}{2}} \sim x + \frac{1}{2}\,\frac{\langle \Delta r^2 \rangle}{x} \qquad (3.13a)$$

The additional round trip time delay can then be estimated from Eq. 3.13a such that

$$\delta t \sim \frac{2(\ell - x)}{c} \sim \frac{1}{3}\,\frac{\beta x^2 \langle \theta_f^2 \rangle}{c} \qquad (3.13b)$$

It follows that $\delta t \sim 10^{-8}$ s for $\beta = 2$ km^{-1}, $x = 1$ km

and $\langle\theta_f^2\rangle^{-1} = 250\ \text{rad}^{-2}$, where $\langle\theta_f^2\rangle$ is the scattering angle variance for a narrow diffraction peak characteristic of the small droplets in light fog. Such delays are small in comparison to the typical transit times of lidar signals. It is therefore convenient to separate the temporal and spatial dependence of the scattered radiance I, such that

$$I(x,y,z,\theta,\phi,t) = \tilde{I}(x,y,z,\theta,\phi) \cdot \delta(x-ct) \qquad (3.14)$$

where $\tilde{I}$ accounts only for the spatial dependence of the scattered radiance and $\delta(x-ct)$ is the Dirac delta function. The Eq. 3.14 approximation implies that the forward scattered radiance is located at penetration depth $x = ct$ after a time delay t, and the temporal spreading which arises from small angle forward scattering is neglected.

Radiances which are scattered through large angles other than those near $\theta \sim \pi$ are assumed to be incapable of contributing to the lidar return signal. The scattered radiance is therefore separated into parts which represent energy scattered through small angles $\hat{I}$ and through large angles $\bar{I}$, such that

$$\tilde{I}(x,y,z,\theta,\phi) = \hat{I}(x,y,z,\theta,\phi) + \bar{I}(x,y,z,\theta,\phi) \qquad (3.15a)$$

The forward scattering phase function is also separated

into small angle $\hat{\mathbf{P}}$ and large angle $\bar{\mathbf{P}}$ components, such that

$$\tilde{\mathbf{P}}(\theta',\phi';\theta,\phi) = \hat{\mathbf{P}}(\theta',\phi';\theta,\phi) + \bar{\mathbf{P}}(\theta',\phi';\theta,\phi) \qquad (3.15b)$$

The following derivation is confined to the solution for those radiances which are scattered in the forward direction through small angles, with the exception of one large angle scattering event which directs the scattered radiance back towards the receiver.

The part of Eq. 3.12 which governs small angle scattering is

$$\frac{\partial \hat{I}}{\partial x} + \eta\frac{\partial \hat{I}}{\partial y} + \zeta\frac{\partial \hat{I}}{\partial z} + \beta\hat{I} =$$

$$\tilde{\omega}\beta \int_{-\infty}^{\infty}\int_{-\infty}^{\infty} \hat{I}(x,y,z,\eta',\zeta') \frac{\hat{\mathbf{P}}(\eta',\zeta';\eta,\zeta)}{4\pi} d\eta' d\zeta' \qquad (3.17)$$

where

$\cos\theta \simeq 1$

$\sin\theta \simeq \theta$

$\eta = \theta\cos\phi$

$\zeta = \theta\sin\phi$

$\Theta^2 = (\eta'-\eta)^2 + (\zeta'-\zeta)^2$ is the scattering angle

$\tilde{\omega}\dfrac{\hat{\mathbf{P}}(\Theta)}{4\pi} = \sum_{i=1}^{I} \dfrac{a_i\gamma_{f,i}}{\pi} \exp[-\gamma_{f,i}\Theta^2]$ is a multi-Gaussian approximation to the forward scattering phase function.

The albedo for single scattering $\tilde{\omega}$ is included in the factors a_i in the subsequent derivation to reduce the number of symbols.

Following the original development of Weinman (1976), a Neumann solution is now developed for the contribution of N^{th} order multiple small angle forward scattering to the return signal of a monostatic lidar. This solution includes all combinations of n forward scatterings and one backscattering, followed by $m = N-n-1$ forward scatterings on the return path to the receiver. A general solution is found for which the extinction coefficient and the scattering phase functions are allowed to vary with penetration depth x, but are not allowed to vary along the y or z axes. The assumption of a plane parallel scattering medium is not restrictive since lidar beam divergences and forward phase function widths are small, and the transverse displacements due to multiple scattering are small in comparison to the penetration depth [cf. footnote #1].

The Neumann solution to Eq. 3.17 for the radiance which is scattered in the forward direction is

$$\hat{I} = \sum_{n=0}^{\infty} \hat{I}_n \tag{3.18}$$

where

$$\frac{\partial \hat{I}_n}{\partial x} + \eta\frac{\partial \hat{I}_n}{\partial y} + \zeta\frac{\partial \hat{I}_n}{\partial z} + \beta\hat{I}_n =$$

$$(1-\delta_{n,0})\beta \sum_{i=1}^{I} \frac{a_i\gamma_{f,i}}{\pi} \int_{-\infty}^{\infty}\int_{-\infty}^{\infty} \exp\{-\gamma_{f,i}[(\eta'-\eta)^2+(\zeta'-\zeta)^2]\}\hat{I}_{n-1}(\eta',\zeta')d\eta'd\zeta' \tag{3.19}$$

The subscript n denotes the number of small angle forward scatterings and the Kronecker delta is defined by

$$\delta_{n,m} = \begin{cases} 1 & n=m \\ 0 & n\neq m \end{cases} \tag{3.20}$$

Eq. 3.19 can be solved analytically by taking a two dimensional Fourier transform of $\hat{I}_n$ defined by

$$\hat{i}_n(x,p,q,\eta,\zeta) = \frac{1}{2\pi}\int_{-\infty}^{\infty}\int_{-\infty}^{\infty} \hat{I}_n(x,y,z,\eta,\zeta)\exp[\hat{j}(py+qz)]dydz \tag{3.21}$$

where $\hat{j}^2 = -1$. Eq. 3.19 is then transformed to

$$\frac{\partial \hat{i}_n(x_{n+1})}{\partial x_{n+1}} + \hat{i}_n(x_{n+1})[\beta(x_{n+1})-\hat{j}(\eta p+\zeta q)] =$$

$$(1-\delta_{n,0})\beta(x_{n+1}) \sum_{i=1}^{I} \frac{a_i\gamma_{f,i}}{\pi} \int_{-\infty}^{\infty}\int_{-\infty}^{\infty} \exp\{-\gamma_{f,i}[(\eta'-\eta)^2+(\zeta'-\zeta)^2]\}\cdot$$

$$\hat{i}_{n-1}(x_n,\eta',\zeta')d\eta'd\zeta' \tag{3.22}$$

where x_n and x_{n+1} represent the locations of the n^{th} and $n+1^{rst}$ scattering events. The boundary condition

which applies at the cloud base must account for the effects of the transmitter beam divergence, and it is given by

$$\hat{i}_0(x_1=0,p,q,\eta,\zeta) = \frac{\gamma_t}{2\pi^2} \exp[-\gamma_t(\eta^2+\zeta^2)+\hat{j}(\eta p+\zeta q)R_c] \qquad (3.23)$$

It follows from Eqs. 3.22 and 3.23 with $n = 0$ that

$$\hat{i}_0(x_1,p,q,\eta,\zeta) = \hat{i}_0(0,p,q,\eta,\zeta)\cdot\exp\{-\int_0^{x_1} [\beta-\hat{j}(\eta p+\zeta q)]dx\} \qquad (3.24a)$$

and for $n > 0$ that

$$\hat{i}_n(x_{n+1},p,q,\eta,\zeta) = \int_0^{x_{n+1}} \hat{J}_{n-1}(x_n,p,q,\eta,\zeta)\cdot\exp\{-\int_{x_n}^{x_{n+1}} [\beta-\hat{j}(\eta p+\zeta q)]dx\}dx_n \qquad (3.24b)$$

where

$$\hat{J}_{n-1}(x_n,p,q,\eta,\zeta) = \beta(x_n) \sum_{i=1}^{I} \frac{a_i\gamma_{f,i}}{\pi} \cdot$$

$$\cdot \int_{-\infty}^{\infty}\int_{-\infty}^{\infty} \hat{i}_{n-1}(x_n,p,q,\eta',\zeta')\cdot\exp\{-\gamma_{f,i}[(\eta'-\eta)^2+(\zeta'-\zeta)^2]\}d\eta'd\zeta' \qquad (3.24c)$$

The multiply scattered radiance penetrates the medium to a depth $R-R_c$ where it is backscattered. The backscatter phase function is represented by the multi-Gaussian function

$$\frac{\hat{\mathbf{P}}(\pi-\Theta)}{4\pi} = \sum_{s=1}^{S} \frac{\mathbf{P}_s(\pi)}{4\pi} \exp\{-\gamma_{b,s}[(\eta'+\eta)^2+(\zeta'+\zeta)^2]\} \qquad (3.25a)$$

where (η',ζ') is the direction of the forward directed radiance and (η,ζ) is the direction after the single large angle scattering, such that

$$(\pi-\theta)^2 = (\eta'+\eta)^2 + (\zeta'+\zeta)^2 \tag{3.25b}$$

The radiance which is subsequently propagated back to the lidar receiver through m small angle forward scatterings is then subject to the boundary condition

$$\hat{\hat{i}}_{n,0}(R-R_c,p,q,\eta,\zeta) = \beta(R-R_c) \sum_{s=1}^{S} \frac{P_s(\pi)}{4\pi} \cdot$$

$$\cdot \int_{-\infty}^{\infty} \int_{-\infty}^{\infty} \hat{i}_n(R-R_c,p,q,\eta',\zeta') \cdot \exp\{-\gamma_{b,s}[(\eta'+\eta)^2+(\zeta'+\zeta)^2]\} d\eta' d\zeta' \tag{3.26}$$

Eq. 3.26 can be interpreted as the source of the backward propagating radiance.

The backscattered radiance must satisfy an equation similar in form to Eq. 3.22. The Neumann solution for this backward directed radiance after n scatterings in the forward direction and <u>no</u> scatterings in the backward direction is

$$\hat{\hat{i}}_{n,0}(x_{n+1},p,q,\eta,\zeta) = \hat{\hat{i}}_{n,0}(R-R_c,p,q,\eta,\zeta) \cdot \exp\{-\int_{X_{n+1}}^{R-R_c} [\beta-\hat{j}(\eta p+\zeta q)]dx\} \tag{3.27}$$

where $\hat{\hat{i}}_{n,0}(x_{n+1},p,q,\eta,\zeta)$ is defined by Eq. 3.26. It follows that the transformed radiance which exits the

cloud boundary after an additional m forward scatterings in the backward direction is

$$\hat{\hat{i}}_{n,m}(x_{n+m+1}=0,p,q,\eta,\zeta) = \int_0^{R-R_c} \hat{\hat{J}}_{n,m-1}(x_{n+m},p,q,\eta,\zeta)\cdot \cdot\exp\{-\int_0^{x_{n+m}} [\beta-\hat{j}(\eta p+\zeta q)]dx\}dx_{n+m} \tag{3.28a}$$

where

$$\hat{\hat{J}}_{n,m-1}(x_{n+m},p,q,\eta,\zeta) = \beta(x_{n+m}) \sum_{i=1}^{I} \frac{a_i \gamma_{f,i}}{\pi}$$

$$\int_{-\infty}^{\infty}\int_{-\infty}^{\infty} \hat{\hat{i}}_{n,m-1}(x_{n+m},p,q,\eta',\zeta')\cdot\exp\{-\gamma_{f,i}[(\eta'-\eta)^2+(\zeta'-\zeta)^2]\}d\eta'd\zeta' \tag{3.28b}$$

The radiance which is collected by the lidar receiver is

$$P_N = \sum_{n=0}^{N-1}\sum_{m=0}^{N-1} P_{n,m}\delta_{n,N-m-1} \tag{3.29}$$

where

$$P_{n,m} = \int_{-\psi}^{\psi}\int_{-\psi}^{\psi}\int_{-\infty}^{\infty}\int_{-\infty}^{\infty} \hat{\hat{I}}_{n,m}(x=0,y,z,\eta,\zeta)\cdot\tilde{R}(x=0,y,z,\eta,\zeta)dydzd\eta d\zeta \tag{3.30}$$

and where $\tilde{R}(x=0,y,z,\eta,\zeta)$ is the receiver response function. Locating the receiver off-axis at $x = -R_c$, $y = y_o$ and $z = z_o$, then the receiver response function at the

cloud boundary is given by

$$\tilde{R}(x=0,y,z,\eta,\zeta) = \begin{cases} \frac{1}{\pi\psi^2} \cdot \delta[R_c\eta-(y-y_o)]\,\delta[R_c\zeta-(z-z_o)]; & \eta^2+\zeta^2 \le \psi^2 \\ 0 & ; \ \eta^2+\zeta^2 > \psi^2 \end{cases} \tag{3.31}$$

Using Eq. 2.1.8 of Titschmarsh (1948), Eqs. 3.30 and 3.31 can be solved directly in terms of their Fourier transformed functions, such that

$$P_{n,m} = \int_{-\psi}^{\psi}\int_{-\psi}^{\psi}\int_{-\infty}^{\infty}\int_{-\infty}^{\infty} \hat{\hat{i}}_{n,m}(x=0,p,q,\eta,\zeta)\cdot\tilde{r}(x=0,p,q,\eta,\zeta)\,dp\,dq\,d\eta\,d\zeta \tag{3.32}$$

where the receiver response function transform is

$$\tilde{r}(x=0,p,q,\eta,\zeta) = \begin{cases} \frac{1}{2\pi^2\psi^2} \exp\{+\hat{j}R_c[p(\eta+\frac{y_o}{R_c})+q(\zeta+\frac{z_o}{R_c})]\}; & \eta^2+\zeta^2 \le \psi^2 \\ 0 & ; \ \eta^2+\zeta^2 > \psi^2 \end{cases} \tag{3.33}$$

A derivation of the general solution to Eqs. 3.32 and 3.33 is presented in Appendix B. The solution for $P_{n,m}$ is given by Eq. B.13 for a non-coaxial lidar when the lateral separation between the transmitter and receiver optical axes is

$$L = (y_o^2 + z_o^2)^{1/2} \tag{3.34}$$

After some tedious algebraic manipulation, the following simplified Neumann solution can be derived from Eq. B.13:

$$\frac{P_{n,m}}{P_1} = \tau^{n+m} \int_0^1 du_1 \int_0^{u_1} du_2 \cdots \int_0^{u_{n-1}} du_n \cdot \int_0^1 du_{n+1} \int_{u_{n+1}}^1 du_{n+2} \cdots \int_{u_{n+m-1}}^1 du_{n+m} \cdot \mathcal{L}_{n+m+1} \quad (3.35)$$

where

$$\mathcal{L}_n = \frac{\prod_{i=1}^{N} a(u_i)\rho(u_i)}{C_N + \langle\theta_t^2\rangle D_N} \int_0^{\psi} \theta d\theta \exp\left\{\frac{-D_N}{C_N + \langle\theta_t^2\rangle D_N} \left[\theta^2 + \frac{L^2 E_N}{D_N R^2}\right]\right\} \cdot$$

$$\cdot I_o\left\{\frac{2L\theta}{C_N + \langle\theta_t^2\rangle D_N} \left[\frac{D_N}{E_N} \left(C_N + \langle\theta_t^2\rangle D_N\right) - \langle\theta_b^2\rangle\right]^{1/2}\right\} \quad (3.36)$$

$$C_N(u_1,\ldots,u_{N-1}) = \left(\frac{R-R_c}{R}\right)\left[\sum_{i=1}^{N-1} \langle\theta_f^2\rangle u_i u_i^2 + \sum_{j=1}^{N-2} \sum_{k=j+1}^{N-1} \frac{\langle\theta_f^2\rangle u_j \langle\theta_f^2\rangle u_k}{\langle\theta_b^2\rangle} (u_j - u_k)^2\right] \quad (3.37a)$$

$$D_N(u_1,\ldots,u_{N-1}) = 1 + \sum_{i=1}^{N-1} \frac{\langle\theta_f^2\rangle u_i}{\langle\theta_b^2\rangle} \left(1 - \frac{R-R_c}{R} u_i\right)^2 \quad (3.37b)$$

$$E_N(u_1,\ldots,u_{N-1}) = 1 + \frac{\langle\theta_t^2\rangle + \sum_{i=1}^{N-1} \langle\theta_f^2\rangle u_i}{\langle\theta_b^2\rangle} \quad (3.37c)$$

and where

$R-R_c$ penetration depth to the location of the backscattering event, where R and R_c are the ranges from the lidar to the backscattering event location and the scattering medium boundary, respectively

u dimensionless penetration depth, $u = x/(R-R_c)$ where $0 \leq x \leq (R-R_c)$

$a(u)$ spatial structure of the fraction of the total scattered energy which is defined by the forward scattering phase function

τ optical penetration depth, $\tau = \int_0^{R-R_c} \beta(u)du$ where β is the optical extinction coefficient

$\rho(u)$ spatial structure of the optical extinction coefficient about its mean value, $\rho(u) = \beta(u) \cdot (R-R_c)/\tau$

ψ receiver half width field of view

L lateral separation between the lidar transmitter and receiver optical axes

$\langle \theta_b^2 \rangle$ mean square angle for backscattering by the atmosphere at range R

$\langle \theta_f^2 \rangle_u$ mean square angle for forward scattering by the atmosphere at the dimensionless penetration depth u

$\langle \theta_t^2 \rangle$ mean square angle of the transmitter beam pattern

$I_o(\ )$ modified Bessel function (cf. Abramowitz and Stegun (1965), Eq. 9.6.16).

When the lidar system is coaxial such that $L = 0$, then Eq. 3.36 reduces to the relatively simple result

$$\mathcal{L}_N = \frac{\prod_{i=1}^{N-1} a(u_i)\rho(u_i)}{D_N} \{1-\exp[\frac{-D_N\psi^2}{C_N+\langle\theta_t^2\rangle D_N}]\} \qquad (3.38)$$

Note that the integrands $\mathcal{L}_N$ of Eqs. 3.36 and 3.38 are <u>independent</u> of the ordering of the scattering events.

The single scatter signal contribution for a non-coaxial lidar is

$$P_1(R) = \frac{2\beta(R)\frac{P(\pi)}{4\pi}}{\pi\psi^2\langle\theta_t^2\rangle R^2}\exp[-2\int_0^R \beta(R')dR']\cdot\int_0^{\psi}\theta d\theta\ \exp[-\frac{\theta^2}{\langle\theta_t^2\rangle} - \frac{L^2}{R^2}\frac{1}{\langle\theta_t^2\rangle+\langle\theta_b^2\rangle}]\cdot I_o[2\frac{L}{R}\frac{\theta}{\langle\theta_t^2\rangle}] \qquad (3.39a)$$

When the lidar transmitter and receiver optical axes are coaxial, then $L = 0$ and Eq. 3.39a reduces to

$$P_1(R) = \frac{\beta(R)\frac{P(\pi)}{4\pi}}{\pi\psi^2 R^2}\exp[-2\int_0^R \beta(R')dR']\cdot\{1-\exp[-\frac{\psi^2}{\langle\theta_t^2\rangle}]\} \qquad (3.39b)$$

The Neumann solution [Eqs. 3.35-3.39] is identical to the ray tracing theory of section 3.1 for the return signal of a coaxial monostatic lidar, particularly to Eq. 3.2 for isotropic backscattering and to Eq. 3.10 for double scattering with no transmitter beam divergence. This Neumann solution is given in a form for scattering phase functions which are characterized by single Gaussian functions. The solution can be generalized to multi-Gaussian phase functions by incorporating the appropriate combinations of $a(u_i)$, $\langle\theta_f^2\rangle_{u_i}$ and $\langle\theta_b^2\rangle$ into the formulae for $\mathcal{Q}_n$.

The general solution for multiple scattering can be significantly simplified when the components $P_{n,m}$ are related to $P_{n+m,0}$ by Eq. 3.4. A test of Eq. 3.4 was

performed for a coaxial lidar with $3 \leq N \leq 6$ in cases of spatially inhomogeneous media, anisotropic backscattering and finite transmitter beam widths.[5] Eq. 3.4 was found to hold in each of these test cases, which indicates that it may be applicable in general. When $L > 0$, then the integrand $\mathcal{A}_N$ of Eq. 3.36 is no longer symmetrical in u_i and Eq. 3.4 will not hold except at large ranges where $R \gg L$. A general proof of Eq. 3.4 for $N \geq 3$ and $L = 0$ is not available at this time. Assuming that Eq. 3.4 is valid in general, however, then the total return signal of a coaxial monostatic lidar due to N^{th} order multiple scattering is

$$\frac{P_N}{P_1} = 2^{N-1} \tau^{N-1} \int_0^1 du_1 \int_0^{u_1} du_2 \ldots \int_0^{u_{N-2}} du_{N-1} \cdot \mathcal{A}_N \qquad (3.40)$$

where $\mathcal{A}_N$ is given by either Eq. 3.36 for $L > 0$ or Eq. 3.38 for $L = 0$.

3.3 Summary of the Theory for Multiple Scattering

This section summarizes the results of sections 3.1 and 3.2 for the contribution of multiple scattering to

---

[5] Eq. 3.34 was solved numerically to verify Eq. 3.4 to $\pm$ 0.1% for $\rho(u) = 1$, $\rho(u) = 2u$ and $\rho(u) = 2 - 2u$, as well as for $Q = 10^{-1}, 10^{0}, 10^{+1}$ and $\langle\Theta_t^2\rangle/\psi^2 = 10^{-1}, 5\times10^{-1}$.

the return signal of a coaxial monostatic lidar. The complete solution for a non-coaxial lidar system is given by Eqs. 3.35-3.37. Using Eq. 3.4 to relate the total return signal P_N to the individual components $P_{n,m}$ where $m = N=n-1$, then the N^{th} order scattering contribution to the return signal of a coaxial monostatic lidar can be calculated from the simple expression

$$\boxed{\frac{P_N}{P_1} = 2^{N-1} \cdot \langle a \rangle^{N-1} \frac{\langle P(\pi) \rangle_N}{P(\pi)} A_N \cdot \frac{\tau^{N-1}}{(N-1)!}} \qquad (3.5)$$

where

$\langle a \rangle$ average value of the fraction of the total scattered energy which is defined by the forward scattering phase function, where the average is taken over the range interval from R_c to $R-R_c$

$\frac{\langle P(\pi) \rangle_N}{P(\pi)}$ an average value for the backscatter phase function which is itself a function of phase function anisotropy, spatial inhomogeneity of the scattering medium and range to the scattering medium boundary

A_N a dimensionless coefficient which accounts for the variation of the multiple scattering contribution with respect to the dimensionless receiver field of view

$$\tau^2 = \frac{\psi^2}{\langle \theta_f^2 \rangle} \cdot \left(\frac{R}{R-R_c}\right)^2 \qquad (3.7a)$$

τ total optical depth between the lidar and the location of the backscattering event.

The coefficients A_N are defined in this paper by the value of P_N/P_1 in the limit of isotropic backscattering

$(\frac{\langle P(\pi)\rangle_N}{P(\pi)} = 1)$. The coefficients A_N are given as a function of the dimensionless receiver field of view τ^2 in Figs. 3.2 and 3.3, and in Table 3.1. The average value of the backscatter phase function $\frac{\langle P(\pi)\rangle_N}{P(\pi)}$ is then a complicated function of the remaining solution parameters such as phase function anisotropy and spatial inhomogeneity of the scattering medium. The value of the average backscatter phase function is examined in chapter 4.

The general formula for the contribution of multiple small angle scattering to the return signal of a coaxial monostatic lidar is

$$\frac{P_N}{P_1} = \tau^{N-1} \int_0^1 du_1 \int_0^{u_1} du_2 \cdots \int_0^{u_{N-2}} du_{N-1} \mathcal{A}_N \tag{3.35}$$

where

$$\mathcal{A}_N = \frac{\prod_{i=1}^{N-1} a(u_i)\rho(u_i)}{D_N} \{1-\exp[\frac{-D_N\psi^2}{C_N+\langle\theta_t^2\rangle D_N}]\} \tag{3.36}$$

$$C_N(u_1,\ldots,u_{N-1}) = (\frac{R-R_c}{R})^2 [\sum_{i=1}^{N-1} \langle\theta_f^2\rangle u_i^2 + \sum_{j=1}^{N-2} \sum_{k=j+1}^{N-1} \frac{\langle\theta_f^2\rangle u_j \langle\theta_f^2\rangle u_k}{\langle\theta_b^2\rangle} (u_j-u_k)^2] \tag{3.37a}$$

$$D_N(u_1,\ldots,u_{N-1}) = 1 + \sum_{i=1}^{N-1} \frac{\langle\theta_f^2\rangle u_i}{\langle\theta_b^2\rangle} (1 - \frac{R-R_c}{R} u_i)^2 \tag{3.37b}$$

and where

$R-R_c$ penetration depth to the location of the backscattering event, where R and R_c are the ranges from the lidar to the backscattering event location and the scattering medium boundary, respectively

u dimensionless penetration depth, $u = x/(R-R_c)$ where $0 \leq x \leq (R-R_c)$

$a(u)$ spatial structure of the fraction of the total scattered energy which is defined by the forward scattering phase function

τ optical penetration depth, $\tau = \int_0^{R-R_c} \beta(u)du$ where β is the optical extinction coefficient

$\rho(u)$ spatial structure of the optical extinction coefficient about its mean value $\rho(u) = \beta(u)\cdot(R-R_c)/\tau$

ψ receiver half width field of view

$\langle\theta_b^2\rangle$ mean square angle for backscattering by the atmosphere at range R

$\langle\theta_f^2\rangle_u$ mean square angle for forward scattering by the atmosphere at the dimensionless penetration depth u

$\langle\theta_t^2\rangle$ mean square angle of the transmitter beam pattern

The single scatter contribution for a coaxial monostatic lidar is given by

$$P_1(R) = \frac{\beta(R)\frac{P(\pi)}{4\pi}}{\pi\psi^2R^2} \exp\left[-2\int_0^R \beta(R')dR'\right]\cdot\left\{1-\exp\left[-\frac{\psi^2}{\langle\theta_t^2\rangle}\right]\right\} \qquad (3.39b)$$

Note that the multi-Gaussian approximations to the forward and backward scattering phase functions can be

obtained by summing the $\mathcal{L}_N$ of Eq. 3.35 over the appropriate combinations of $a(u_i)$, $\langle\theta_b^2\rangle_{u_i}$ and $\langle\theta_f^2\rangle_{u_i}$.

Chapter 4

THE EFFECTS OF MULTIPLE SCATTERING

The Neumann solution of chapter 3 can be used to calculate the effects of anisotropic backscattering on the contribution of multiple scattering to monostatic lidar return signals. In this chapter, the average backscatter phase function $\frac{\langle P(\pi)\rangle_N}{P(\pi)}$ is determined to explain the change in the contribution of N^{th} order scattering caused by backscatter phase function angular anisotropy. Some analytical and numerical results for the relation of $\frac{\langle P(\pi)\rangle_N}{P(\pi)}$ to the mean square angle ratio $Q = \langle\theta_f^2\rangle/\langle\theta_b^2\rangle$, range to the scattering medium boundary R_c, and linear spatial inhomogeneity of the scattering medium are presented in section 4.1. These results are then used in section 4.2 to provide simple approximations for the variation of $\frac{\langle P(\pi)\rangle_N}{P(\pi)}$ with respect to the ratio $\psi^2/\langle\theta_f^2\rangle$, Q, R_c and linear spatial inhomogeneity. The average backscatter phase function and the coefficients A_N can be used with Eq. 3.5 to calculate the N^{th} order scattering contribution to the return signal of a monostatic lidar. The coefficients A_N are given in Figs. 3.2 and 3.3, and in Table 3.1.

A multiple scattering correction to the lidar equation is derived in section 4.3 for lidar signals which

are obtained from rainfall. This section combines the multi-Gaussian scattering phase function results of chapter 2 [Eqs. 2.22 and 2.23] and the average phase function approximations of section 4.2 to derive the N^{th} order multiple scattering contribution to lidar signals which are obtained from rainfall. A multiple scattering correction factor after Kunkel and Weinman (1976) is defined in terms of the decrease in attenuation caused by the addition of multiply scattered light to the lidar return signal. It is shown that the multiple scattering correction factor is a variable but bounded function of the optical penetration depth.

4.1 The Average Backscatter Phase Function

A backscatter phase function average value $\frac{\langle P(\pi)\rangle_N}{P(\pi)}$ can be defined by the ratio of Neumann solutions for anisotropic and isotropic backscattering. The effective backscatter phase function is defined such that the N^{th} order scattering contribution is described by Eq. 3.5, and where $\frac{\langle P(\pi)\rangle_N}{P(\pi)} = 1$ for isotropic backscattering. It follows that

$$\frac{\langle P(\pi)\rangle_N}{P(\pi)} = \frac{P_N/P_1}{\lim\limits_{\langle\theta_b^2\rangle\to\infty} P_N/P_1} \qquad (4.1)$$

where P_N/P_1 is given by Eqs. 3.35-3.37. An inspection of Eqs. 3.35-3.37 reveals that the $\frac{\langle P(\pi)\rangle_N}{P(\pi)}$ are independent of penetration depth in the case of a spatially homogeneous medium with $R_c = 0$. Moreover, the average backscatter phase function varies uniquely with the ratios $Q = \langle\theta_f^2\rangle/\langle\theta_b^2\rangle$ and $\psi^2/\langle\theta_f^2\rangle$. The variation of $\frac{\langle P(\pi)\rangle_N}{P(\pi)}$ with the ratio $\psi^2/\langle\theta_f^2\rangle$ is shown in Fig. 4.1 for $2 \leq N \leq 6$ and $Q = 1$.

4.1a Limits for Large and Small Receiver Field of View

The $\frac{\langle P(\pi)\rangle_N}{P(\pi)}$ of Fig. 4.1 approach limiting values for large and small values of the ratio $\psi^2/\langle\theta_f^2\rangle$. In the limit of large receiver field of view with $\langle\theta_f^2\rangle$ fixed, $\lim_{\psi\to\infty} A_N = 1$ and the average backscatter phase function defined by Eq. 4.1 can be determined from the Neumann solution such that

$$\lim_{\psi\to\infty} \frac{\langle P(\pi)\rangle_N}{P(\pi)} = (N-1) \int_0^1 du_1 \int_0^{u_1} du_2 \cdots \int_0^{u_{N-2}} du_{N-1} \frac{\prod_{i=1}^{N-1} \frac{a(u_i)\,\rho(u_i)}{\langle a\rangle}}{1 + \sum_{i=1}^{N-1} Q_{u_i} \left(1 - \frac{R-R_c}{R} u_i\right)^2} \qquad (4.2)$$

This large ψ limit was already determined in section 3.1b for second order scattering from a spatially homogeneous medium (cf. Eq. 3.11), such that

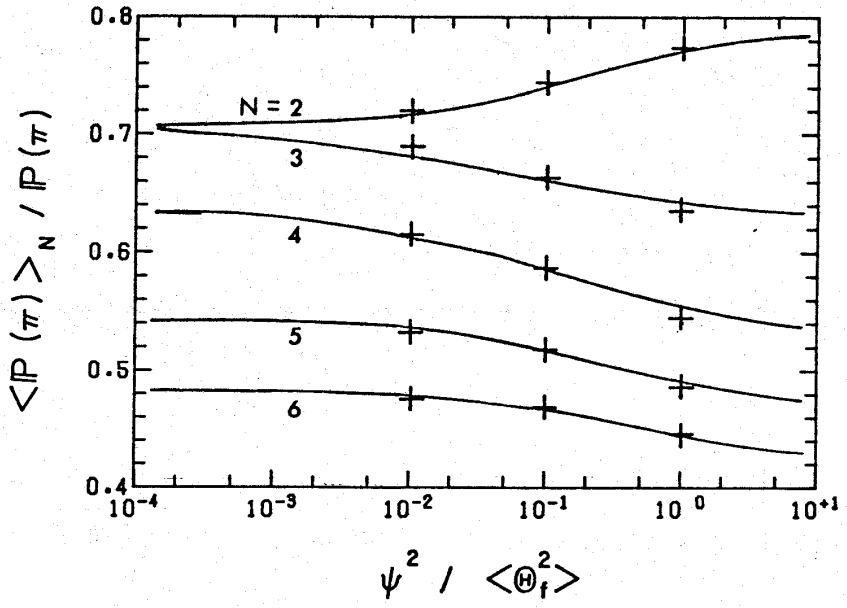

Fig. 4.1 The average backscatter phase function for a spatially homogeneous medium with $R_c = 0$, $Q = 1$ and $2 \leq N \leq 6$. The abscissa is given in terms of the ratio of squared half width receiver field of view to the mean square angle for forward scattering. The Eq. 4.11 approximation (+) for the average backscatter phase function variation with $\psi^2/\langle\Theta_f^2\rangle$ is included for comparison.

$$\lim_{\psi\to\infty} \frac{\langle \mathbb{P}(\pi)\rangle_2}{\mathbb{P}(\pi)} = \frac{R}{R-R_c}\frac{1}{\sqrt{Q}}\left\{\tan^{-1}\sqrt{Q} - \tan^{-1}\left[\sqrt{Q}\left(1-\frac{R-R_c}{R}\right)\right]\right\} \qquad (4.3)$$

where

$R-R_c$ penetration depth, where R_c is the distance between the scattering medium boundary and the lidar

$Q = \langle\Theta_f^2\rangle/\langle\Theta_b^2\rangle$ ratio of mean square angles for forward scattering and backscattering.

The large receiver field of view limits for $\frac{\langle \mathbb{P}(\pi)\rangle_N}{\mathbb{P}(\pi)}$ can be calculated using Eqs. 4.2 and 4.3, and they are

shown in Fig. 4.2 as a function of the mean square angle ratio Q for $2 \leq N \leq 6$.

The small ψ limits are difficult to determine since the P_N/P_1 approach zero and the division in Eq. 4.1 is indeterminate. In the case of double scattering, the average backscatter phase function limit for small ψ can be obtained from Eqs. 3.10 and 4.1 using l'Hospital's rule, such that

$$\lim_{\psi \to 0} \frac{\langle P(\pi) \rangle_2}{P(\pi)} = \frac{\lim_{\psi \to 0} \frac{\partial}{\partial \psi} P_2/P_1}{\lim_{\psi \to 0} \frac{\partial}{\partial \psi} \lim_{\langle \Theta_b^2 \rangle \to \infty} P_2/P_1} \tag{4.4}$$

Referring to Eq. 3.10 and using Leibniz's theorem for the differentiation of an integral, it follows that

$$\frac{\partial A_2}{\partial \psi} = \frac{-2\psi}{\langle \Theta_f^2 \rangle} \int_0^1 \exp\left\{ - \frac{1+Q\left(1 - \frac{R-R_c}{R} u\right)^2}{u^2} \frac{\psi^2}{\langle \Theta_f^2 \rangle} \right\} \frac{du}{u^2} \tag{4.5a}$$

Applying the transformation $u' = u^{-1}$, Eq. 4.5a can be readily integrated such that

$$\frac{\partial A_2}{\partial \psi} = \sqrt{\frac{\pi}{1+Q}} \frac{\exp\left[- \frac{1}{1+Q} \frac{\psi^2}{\langle \Theta_f^2 \rangle} \right]}{\sqrt{\langle \Theta_f^2 \rangle}} \operatorname{erfc}\left\{ \frac{\psi}{\sqrt{\langle \Theta_f^2 \rangle}} \left[\sqrt{1+Q} - \frac{R-R_c}{R} \frac{Q}{\sqrt{1+Q}} \right] \right\} \tag{4.5b}$$

Combining Eqs. 4.4 and 4.5a, it follows that

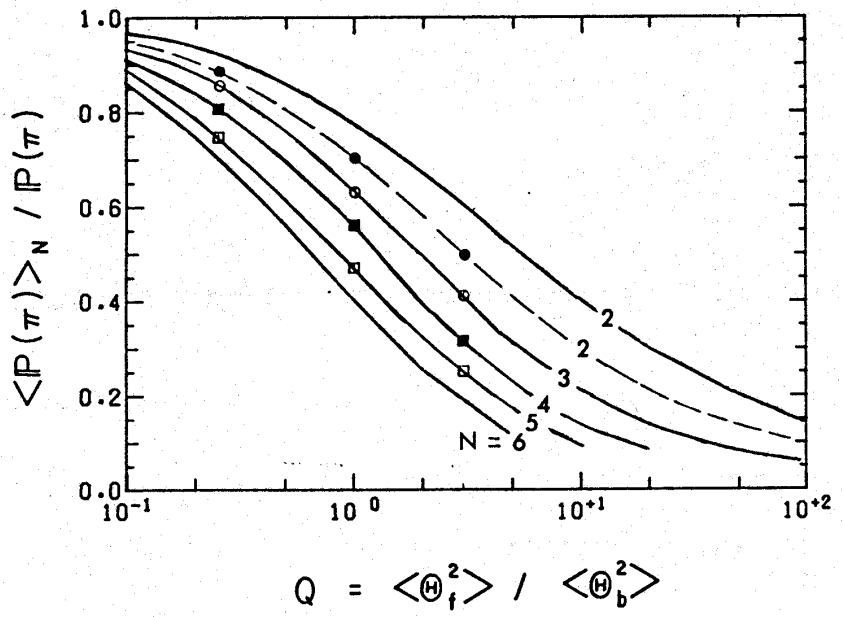

Fig. 4.2 The average backscatter phase function in the limits of large and small receiver field of view, plotted as a function of the mean square angle ratio Q with $2 < N < 6$. The large ψ limits (solid) are shown together with the small ψ limits for N = 2 (dash), N = 3 (•), N = 4 (o), N = 5 (■) and N = 6 (□). The small ψ limits for N = 2 and 3 are identical. The small ψ limits for N = 4,5,6 are numerically equal to the large ψ limits for N = 3,4,5 , respectively.

$$\lim_{\psi \to 0} \frac{\langle \mathbb{P}(\pi) \rangle_2}{\mathbb{P}(\pi)} = (1+Q)^{-1/2} \qquad (4.6)$$

where $Q = \langle \theta_f^2 \rangle / \langle \theta_b^2 \rangle$ is the ratio of the mean square angles for forward scattering and backscattering. The Eq. 4.6 result for the average backscatter phase function for N = 2 in the limit of small receiver field of view is included in Fig. 4.2.

The small receiver field of view limit $\lim_{\psi \to 0} \frac{\langle \mathbb{P}(\pi) \rangle_N}{\mathbb{P}(\pi)}$

was also calculated using Eqs. 3.35 - 3.37 for $Q = 0.25$, 1.0 and 3.0 with $3 \leq N \leq 6$, and these results are included in Fig. 4.2. The numerical results for $N = 3$ were found to be identical to the analytical result of Eq. 4.6 for $N = 2$. A relation between the large and small receiver field of view limits for higher values of N was also found for $4 \leq N \leq 6$, viz.

$$\lim_{\psi \to 0} \frac{\langle P(\pi) \rangle_N}{P(\pi)} \simeq \lim_{\psi \to \infty} \frac{\langle P(\pi) \rangle_{N-1}}{P(\pi)} \tag{4.7}$$

4.1b Large Receiver Field of View with Scattering Medium Boundary at R_c–

The backscatter phase function displays a unique functional dependence on the ratio of penetration depth to total range. This dependence is given exactly in the case for $N = 2$ by Eq. 4.3. For values of N greater than 2 in the limit of large R_c, it can be seen by inspection of Eqs. 3.35 - 3.37 that the average backscatter phase functions approach the limiting values

$$\lim_{R_c \to \infty} \frac{\langle P(\pi) \rangle_N}{P(\pi)} = \frac{1}{1+(N-1)Q} \tag{4.8}$$

where $Q = \langle \theta_f^2 \rangle / \langle \theta_b^2 \rangle$ is the ratio of the mean square angles

for forward scattering and backscattering. The Eq. 4.8 limit applies only in situations where the penetration depth is small in comparison to the distance of the scattering medium boundary R_c . Moreover, this large R_c limit is independent of the receiver field of view. The dependence fo the average backscatter phase function on $\frac{R-R_c}{R}$ was calculated for $2 \leq N \leq 4$ with $Q = 0.25$ and $Q = 3.0$, and these results are shown as a function of $\frac{R-R_c}{R}$ in Figs. 4.3. This dependence was calculated for $Q = 0.25$ and $Q = 3.0$ since these mean square angle ratios are expected to represent the phase function for rain, cf. Eqs. 2.22 and 2.23. The average backscatter phase functions of Figs. 4.3 attain their maximum values when the scattering medium boundary is located at the lidar, $\frac{R-R_c}{R} = 1$. The values of the average backscatter phase function decrease as the penetration depth $R-R_c$ becomes small with respect to the range of the backscattering event location R .

4.1c The Effect of Spatial Inhomogeneity

The effects of scattering medium inhomogeneity are examined in this section for the limit of large receiver field of view. The Neumann solution is determined in the large ψ limit for a linear distribution of the

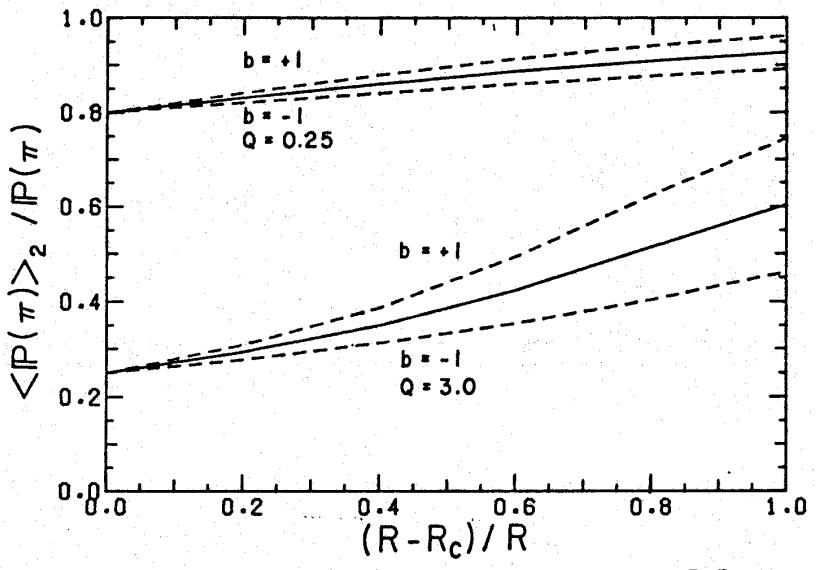

Fig. 4.3a Variation of $\frac{\langle P(\pi)\rangle_2}{P(\pi)}$ with respect to $\frac{R-R_c}{R}$ for a homogeneous spatial distribution of the extinction coefficient (solid), with $Q = 0.25$ (upper) and $Q = 3.0$ (lower). The results for a linear extinction coefficient distribution are also given for $b = \pm 1$, where b is defined in Eq. 4.9.

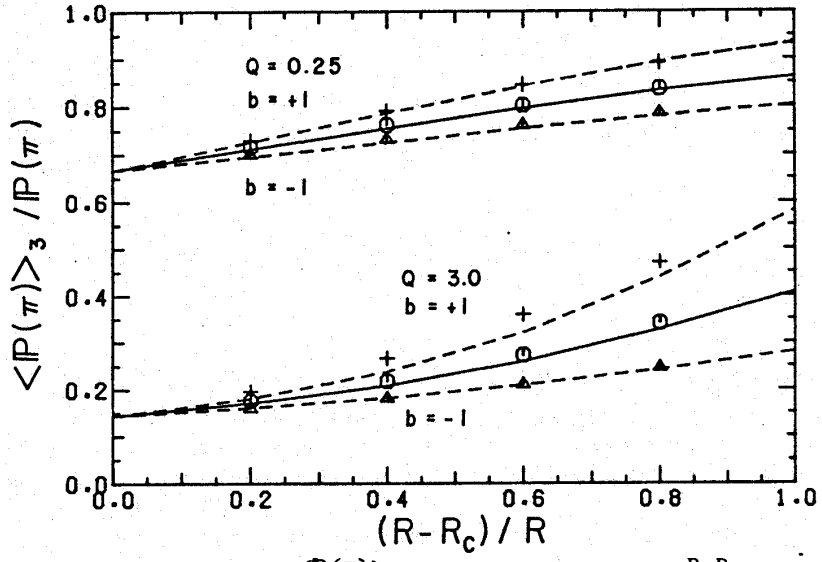

Fig.4.3b Variation of $\frac{\langle P(\pi)\rangle_3}{P(\pi)}$ with respect to $\frac{R-R_c}{R}$ for a homogeneous spatial distribution of the extinction coefficient (solid), with $Q = 0.25$ (upper) and $Q = 3.0$ (lower). The results for a linear extinction coefficient distribution are also given for $b = \pm 1$. The Eq. 4.12 approximation for $b = -1$ (Δ), $b = 0$ (o) and $b = +1$ (+) is included for comparison.

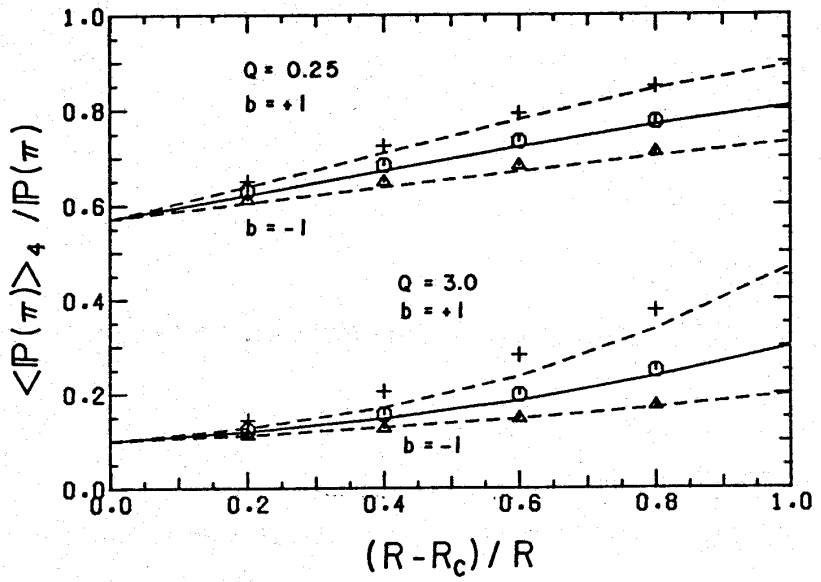

Fig. 4.3c Variation of $\frac{\langle \mathbb{P}(\pi) \rangle_4}{\mathbb{P}(\pi)}$ with respect to $\frac{R-R_c}{R}$ for a homogeneous spatial distribution of the extinction coefficient (solid), with $Q = 0.25$ (upper) and $Q = 3.0$ (lower). The results for a linear extinction coefficient distribution are also given for $b = \pm 1$. The Eq. 4.12 approximation for $b = -1$ (Δ), $b = 0$ (o) and $b = +1$ (+) is included for comparison.

extinction coefficient

$$\rho(u) = (1-b) + 2bu \tag{4.9}$$

where $-1 \leq b \leq +1$. Substituting this linear distribution into Eq. 4.2, the average backscatter phase function for $N = 2$ and large receiver field of view is

$$\lim_{\psi \to \infty} \frac{\langle \mathbb{P}(\pi) \rangle_2}{\mathbb{P}(\pi)} = [1+2b(\frac{R}{R-R_c} - \frac{1}{2})] \lim_{\psi \to \infty} \frac{\langle \mathbb{P}(\pi) \rangle_{2,b=0}}{\mathbb{P}(\pi)}$$

$$- \frac{b}{Q} (\frac{R}{R-R_c})^2 \ell n[\frac{1+Q}{1+Q(1-\frac{R-R_c}{R})^2}] \tag{4.10}$$

where $\frac{R-R_c}{R} \neq 0$ and $\lim_{\psi \to \infty} \frac{\langle P(\pi) \rangle_{2,b=0}}{P(\pi)}$ is given by Eq. 4.3. This result reduces to Eq. 4.8 in the limit of large R_c. Note that the Eq. 4.10 result for $N = 2$ is linear in the spatial distribution slope parameter b.

The effects of a linear extinction coefficient distribution on the value of the average backscatter phase function for $2 \leq N \leq 4$ are included in Figs. 4.3 for $b = \pm 1$. These results indicate that positive and negative slopes in the extinction coefficient spatial distribution will increase and decrease the values of $\frac{\langle P(\pi) \rangle_N}{P(\pi)}$, respectively.

4.2 Approximations for the Effects of Multiple Scattering

4.2a The Average Backscatter Phase Function

Several approximations which explain the variation of the average backscatter phase function with $\psi^2/\langle \theta_f^2 \rangle$, $Q = \langle \theta_f^2 \rangle / \langle \theta_b^2 \rangle$, R_c and linear spatial inhomogeneity are presented in this section. These approximations use the large and small receiver field of view limits for the average backscatter phase function as determined in section 4.1 to estimate the values of the average backscatter phase function at intermediate values of the ratio $\psi^2/\langle \theta_f^2 \rangle$. The variations of $\frac{\langle P(\pi) \rangle_N}{P(\pi)}$ with respect to $\frac{R-R_c}{R}$ and linear spatial inhomogeneity of the scattering

medium are estimated assuming proportionality of the large receiver field of view limits of $\frac{\langle P(\pi)\rangle_N}{P(\pi)}$ for $N \geq 3$ to the exact results for $N = 2$. The N^{th} order multiple scattering contribution to the return signal of a monostatic lidar can then be estimated using Eq. 3.5, where the coefficients A_N are given in Figs. 3.2 and 3.3, and in Table 3.1. The approximations of this section are summarized in section 4.4.

A simple approximation was determined to estimate the variation of the average backscatter phase function with respect to the ratio $\psi^2/\langle\Theta_f^2\rangle$ for $R_c = 0$ and $N \geq 3$. Using the limiting values of the average backscatter phase function for large and small receiver field of view, this approximation is

$$\frac{\langle P(\pi)\rangle_N}{P(\pi)} \simeq \lim_{\psi\to\infty} \frac{\langle P(\pi)\rangle_N}{P(\pi)} \left\{1-\left[1 - \frac{\lim_{\psi\to 0} \frac{\langle P(\pi)\rangle_N}{P(\pi)}}{\lim_{\psi\to\infty} \frac{\langle P(\pi)\rangle_N}{P(\pi)}}\right] e^{-K_1 \frac{\psi^2}{\langle\Theta_f^2\rangle}}\right\} \qquad (4.11a)$$

where

$$K_1 = \begin{cases} N & ; \quad N \leq 3 \\ \frac{16}{2^{N-1}} & ; \quad N \geq 4 \end{cases} \qquad (4.11b)$$

The phase function limits $\lim_{\psi\to 0} \frac{\langle P(\pi)\rangle_N}{P(\pi)}$ and $\lim_{\psi\to\infty} \frac{\langle P(\pi)\rangle_N}{P(\pi)}$ are given in graphical form in Fig. 4.2. The results of this approximation for $Q = 1$ are included in Fig. 4.1

for comparison to the results of the exact numerical solution. Eqs. 4.11 estimate the variation of the average backscatter phase function with $\psi^2/\langle\theta_f^2\rangle$ to within $\pm 5\%$ for $R_c = 0$ with $2 \leq N \leq 6$.

The functional dependence of the backscatter phase function on the ratio of penetration depth to the range of the backscattering event location $\frac{R-R_c}{R}$ can be approximated for $N \geq 3$ by a simple relation which uses the exact results for $N = 2$, such that

$$\lim_{\psi\to\infty} \frac{\langle P(\pi)\rangle_N}{P(\pi)} \simeq \frac{1}{1+(N-1)Q} + \left[\lim_{R_c\to 0} \lim_{\psi\to\infty} \frac{\langle P(\pi)\rangle_N}{P(\pi)} - \frac{1}{1+(N-1)Q}\right] \cdot$$

$$\cdot \left[\frac{\lim_{\psi\to\infty} \frac{\langle P(\pi)\rangle_2}{P(\pi)} - \frac{1}{1+Q}}{\lim_{R_c\to 0} \lim_{\psi\to\infty} \frac{\langle P(\pi)\rangle_N}{P(\pi)} - \frac{1}{1+Q}}\right] \qquad (4.12)$$

where $\lim_{\psi\to\infty} \frac{\langle P(\pi)\rangle_2}{P(\pi)}$ is given by Eq. 4.3 and $\lim_{R_c\to 0} \lim_{\psi\to\infty} \frac{\langle P(\pi)\rangle_N}{P(\pi)}$ is given in Fig. 4.2. The results of this approximation are included in Figs. 4.3b and 4.3c for comparison to the exact results in the limit of large receiver field of view. The Eqs. 4.11 approximation was also used to estimate the variation of the average backscatter phase function with $\frac{R-R_c}{R}$ at finite values of the ratio $\psi^2/\langle\theta_f^2\rangle$, and an estimation accuracy similar to that shown in Figs. 4.3b and 4.3c for the large ψ

limit was observed.

The Eq. 4.12 approximation can also be used to estimate the variation of the average backscatter phase function with respect to both $\frac{R-R_c}{R}$ and the linear spatial distribution slope b. The results of this procedure for $3 \leq N \leq 4$ and $b = \pm 1$ are included in Figs. 4.3b and 4.3c for comparison to the results of the exact numerical solution. The variation of the average backscatter phase function with respect to linear spatial inhomogeneity of the scattering medium are not negligible. This implies that a complete solution of Eqs. 3.35 - 3.37 is required when lidar signals are obtained from media exhibiting a high degree of spatial inhomogeneity.

The average backscatter phase functions can be obtained from Fig. 4.2 when the receiver field of view is large in comparison to the width of the forward scattering phase function. Since the cost of calculating the average backscatter phase function for large N can be prohibitive, a simple approximation was determined to predict the large ψ limits of $\frac{\langle \mathbb{P}(\pi) \rangle_N}{\mathbb{P}(\pi)}$ for $N \geq 3$, namely

$$\lim_{R_c \to 0} \lim_{\psi \to \infty} \frac{\langle \mathbb{P}(\pi) \rangle_N}{\mathbb{P}(\pi)} \simeq \lim_{R_c \to 0} \lim_{\psi \to \infty} \frac{\langle \mathbb{P}(\pi) \rangle_2}{\mathbb{P}(\pi)} \cdot \left(\frac{N}{2}\right)^{-K_2(Q,b)} \qquad (4.13)$$

where $-1 \leq b \leq +1$. The power $K_2(Q,b)$ of Eq. 4.13 is

given in Fig. 4.4 as a function of the ratio of the mean square angles for forward scattering and backscattering Q, and it is also given in Table 4.1 for $Q = 3.0$, 0.25 and 0.01. The results of the Eq. 4.13 approximation for $b = 0$ are included in Table 4.1 for comparison to the exact values from Fig. 4.2 for $3 \leq N \leq 6$.

The procedure for approximating the average backscatter phase function for $N \geq 3$ using Eqs. 4.11-4.13 can be summarized as follows:

(a) determine the large ψ limit of $\frac{\langle P(\pi)\rangle_N}{P(\pi)}$ for $N \geq 3$ and $R_c = 0$ using Eq. 4.13, where $\lim_{R_c \to 0} \lim_{\psi \to \infty} \frac{\langle P(\pi)\rangle_2}{P(\pi)}$ is given by Eq. 4.10 with $R_c = 0$, and $K_2(Q,b)$ is given in Fig. 4.4.

(b) determine the variation of $\lim_{\psi \to \infty} \frac{\langle P(\pi)\rangle_N}{P(\pi)}$ with respect to $R_c \neq 0$ using Eq. 4.12, where $\lim_{R_c \to 0} \lim_{\psi \to \infty} \frac{\langle P(\pi)\rangle_N}{P(\pi)}$ was determined in step (a) and $\lim_{\psi \to \infty} \frac{\langle P(\pi)\rangle_2}{P(\pi)}$ is given by Eq. 4.10 with $R_c = 0$.

(c) finally, determine the variation of $\frac{\langle P(\pi)\rangle_N}{P(\pi)}$ with respect to $\psi^2/\langle\theta_f^2\rangle$ using Eqs. 4.11, where $\lim_{\psi \to \infty} \frac{\langle P(\pi)\rangle_N}{P(\pi)}$ was determined in step (b) and

$$\lim_{\psi \to 0} \frac{\langle P(\pi)\rangle_3}{P(\pi)} = \lim_{\psi \to 0} \frac{\langle P(\pi)\rangle_2}{P(\pi)} = (1+Q)^{-1} \tag{4.6}$$

$$\lim_{\psi \to 0} \frac{\langle P(\pi)\rangle_N}{P(\pi)} = \lim_{\psi \to \infty} \frac{\langle P(\pi)\rangle_{N-1}}{P(\pi)}; \quad N \geq 4 \tag{4.7}$$

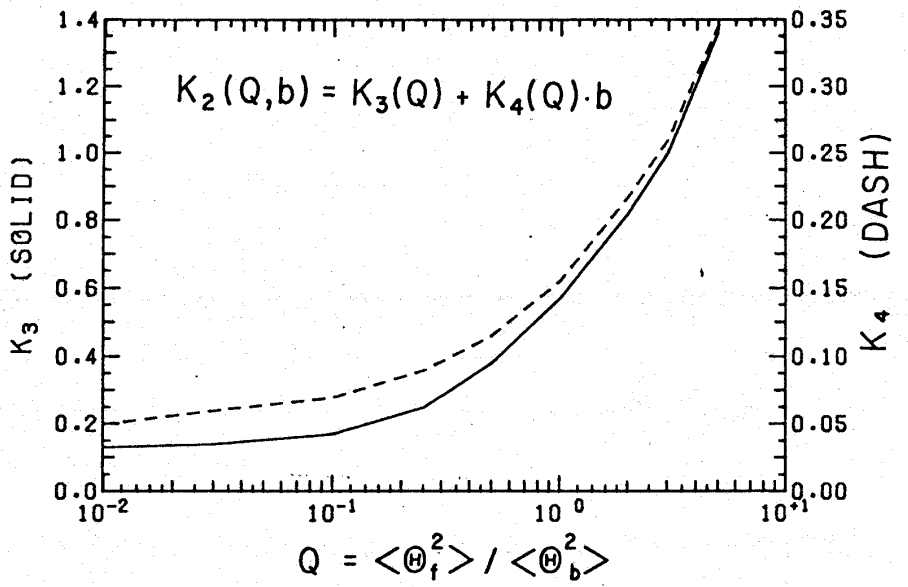

Fig. 4.4 The power $K_2(Q,b)$ of Eq. 4.13 as a function of the ratio of the mean square angles for forward scattering and backscattering Q . This factor is given in terms of the linear equation $K_2(Q,b) = K_3(Q) + K_4(Q)\cdot b$.

Table 4.1

Comparison of the Eq. 4.13 Approximation for the Average Backscatter Phase Function of Rain in the Limit of Large Receiver Field of View with b = 0

	Q = 0.01		Q = 0.25		Q = 3.0	
N	K_2 = 0.13-0.05b		K_2 = 0.25-0.09b		K_2 = 1.0-0.26b	
	exact	approx	exact	approx	exact	approx
2	0.997	--	0.927	--	0.605	--
3	0.94	0.95	0.86	0.84	0.41	0.40
4	0.91	0.91	0.81	0.78	0.30	0.30
5	0.89	0.89	0.75	0.74	0.23	0.24
6	0.86	0.86	0.71	0.70	0.19	0.20

The small ψ limits of the average backscatter phase function are independent of both R_c and the linear spatial distribution slope parameter b. Note that when the penetration depth $R-R_c$ is small in comparison to the range of the backscattering event location R, then the average backscatter phase function is again independent of both R_c and the linear spatial distribution slope parameter b, and the average backscatter phase function is given by Eq. 4.8

4.2b Single Gaussian Approximations to Multi-Gaussian Phase Functions

The small angle multiple scattering contribution approximations of section 4.2a are given for phase functions which are characterized by single Gaussian functions. A method for calculating the multiple scattering contribution for multi-Gaussian phase functions using these single Gaussian approximations is presented in this section.

The results of section 4.2a can be applied directly to multi-Gaussian backscatter phase functions since multiple large angle scattering contributions to the return signal are neglected in this formulation. The contributions of each Gaussian component of the backscatter phase

function are therefore independent, and it follows by superposition that

$$\left.\frac{P_N}{P_1}\right|_{\text{total}} = \frac{\sum_{s=1}^{S} P_s(\pi) \left.\frac{P_N}{P_1}\right|_s}{\sum_{s=1}^{S} P_s(\pi)} \tag{4.14}$$

The angular deflections due to multiple forward scattering arise from Gaussian phase function components which have different widths and amplitudes, and it follows that the effects of a multi-Gaussian forward phase function cannot be accounted for by a relation of the form of Eq. 4.14. As shown by Eloranta (1972) for double scattering, the return signal in the limit of small receiver field of view will be composed primarily of photons which have undergone multiple forward scatterings at $\Theta \sim 0$. It follows in this case that the magnitude of the multiple scatter contribution is determined by the amplitude of the forward scattering phase function. The equivalent single Gaussian forward phase function can therefore be approximated by a Gaussian function with the same total area and a mean square width defined by

$$\langle \Theta_f^2 \rangle^{-1} \simeq \frac{\sum_i \frac{a_i}{\langle \Theta_f^2 \rangle_i}}{\sum_i a_i} \tag{4.15a}$$

In the large receiver field of view limit, the total angular deflection can be approximated by the sum of angular deflections which arise from each component of the multi-Gaussian forward phase function. It follows in this case that the equivalent single Gaussian forward phase function can be approximated by a Gaussian function with the same total area and a mean square width defined by

$$\langle\Theta_f^2\rangle \simeq \frac{\sum_i a_i \langle\Theta_f^2\rangle_i}{\sum_i a_i} \qquad (4.15b)$$

The multiple scattering contribution was calculated from Eqs. 3.35-3.37 using the Nimbostratus triple Gaussian forward phase function of Weinman (1976) with isotropic backscattering, cf. Table 4.2. The exact solution for the triple Gaussian Nimbostratus phase function was used to calculate the quantity $A_N/(2a)^{N-1}$, and these results are compared to the results for a single Gaussian forward phase function in Fig. 4.5 for $N = 3$. The triple Gaussian results are shown for equivalent $\langle\Theta_f^2\rangle$ values defined by both Eqs. 4.15a and 4.15b. It can be seen from Fig. 4.5 that Eq. 4.15a is valid when the dimensionless receiver field of view $T^2 \lesssim 10^{-2}$, and that Eq. 4.15b is valid when $T^2 \gtrsim 10^0$. The width of the equivalent single Gaussian forward phase function must be extrapolated from Eqs. 4.15 when $10^{-2} < T^2 < 10^0$.

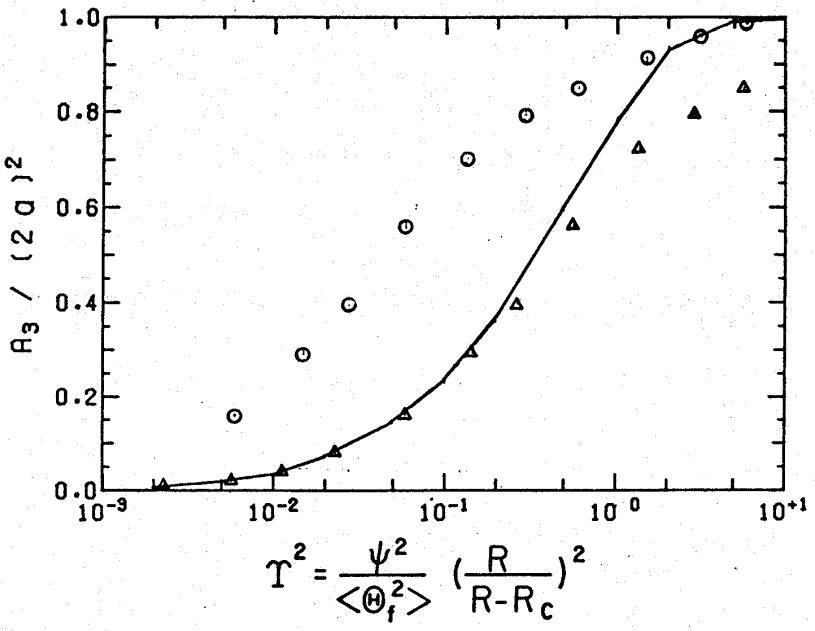

Fig. 4.5 A comparison of the multiple scattering coefficient $A_N/(2a)^{N-1}$ for the triple Gaussian Nimbostratus (Δ and o) and single Gaussian (solid) forward phase functions with $N = 3$. The width of the equivalent single Gaussian for the Nimbostratus forward phase function was calculated using Eq. 4.15a (Δ) and Eq. 4.15b (o) for the small and large limits of the dimensionless receiver field of view τ^2 , respectively.

Table 4.2

The Nimbostratus Forward Scattering Phase Function of Weinman (1976)

i	a_i	$\langle\theta_f^2\rangle_i$	
1	0.37	1.13×10^{-4}	rad^2
2	0.09	6.76×10^{-4}	rad^2
3	0.08	8.85×10^{-3}	rad^2
Equivalent single Gaussian	0.54	1.58×10^{-4}	rad^2 (Eq. 4.15a)
		1.50×10^{-3}	rad^2 (Eq. 4.15b)

4.3 A Multiple Scattering Correction Factor for Rain

This section examines the effect of multiple scattering on the form of the lidar equation. In comparison to single scattering, multiple small angle forward scattering increases the amount of light which is available for backscattering, and therefore increases the amount of light which is collected by a monostatic lidar. This signal enhancement can be thought of as either an increase in the atmospheric backscatter cross section, or a decrease in atmospheric attenuation. Platt (1973), Shipley et al. (1974), and Kunkel and Weinman (1976) account for multiple scattering as a decrease in the extinction coefficient by introducing an effective extinction coefficient β_{eff} in the attenuation term of the lidar equation (cf. Eq. 1.2). Following the notation of Kunkel and Weinman, the effective extinction coefficient is

$$\beta_{eff} = [1-F(\tau)]\cdot\beta \qquad (4.16)$$

where $1-F(\tau)$ is a multiple scattering correction factor. Single scattering is dominant in cases of small optical penetration depths where the receiver field of view is small in comparison to the mean square angle for forward scattering, such that $F \sim 0$. The value of F increases when multiple scattering accounts for larger portions

of the return lidar signal. When the scattering medium is composed of very large particles, for example, one half of the scattered energy is diffracted in the forward direction through small angles. When the receiver field of view is larger than these deflections, then one half of the scattered energy continues to propagate in the same direction as the unscattered light and $F \sim 1/2$. The variation of F with τ and with the spatial structure of the scattering medium is discussed in the remainder of this section.

Substituting Eq. 4.16 into the lidar equation (Eq. 1.2), the ratio of the total return signal to that due to single scattering only is

$$\frac{P_{total}(R)}{P_1(R)} = \exp\{+2\int_0^R \beta \cdot F(R) \cdot dR\} \qquad (4.17a)$$

The multiple scattering correction factor can therefore be expressed as a function of optical depth, such that

$$F(\tau) = 1/2 \, \frac{d}{d\tau} \, \ell n\left(\frac{P_{total}}{P_1}\right) \qquad (4.17b)$$

where $F(\tau)$ is a unique function of the lidar system geometry and the scattering medium spatial distribution. The multiple scattering correction factor can be represented in terms of the average backscatter phase function when Eq. 3.5 is used to describe the contributions of

N^{th} order scattering to the return lidar signal, such that

$$F(\tau) = \frac{1}{2} \frac{A_2 \frac{\langle P(\pi)\rangle_2}{P(\pi)} + A_3 \frac{\langle P(\pi)\rangle_3}{P(\pi)} \frac{\tau}{1!} + \cdots}{1 + A_2 \frac{\langle P(\pi)\rangle_2}{P(\pi)} \frac{\tau}{1!} + A_3 \frac{\langle P(\pi)\rangle_3}{P(\pi)} \frac{\tau^2}{2!} + \cdots} \qquad (4.18)$$

In the limits of large receiver field of view and isotropic backscattering, the coefficients $A_N \frac{\langle P(\pi)\rangle_N}{P(\pi)}$ approach unity and $\lim_{\langle \theta_b^2 \rangle \to \infty} \lim_{\psi \to \infty} F(\tau) = 1/2$. In the limit of small receiver field of view and negligible transmitter beam divergence, the coefficients A_N approach zero and $\lim_{\psi \to 0} F(\tau) = 0$.

The scattering phase function parameters for rainfall can be obtained from the results of chapter 2 for the scattering phase functions of spherical water drop polydispersions which are described by the size distributions of Marshall and Palmer or Joss and Gori. Using the single Gaussian approximation for the diffraction phase function (Eq. 2.23), the mean square angle ratios Q for the triple Gaussian backscatter phase function approximation (Eq. 2.22) are $Q = 3.0$, 0.25 and 0.01.[1]

---

[1] The Neumann solution was obtained using both the triple Gaussian (Eq. 2.21b) and single Gaussian (Eq. 2.23) approximations for the forward scattering phase function due to diffraction. The results were identical in the large receiver field of view limit which is characteristic of lidar operation in rainfall, and the time consuming triple Gaussian approximation to the diffraction phase function need not be applied.

These Gaussians define 55%, 30% and 15% of the non-geometrical optics portion of the backscatter phase function, respectively. Note that these mean square angle ratios are independent of the extinction coefficient magnitude when the rain drop size distributions are given by the distributions of Marshall and Palmer or Joss and Gori.

The multiple scattering correction factor for spatially homogeneous rain in the limit of large ψ is shown as a function of optical penetration depth in Fig. 4.6. This correction factor is shown for both $R_c = 0$ and $R_c \to \infty$, as well as for several cases where the medium boundary is situated at intermediate distances. The $R_c = 0$ and $R_c \to \infty$ cases give lower and upper limits on the value of $1-F(\tau)$, respectively, and all of these results converge as the value of τ becomes large. It can also be seen from Fig. 4.6 that the multiple scattering correction factor for a homogeneous medium can be approximated by linear segments in τ when $R_c = 0$, such that

$$1-F(\tau) \sim \begin{cases} 0.62 - 0.02\tau & ; \tau \leq 3.5 \\ 0.55 & ; 3.5 < \tau \leq 5.5 \\ 0.55 + 0.02\,(\tau-5.5) & ; 5.5 < \tau \leq 7.5 \end{cases} \qquad (4.19)$$

The multiple scattering correction factor for several spatially inhomogeneous distributions of rain in the limit

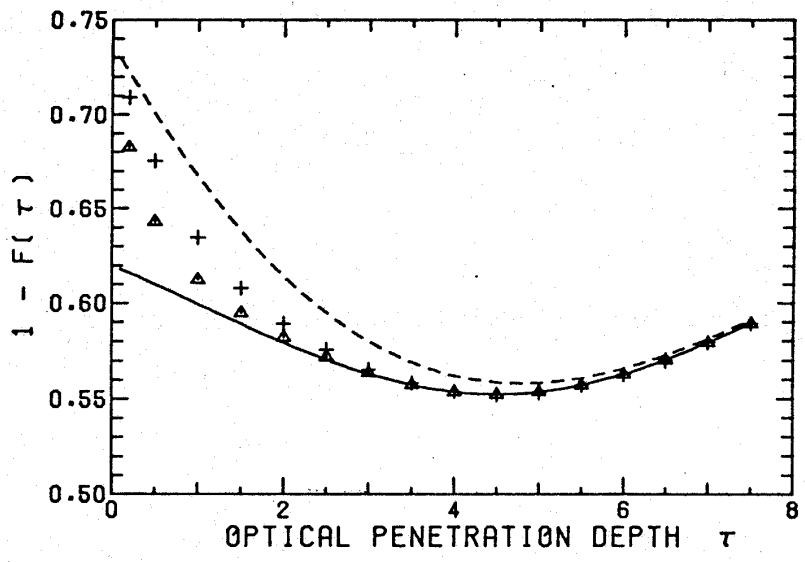

Fig. 4.6 The multiple scattering correction factor 1-F(τ) for spatially homogeneous rain, plotted as a function of optical penetration depth for $R_c = 0$ (solid) and $R_c \to \infty$ (dash). The correction factor is also shown for $\beta = 1.0$ km^{-1} with $R_c = 0.025$ km (Δ) and $R_c = 1.0$ km (+) .

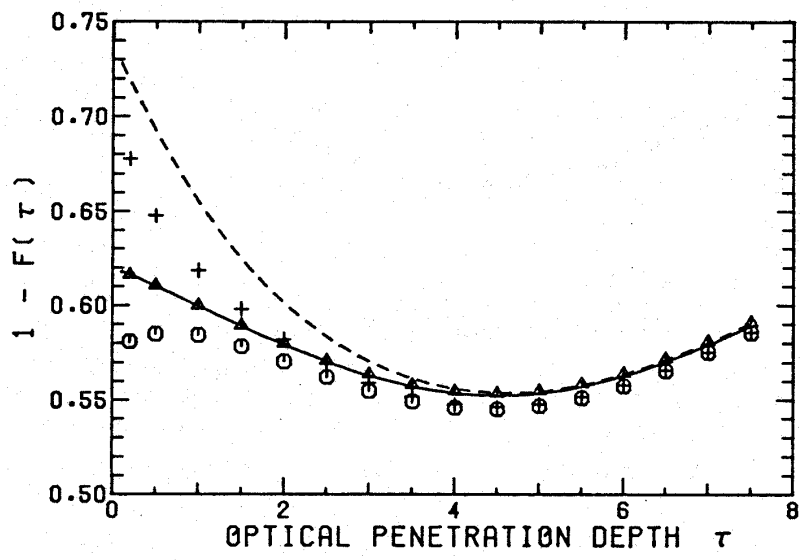

Fig. 4.7 The multiple scattering correction factor 1-F(τ) for several linear spatial distributions of the rainfall optical extinction coefficient, plotted as a function of the optical penetration depth. The correction factor is shown for $\beta(km^{-1}) = R-R_c$ with $R_c = 0$ (Δ) and $R_c = 1$ km (+) , as well as for $\beta(km^{-1}) = 4-(R-R_c)$ with $R_c = 0$ (o) and $R_c = 1$ km (dash). The spatially homogeneous result for $R_c = 0$ is included for comparison (solid).

of large receiver field of view are shown in Fig. 4.7.

These results indicate that the multiple scattering correction factor can be approximated by Eq. 4.19 in most cases encountered by lidar operation in rainfall. At small optical penetration depths, the largest error which would be incurred by the use of Eq. 4.19 is on the order of $\pm 20\%$. It can be concluded that the value of $1-F(\tau)$ departs from the value of 0.5 for isotropic backscattering due to the presence of the "glory" in the backscatter phase function of rainfall.

4.4 Summary of the Approximations for Multiple Scattering

The average backscatter phase function and the coefficients A_N can be used to calculate the N^{th} order scattering contribution to the return signal of a monostatic lidar using Eq. 3.5, viz.

$$\boxed{\frac{P_N}{P_1} = 2^{N-1} \langle a \rangle^{N-1} \frac{\langle P(\pi) \rangle_N}{P(\pi)} A_N \frac{\tau^{N-1}}{(N-1)!}} \qquad (3.5)$$

where $\langle a \rangle$ is the mean value of the fraction of total scattered energy which is defined by the forward scattering phase function. The coefficients A_N are given in Figs. 3.2 and 3.3, and in Table 3.1. The average backscatter phase function $\frac{\langle P(\pi) \rangle_N}{P(\pi)}$ was investigated in

sections 4.1 and 4.2, and the exact and approximate results of these sections for the values of $\frac{\langle P(\pi)\rangle_N}{P(\pi)}$ are summarized below.

Several exact results for the average backscatter phase function with $N = 2$ were obtained in section 4.1. The second order average backscatter phase function for a spatially homogeneous medium with large receiver field of view $[\psi^2 \gg \langle\theta_f^2\rangle]$ is

$$\lim_{\psi\to\infty} \frac{\langle P(\pi)\rangle_{2,b=0}}{P(\pi)} = \frac{R}{R-R_c}\frac{1}{\sqrt{Q}}\left\{\tan^{-1}\sqrt{Q} - \tan^{-1}\left[\sqrt{Q}\left(1-\frac{R-R_c}{R}\right)\right]\right\} \qquad (4.3)$$

where

$R-R_c$ penetration depth, where R_c is the distance between the scattering medium boundary and the lidar

$Q = \langle\theta_f^2\rangle/\langle\theta_b^2\rangle$ ratio of the mean square angles for forward scattering and backscattering.

In the limit of small receiver field of view, the second order average backscatter phase function is

$$\lim_{\psi\to 0} \frac{\langle P(\pi)\rangle_2}{P(\pi)} = (1+Q)^{-\frac{1}{2}} \qquad (4.6)$$

The Eq. 4.6 result is independent of the range to the scattering medium boundary R_c. When the optical extinction coefficient of the scattering medium is distributed linearly with range, such that

$$\rho(u) = (1-b) + 2bu \tag{4.9}$$

then

$$\lim_{\psi\to\infty} \frac{\langle P(\pi)\rangle_2}{P(\pi)} = [1+2b(\frac{R}{R-R_c} - \frac{1}{2})] \lim_{\psi\to\infty} \frac{\langle P(\pi)\rangle_{2,b=0}}{P(\pi)}$$

$$- \frac{b}{Q} (\frac{R}{R-R_c})^2 \ln[\frac{1+Q}{1+Q(1-\frac{R-R_c}{R})^2}] \tag{4.10}$$

where $\lim_{\psi\to\infty} \frac{\langle P(\pi)\rangle_{2,b=0}}{\langle P(\pi)\rangle}$ is given by Eq. 4.3. The function $\rho(u) = \beta(u)/\langle\beta\rangle$ is the spatial structure of the optical extinction coefficient about the mean value $\langle\beta\rangle = \tau/(R-R_c)$.

The procedure for approximating the average backscatter phase function for $N \geq 3$ using Eqs. 4.11-4.13 can be summarized as follows:

(a) determine the large ψ lim of $\frac{\langle P(\pi)\rangle_N}{P(\pi)}$ for $N \geq 3$ and $R_c = 0$ using

$$\lim_{R_c\to 0} \lim_{\psi\to\infty} \frac{\langle P(\pi)\rangle_N}{P(\pi)} \simeq \lim_{R_c\to 0} \lim_{\psi\to\infty} \frac{\langle P(\pi)\rangle_2}{P(\pi)} \cdot (\frac{N}{2})^{-K_2(Q,b)} \tag{4.13}$$

where $\lim_{R_c\to 0} \lim_{\psi\to\infty} \frac{\langle P(\pi)\rangle_2}{P(\pi)}$ is given by Eq. 4.10 with $R_c = 0$ and $K_2(Q,b)$ is given in Fig. 4.4.

(b) determine the variation of $\lim_{\psi\to\infty} \frac{\langle P(\pi)\rangle_N}{P(\pi)}$ with respect to $R_c \neq 0$ using

$$\lim_{\psi\to\infty}\frac{\langle P(\pi)\rangle_N}{P(\pi)} \simeq \frac{1}{1+(N-1)Q} + \left[\lim_{R_c\to 0}\lim_{\psi\to\infty}\frac{\langle P(\pi)\rangle_N}{P(\pi)} - \frac{1}{1+(N-1)Q}\right]\cdot$$

$$\cdot\left[\frac{\lim_{\psi\to\infty}\frac{\langle P(\pi)\rangle_2}{P(\pi)} - \frac{1}{1+Q}}{\lim_{R_c\to 0}\lim_{\psi\to\infty}\frac{\langle P(\pi)\rangle_N}{P(\pi)} - \frac{1}{1+Q}}\right] \qquad (4.12)$$

where $\lim_{R_c\to 0}\lim_{\psi\to\infty}\frac{\langle P(\pi)\rangle_N}{P(\pi)}$ was determined in step (a) and $\lim_{\psi\to\infty}\frac{\langle P(\pi)\rangle_2}{P(\pi)}$ is given by Eq. 4.10 with $R_c = 0$.

(c) finally, determine the variation of $\frac{\langle P(\pi)\rangle_N}{P(\pi)}$ with respect to $\psi^2/\langle\Theta_f^2\rangle$ using

$$\frac{\langle P(\pi)\rangle_N}{P(\pi)} \simeq \lim_{\psi\to\infty}\frac{\langle P(\pi)\rangle_N}{P(\pi)}\left\{1-\left[1-\frac{\lim_{\psi\to 0}\frac{\langle P(\pi)\rangle_N}{P(\pi)}}{\lim_{\psi\to\infty}\frac{\langle P(\pi)\rangle_N}{P(\pi)}}\right]e^{-K_1\frac{\psi^2}{\langle\Theta_f^2\rangle}}\right\} \qquad (4.11a)$$

where

$$K_1 = \begin{cases} N & N \le 3 \\ \frac{16}{2^{N-1}}\,; & N \ge 4 \end{cases} \qquad (4.11b)$$

The average backscatter phase function $\lim_{\psi\to\infty}\frac{\langle P(\pi)\rangle_N}{P(\pi)}$ was determined in step (b). In addition, the small receiver field of view limits of the average backscatter phase function are given by

$$\lim_{\psi\to 0} \frac{\langle P(\pi)\rangle_3}{P(\pi)} = \lim_{\psi\to 0} \frac{\langle P(\pi)\rangle_2}{P(\pi)} = (1+Q)^{-1} \tag{4.6}$$

$$\lim_{\psi\to 0} \frac{\langle P(\pi)\rangle_N}{P(\pi)} = \lim_{\psi\to \infty} \frac{\langle P(\pi)\rangle_{N-1}}{P(\pi)} \; ; \quad N \geq 4 \tag{4.7}$$

A multiple scattering correction factor $1-F(\tau)$ for rain after Kunkel and Weinman (1976) can be calculated using the average backscatter phase function approximations of section 4.2. An effective extinction coefficient is defined such that $\beta_{eff} = [1-F(\tau)]\beta$, where $F(\tau)$ is a unique function of the lidar system geometry and the scattering medium spatial distribution of the optical extinction coefficient. The multiple scattering correction factor can be approximated to $\pm 20\%$ using the results for a spatially homogeneous medium, such that

$$1 - F(\tau) \sim \begin{cases} 0.62 - 0.02\,\tau & ; \quad \tau \leq 3.5 \\ 0.55 & ; \quad 3.5 < \tau < 5.5 \\ 0.55 + 0.02(\tau - 5.5) & ; \quad 5.5 \leq \tau \lesssim 7.5 \end{cases} \tag{4.19}$$

The variation in the multiple scattering correction factor of Fig. 4.7 with respect to scattering medium spatial inhomogeneity indicates that a complete Neumann solution (Eqs. 3.35-3.37) is required when lidar signals are obtained from media exhibiting a high degree of spatial inhomogeneity.

Chapter 5

LIDAR OBSERVATIONS OF RAIN

This chapter utilizes the results of chapters 2, 3 and 4 to derive the subcloud spatial distribution of the optical extinction coefficient from monostatic lidar signals during rainfall events. The rainfall scattering phase function approximations of chapter 2 are used to model the relationship of the rainfall backscatter phase function to the optical extinction coefficient β_r. These results were used in section 4.3 to calculate a rainfall multiple scattering correction factor to the lidar equation, and this correction factor is now applied to the extraction of the optical extinction coefficient from monostatic lidar signals obtained from rainfall.

The multiple scattering results of chapters 3 and 4 indicate that receiver field of view techniques may provide an estimation of the drop size distribution. A simple receiver field of view experiment was performed to measure the contribution of drops with diameters ~0.1 mm to the total optical depth by distinguishing the spatial and angular spreading of the transmitted beam caused by multiple scattering. The presence of this drop size was independently verified by simultaneous filter paper measurements of the drop size distribution.

The results of this receiver field of view experiment are discussed in section 5.1.

Procedures for obtaining the range variation of the optical extinction coefficient from monostatic lidar signals are examined in section 5.2. A method which derives range profiles of the rainfall optical extinction coefficient from uncalibrated monostatic lidar signals is presented, and it is shown that this method estimates the actual value of the optical extinction coefficient to within a standard deviation of $\pm 20\%$. Several spatial distributions of the optical extinction coefficient are then derived from uncalibrated monostatic lidar information obtained during rainfall events by the UW lidar system. An RHI time sequence of the subcloud spatial distribution of β_r is examined in section 5.3.

5.1 Some Experimental Observations of Multiple Scattering

The UW lidar was used to measure the variation of the multiple scattering contribution to monostatic lidar signals with respect to receiver field of view. The multiple scattering theory of chapters 3 and 4 predicts that measureable variations in the multiple scattering contribution will be observed when the width of the atmospheric forward scattering phase function and the receiver field

of view are approximately equal. Using Eq. 2.23 to describe the forward scattering phase function, then the largest signal variations caused by the variation of receiver field of view will occur when

$$\psi^2 \sim \langle\theta_f^2\rangle \sim \frac{4}{3}\left(\frac{\lambda}{\pi\langle D\rangle}\right)^2 \tag{5.1}$$

where $\langle D\rangle$ is a representative drop diameter and $\lambda = 694.3$ nm is the UW lidar transmitter wavelength. The UW lidar half width receiver field of view can be continuously varied from 1 to 5 mrad. Variations in the return signal due to a variation in ψ should therefore be observed when the atmosphere consists mainly of drops with diameters on the order of 0.1mm($\pm$ a factor of three).

The effective extinction coefficient can be measured by taking the range derivative or "slope" of lidar signals which are obtained from spatially homogeneous rain. The slope method was applied to lidar returns from spatially homogeneous rain to obtain the effective extinction coefficient β_{eff} as a function of the receiver field of view ψ, and a measurement of the variation in β_{eff} with ψ during a post thunderstorm drizzle on 18 June, 1975 is shown in Fig. 5.1. Referring to Figs. 3.2 and 4.2 for the relation of $A_N \frac{\langle P(\pi)\rangle_N}{P(\pi)}$ to $\psi^2/\langle\theta_f^2\rangle$, Eq. 4.18 predicts that β_{eff} will increase or decrease as the receiver field of view is decreased or increased,

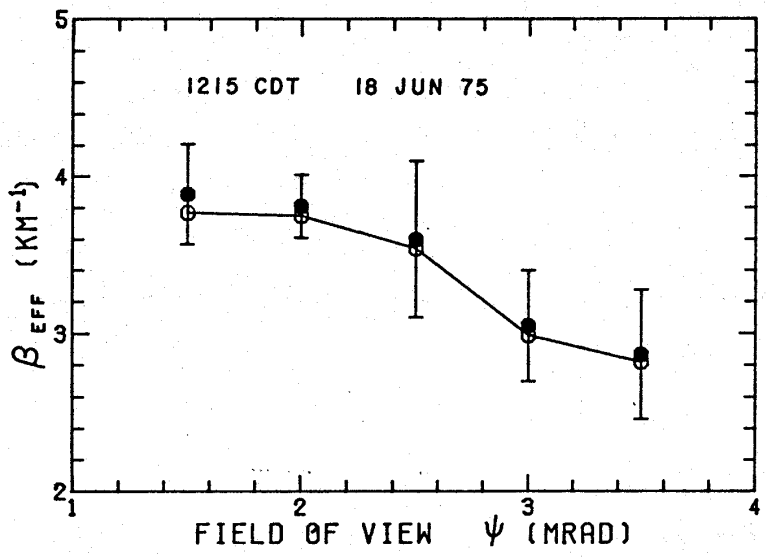

Fig. 5.1 The effective extinction coefficient, plotted as a function of receiver field of view during post thunderstorm drizzle on 18 JUN 75. The slope method was applied to 30 lidar return profiles to compute the mean and standard deviation of β_{eff} (•) . The (o) represent β_{eff} values after corresponding measurements from the clear atmosphere were subtracted. The lidar returns were obtained at a repetition rate of 0.5 Hz, and the receiver field of view was repetitively scanned from 1.5 to 3.5 mrad to minimize any effect due to changes in atmospheric structure or composition.

respectively, under suitable atmospheric conditions. The 25% change in the β_{eff} measurements of Fig. 5.1 reflects this functional dependence of $F(\tau)$ on ψ . In addition, no change in β_{eff} was observed in the measurements taken during the heavy rainfall or fog which occurred immediately before and after the sample time period of Fig. 5.1. Since heavy rain and fog do not satisfy the Eq. 5.1 criterion for the observation of multiple scattering variations with respect to receiver field of view,

these measurements are consistent with the theory that β_{eff} variations are caused by drops with diameters on the order of 0.1 mm.

Since the multiple scattering correction factor is a function of penetration depth, it is more appropriate to characterize the effects of multiple scattering on attenuation by an effective optical depth τ_{eff} over the range domain $[R_1,R_2]$, such that $\beta_{eff} = \tau_{eff}/(R_2-R_1)$. The variation of effective optical depth with the receiver field of view ψ can be obtained from the ratio of lidar signals which are simultaneously measured at ψ_1 and ψ_2. Using Eq. 4.17a, it follows that the change $\delta\tau_{eff}$ in τ_{eff} is given by

$$\delta\tau_{eff} = \frac{1}{2}\left\{\ell n \frac{P(R_2,\psi_2)}{P(R_2,\psi_1)} - \ell n \frac{P(R_1,\psi_2)}{P(R_1,\psi_1)}\right.$$

$$= \int_{R_1}^{R_2} \beta[F(\tau,\psi_2)-F(\tau,\psi_1)]dR \qquad (5.2)$$

The change in τ_{eff} was measured with ψ_1 = 1.5 mrad and ψ_2 = 5 mrad over a range interval from 1.7 to 2.7 km. Measurements of $\delta\tau_{eff}$ during stratiform rain on 19 September, 1976 are shown as a function of local time in Fig. 5.2. Simultaneous rain gage measurements of the rainfall rate R (mm/hr) are included in Fig. 5.2 for comparison. This figure shows that the maxima in $\delta\tau_{eff}$ at 1600 and 1645 CDT occur approximately 15 min after the corresponding maxima in the surface rainfall rate. This

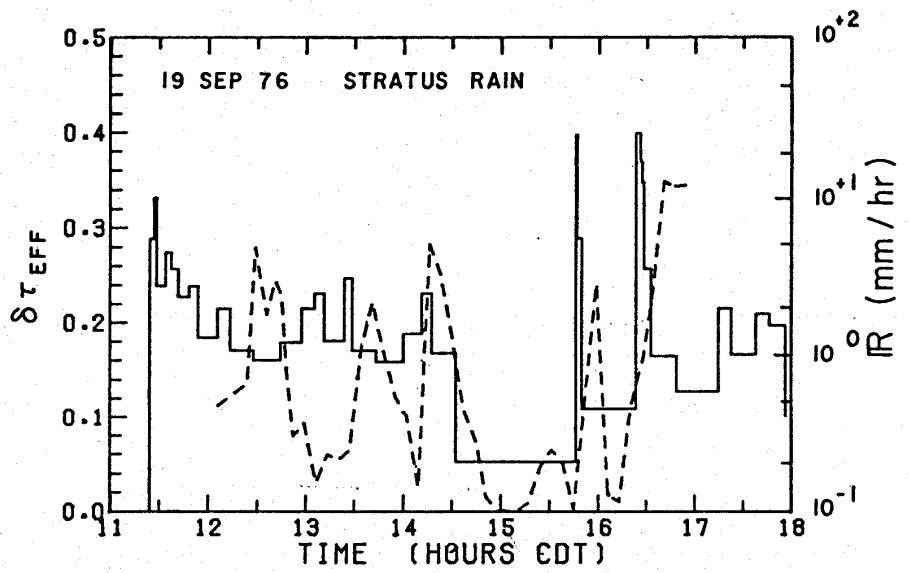

Fig. 5.2 Measurements of $\delta\tau_{eff}$ (dash) obtained from stratiform rain on 19 SEP 76 with $\psi_1 = 1.5$ mrad and $\psi_2 = 5$ mrad, plotted as a function of local time. Simultaneous measurements of the rainfall rate (solid, histogram) were obtained by a tipping bucket rain gage located 50 m below the lidar sample volume at a range of 2.7 km. The time delays of the $\delta\tau_{eff}$ maxima after the corresponding maxima in R are consistent with the presence of drops with diameters on the order of 0.1 mm.

time delay suggests that the $\delta\tau_{eff}$ maxima arise from the passage of small drops which accompany periods of heavy rain. The terminal velocity of a 0.1 mm diameter drop is approximately 20 cm s^{-1} and the cloud base was located at a height ~1 km. Assuming that drops of all sizes exit the cloud base at the same time, the time delays ~ 15 min are then consistent with the theory that the $\delta\tau_{eff}$ maxima arise from the presence of drops with

diameters ~ 0.1 mm .

A more controlled experiment was undertaken on 24 October, 1977 to determine the relation of $\delta\tau_{eff}$ to drop size. In addition to the simultaneous measurement of surface rainfall rate by a tipping bucket rain gage, the drop size distribution was obtained by the filter paper sampling technique. The filter paper collection procedure is summarized by Mason (1971, App. B) and Best (1950). The UW lidar was operated in the same manner used to obtain the data of Fig. 5.2, except that the lidar sample volume was located only 25 m above the gage and filter paper sample site. The resulting measurements of $\delta\tau_{eff}$ are shown in Fig. 5.3.

The drop size distribution was obtained using methylene blue powder on 24 cm diameter blanks of Whatman No. 1 filter paper. Two samples of the filter paper records at 0946 and 1107 CDT are shown in Fig. 5.4. When the stain size calibration of Marshall et al. (1947) for Whatman No. 1 filter paper is used, the drop diameter is related to the stain spot diameter by

$$D = 0.44\, D_{stain}^{2/3} \qquad (5.3)$$

The stain diameters were recorded in 0.5 mm intervals for $D_{stain} \leq 4$ mm , and in 1.0 mm intervals for $D_{stain} > 4$ mm . Measurements of stain sizes less than

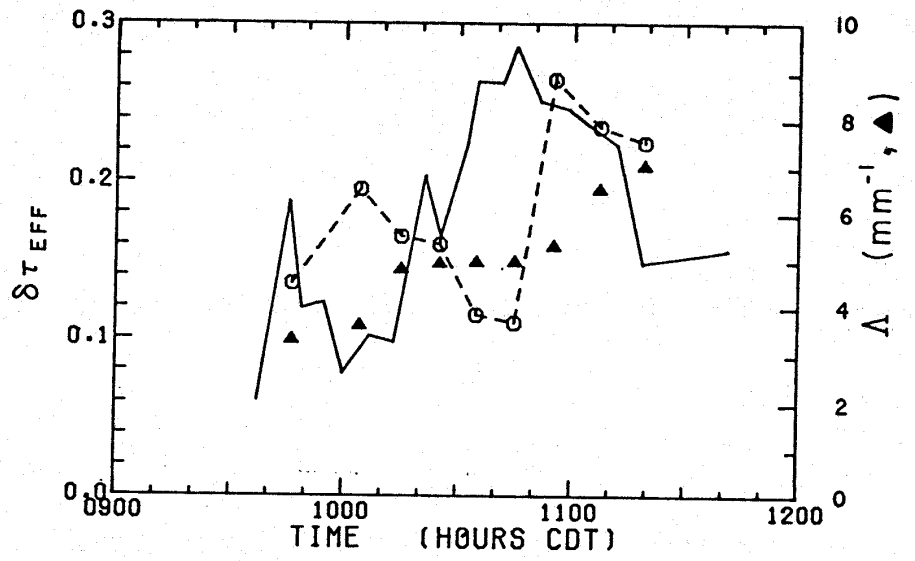

Fig. 5.3 Measurements of $\delta\tau_{eff}$ (solid) obtained from a light rain shower on 24 OCT 77 with $\psi_1 = 1.5$ mrad, $\psi_2 = 5$ mrad and $0 \leq R \leq 2.7$ km, plotted as a function of local time. Filter paper samples of the drop size distribution were used with the multiple scattering theory of chapters 3 and 4 to calculate $\delta\tau_{eff}$ (dash) by means of Eq. 5.2. The phase lag of these theoretical estimates is due to the spatial separation of the volumes sampled by the filter papers and the lidar. These results demonstrate the relation of the maximum in $\delta\tau_{eff}$ to the presence of drops with diameters on the order of 0.1 mm.

0.5 mm ($D < 0.3$ mm) by this technique are not reliable, and an estimation of the number of drops with diameters less than 0.3 mm was performed by fitting the filter paper data for $D > 0.3$ mm to the size distribution of Marshall and Palmer. The drop size distribution samples obtained at 0946, 1025 and 1107 CDT on 24 October, 1977 are shown in Fig. 5.5. The measured drop size distributions were

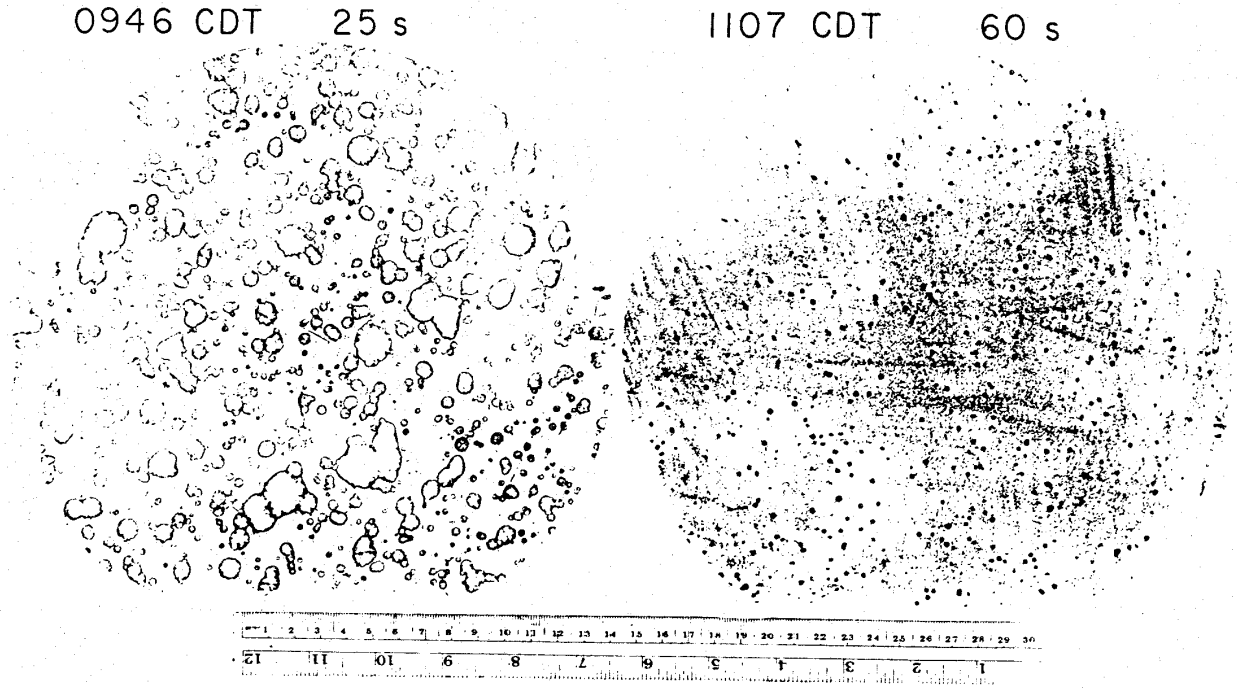

Fig. 5.4 Filter paper samples of the drop size distribution at 0946 (left) and 1107 (right) CDT during light rain on 24 OCT 77. These stains were obtained using methylene blue powder on 24 cm diameter blanks of Whatman No. 1 filter paper.

used to estimate the shape factor Λ of the M-P size distribution (cf. Eq. 2.10). The M-P size distributions corresponding to the drop samples at 0946, 1025 and 1107 CDT are included in Fig. 5.5 for comparison to the measured distributions of drop size. The Λ values which were obtained from the entire set of filter paper samples on 24 October, 1977 are included in Fig. 5.3.

The filter paper samples of the drop size distributions were used with the multiple scattering theory of chapters 3 and 4 to calculate $\delta\tau_{eff}$ by means of Eq. 5.2, and these theoretical results are included in Fig. 5.3. The theoretical estimates and lidar measurements of $\delta\tau_{eff}$ agree in magnitude, but they are not in phase in time. The lidar measurement of $\delta\tau_{eff}$ was obtained over the range interval $0 \leq R \leq 2.7$ km with the lidar pointing horizontally to the WSW. The drop samples, on the other hand, were obtained under the lidar beam propagation path at a range of 2.7 km. The mean wind during this experiment was South Easterly at ~11 knots. The rainfall rate was simultaneously measured by tipping bucket rain gages located under the beam propagation path at ranges of 0 and 2.7 km, and the initiation of rainfall was detected at 0938 CDT at 0 km range, and at 0954 CDT at 2.7 km range. The temporal discrepancy of the measured and theoretical values of $\delta\tau_{eff}$ of Fig. 5.3 can therefore be explained

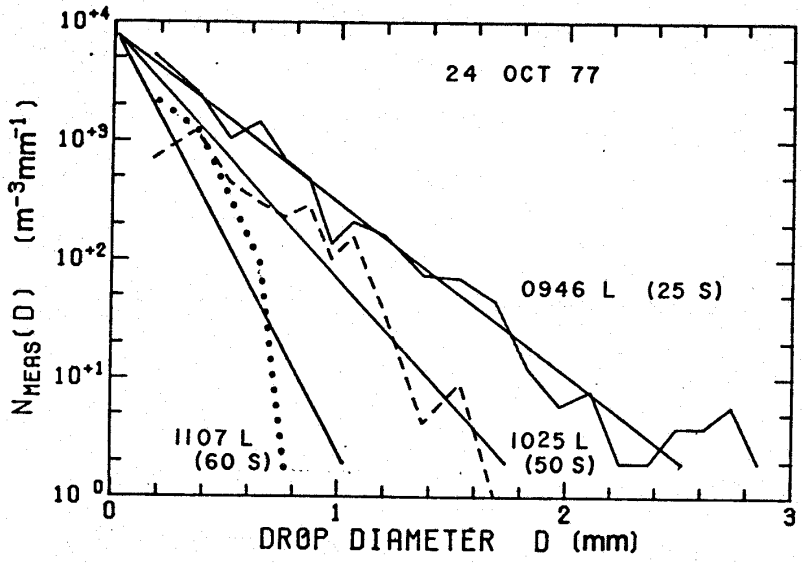

Fig. 5.5 Measurements of the drop size distribution obtained from filter paper samples at 0946 (solid), 1025 (dash) and 1107 (dot) CDT in light rain on 24 OCT 77. The M-P size distribution fits to these samples are included for comparison. When compared to Fig. 5.3, these samples demonstrate the relation of the maximum in $\delta\tau_{eff}$ to the presence of drops with diameters on the order of 0.1 mm.

by the differences in sample volume locations.

The data of Figs. 5.3 through 5.5 demonstrate the relation of maxima in $\delta\tau_{eff}$ to the presence of drops with diameters on the order of 0.1 mm. This observed variation in the contribution of multiple scattering to lidar signals from rain is consistent with the multiple scattering theory which is presented in chapters 3 and 4. The $\delta\tau_{eff}$ measurements indicate that the large receiver field of view approximations will hold for lidar operation

in moderate to heavy rainfall. These results also indicate that the small receiver field of view limits will apply when the UW lidar is operated in cloud or fog.

5.2 Solutions to the Lidar Equation

The lidar equation is solved in this section for the optical extinction coefficient in an atmosphere which is composed of two non-absorbing scattering components with extinction coefficients β_o and β_r. The extinction coefficient β_o is assumed to arise from a spatially homogeneous or independently measured spatial distribution of background aerosol, light drizzle, haze or fog, and the component β_r is used to represent the spatially inhomogeneous extinction coefficient of rainfall. The effective extinction coefficient of the atmosphere during rainfall events is then

$$\beta_{eff}(R) = [1-F_r(R,\psi)]\beta_r(R)+[1-F_o]\beta_o \qquad (5.4)$$

The backscatter phase function for each component is assumed to be either known a priori or independently measured. Taking the natural logarithm of the lidar equation (Eq. 1.2), the two component lidar equation for rain is

$$\ell n(PR^2) = \text{const} + \ell n[\beta_r^{1+k_2} + \frac{\mathbb{P}_o(\pi)}{k_1}\beta_o] - 2\int_0^R \{[1-F_r(R',\psi)]\beta_r(R') + [1-F_o]\beta_o\}dR' \qquad (5.5)$$

where k_1 and k_2 are related to $\mathbb{P}_r(\pi)$ by Eq. 2.24, viz.

$$\mathbb{P}_r(\pi) = k_1\beta_r^{k_2} \qquad (2.24)$$

For convenience in notation, the symbol Ξ is used to represent a modified volume backscattering coefficient, such that

$$\Xi(R) = \beta_r(R)^{1+k_2} + \frac{\mathbb{P}_o(\pi)}{k_1}\beta_o \qquad (5.6)$$

When β_r, β_o and therefore $\mathbb{P}_r(\pi)$, $\mathbb{P}_o(\pi)$ are independent of range, then the effective extinction coefficient can be directly measured from the "slope" of Eq. 5.5, viz.

$$\beta_{eff} = -\frac{1}{2}\frac{d}{dR}\ell n(PR^2) \qquad (5.7)$$

An examination of lidar returns from rainfall suggests that Ξ is often constant over ranges on the order of several kilometers. This slope method has been used frequently in the study of optical extinction, cf. Viezee et al. (1973), Shipley et al. (1974).

5.2a The Bernoulli Solution

An analytic solution to the radar equation which applies to the lidar problem has been known for many years, cf. Hitschfeld and Bordan (1954). This radar equation solution can be readily modified for application to the measurement of the optical extinction coefficient by lidar, and it has been cited often in the lidar literature, cf. Barrett and Ben-Dov (1967), Viezee et al. (1969), Fernald et al. (1972). This solution is derived again for the case of rain in this section.

An exact solution to Eq. 5.5 for β_r is not available, and the range profile of β_r must therefore be obtained numerically. An analytic solution to Eq. 5.5 does exist, however, when the modified volume backscattering coefficient of Eq. 5.6 is approximated by

$$\Xi'(R) = \{\beta_r(R)+[\frac{P_o(\pi)}{k_1}\beta_o]^{\frac{1}{1+k_2}}\}^{1+k_2} \qquad (5.8a)$$

The Eq. 5.8a approximation is an underestimate of $\Xi(R)$ with the maximum fractional error occurring when

$$\frac{\partial}{\partial\beta_r}\frac{\Xi'(R)}{\Xi(R)} = 0 \qquad (5.8b)$$

or

$$\beta_r(R)^{1+k_2} = \frac{P_o(\pi)}{k_1}\beta_o \qquad (5.8c)$$

The maximum fractional error incurred by the Eq. 5.8a

approximation is therefore

$$\left.\frac{\Xi'(R)}{\Xi(R)}\right|_{MAX} - 1 = 2^{k_2} - 1 \qquad (5.8d)$$

Referring to Eq. 2.26b for the "instantaneous" backscatter phase function of rainfall, it is expected that $k_2 \sim -0.025$ such that

$$\left|\frac{\Xi'(R)}{\Xi(R)} - 1\right| \lesssim 0.017 \qquad (5.8e)$$

Substituting the Eq. 5.8a approximation for the modified volume backscattering coefficient of rain, Eq. 5.5 can be rewritten

$$\frac{d\Xi'}{dR} = \frac{2(1-F_r)}{1+k_2} \cdot \Xi'^2 + \Xi' \cdot \frac{dH(R)}{dR} \qquad (5.9a)$$

where

$$H(R) = \frac{\ell n(PR^2)}{1+k_2} + \frac{2}{1+k_2}\int\left\{(1-F_o)\beta_o - (1-F_r)\cdot\left[\frac{P_o(\pi)}{k_1}\beta_o\right]^{\frac{1}{1+k_2}}\right\}dR \qquad (5.9b)$$

Eq. 5.9a is a first order nonlinear differential equation in $\Xi'(R)$, and the general solution to this ordinary differential equation is known as the "Bernoulli solution."[1]

---

[1] According to Murphy (1960), the differential equation

$$y' = g(x)\, y^{\alpha} + f(x)\, y$$

has the solution

$$y^{\alpha-1} = \frac{\exp[h(x)]}{C(x_o) - (\alpha-1)\int_{x_o}^{x} g(x)\exp[h(x)]dx}$$

The Bernoulli solution for the modified volume backscatter coefficient of rainfall is then

$$\Xi'(R) = \frac{\exp[H(R)-H(R_o)]}{\frac{1}{\Xi'(R_o)} - \frac{2}{1+k_2}\int_{R_o}^{R}[1-F_r(R')]\exp[H(R')-H(R_o)]dR'} \qquad (5.10)$$

where $H(R)$ and $\Xi'(R)$ are defined by Eqs. 5.9b and 5.8a, respectively.

The Eq. 5.10 solution requires an independent measurement of $\Xi'(R_o)$ in order to calibrate the entire solution profile. Since the multiple scattering correction factor for rain is a function of optical penetration depth (cf. Eqs. 4.19), an estimate of the optical depth from the lidar to the calibration range R_o is also required. Hitschfeld and Bordan (1954) examined the accuracy of the "Bernoulli" solution for the determination of rainfall rates from radar signals at attenuating radio wavelengths. It was shown that relatively small uncertainties in the value of the integration constant would result in large solution errors. An <u>in situ</u> point measurement of the optical extinction coefficient or a measurement of an integrated path optical depth in the lidar sample volume is therefore needed to calibrate the lidar solutions.

---

where

$$h(x) = (\alpha-1)\int_{x_o}^{x} f(x)dx$$

5.2b An Algorithm for Solution Calibration in the Absence of an Independent Calibrating Measurement

Approximate methods for estimating the integration constant $\Xi'(R_o)$ of Eq. 5.10 are useful when qualitative depictions of the spatial distribution of the optical extinction coefficient are desired and an independent solution calibration measurement is unavailable. When accurate quantiative estimates of the spatial distribution of β_r are needed, then an additional measurement of either the integrated optical depth along the lidar line of sight or the values of β_r, β_o and the ratio $\mathbb{P}_o(\pi)/\mathbb{P}_r(\pi)$ at some calibration range R_o is required. The solutions which are calibrated by an independent measurement will also be somewhat unreliable due to the uncertainties in both the backscatter phase function and the detailed effects of multiple scattering. In particular, the results of chapters 2, 3 and 4 suggest that the backscatter.phase function and the multiple scattering correction factor may themselves be unknown to approximately $\pm 20\%$. A measurement of the spatial distribution of β_r to accuracies on the order of $\pm 20\%$ is still useful, however. The applications of this information were discussed in section 1.1.

An approximate calibration procedure for obtaining

the integration constant of Eq. 5.10 was proposed by Shipley et al. (1974). This procedure selected the "smoothest" profile by minimizing the second derivative of the solution with respect to range, but this procedure has since been proven to be unreliable. A more reliable solution calibration procedure is presented in this section. This calibration procedure uses the "slope" solution of Eq. 5.7 on all range segments of the return signal which are linear in range, and it assumes that they arise from regions which are locally spatially homogeneous, i.e. $\frac{d^3}{dR^3} \ell nPR^2 = 0$ for $R_1 \leq R \leq R_2$. The slopes of all linear segments from several signal profiles which are adjacent in both space and time are then used to determine those β_r solution profiles which best match the assumption of local spatial homogeneity. It is <u>not</u> likely that most of the linear signal segments will correspond to spatially homogeneous distributions of β_r . It is assumed that the entire set of slopes will be randomly distributed about the true value of β_r , however, provided that the sample size is sufficiently large. The occurrence of a large number of linear segments in several return signal profiles is therefore required before this calibration procedure can be attempted.

The segment slope calibration procedure can be outlined as follows:

1. Determine the slope of all linear segments.

This step seeks linear segments in the lidar signal $\ell n(PR^2)$ and assumes that they arise from a spatially homogeneous distribution of β_r. Spatial homogeneity will not hold for all such samples of linear segments, but the slope estimates of β_{eff} are assumed to be randomly distributed about the true values. A return signal segment is accepted as linear when its linear correlation coefficient is greater than some predetermined decision value. A linear correlation coefficient threshold of 0.70 is used in this paper.

2. Determine the integration constants which explain segment linearity.

This step provides a probable estimate to the value of $\Xi'(R_o)$ for each signal profile having one or more linear segments. A simple or range weighted average of these estimates is taken when more than one linear segment is found. Eqs. 4.19 are used to estimate the range variation of the multiple scattering correction factor.

3. Match the adjacent and succeeding profiles with respect to total optical depth.

Since the spatial distribution of the optical extinction coefficient in rain is highly variable, a meaningful comparison of the solution profiles cannot be performed by matching the solution values point by point with one

another. The total optical depth over large range intervals is much less variable, however, particularly when the lidar samples are separated by time and space scales which are small in comparison to the scale of structure of the scattering medium. Rainfall displays time and space structure which persists over time periods $\sim 10^2$ s and lengths $\sim 10^2$ m (cf. section 5.1). The $\Xi'(R_o)$ values for adjacent profiles are therefore adjusted to yield consistent values of $\int_{R_{min}}^{R_{max}} \beta_r(R)\, dR$ to within some predetermined decision value.

This approximate calibration procedure was applied to 1900 consecutive lidar returns obtained from stratus rain on 19 September, 1976. These lidar profiles were obtained at a repitition rate of 0.5 Hz in the RTI format. In addition, the lidar system was accurately pointed towards a 7.5 cm diameter reflector target mounted on a tower at a range of 2.7 km to directly measure the two way total optical depth. A very large signal was obtained from this target under clear atmospheric conditions, and the target signal was therefore reduced to a measureable intensity by the introduction of neutral density filters to the receiver optical path on alternate laser firings. The target was also mounted in a protective shroud to

prevent any change in reflectivity due to wetting by rain.

The measurement of the target reflection signal "spike" is complicated by the 10 MHz frequency response of the receiver electronics and the spatial variability of the transmitted laser beam. The target reflection signal was examined on a clear day under stable atmospheric conditions to obtain the transfer curve of target signal intensity to recorded voltage, where the input signal intensity was varied by the introduction of neutral density filters to the receiver optical path. The entire set of target reflection measurements indicates that the target signal can be characterized by a standard deviation on the order of $\pm 10\%$. An average value of the target signal which is formed from N measurements will decrease the measurement uncertainty by a factor of $N^{1/2}$. Rainy atmospheres are characterized by rapid fluctuations in optical depth, on the other hand, and the number of measurements included in such averages should be small to avoid errors caused by rapid variations in the optical depth between the lidar and the calibration target. The target signal measurements which are described in this section were obtained using a running mean averaging procedure with $N = 2$.

A comparison of the target measurements of the average extinction coefficient to the results of the segment

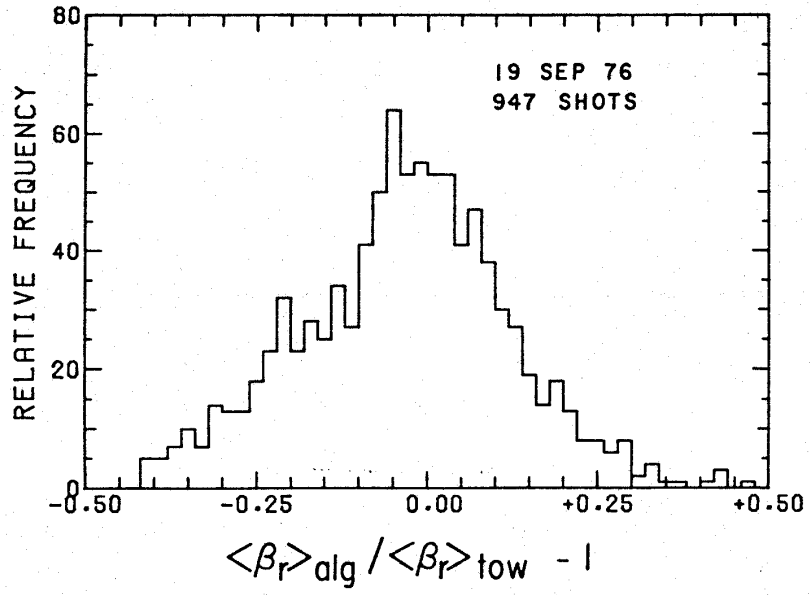

Fig. 5.6 A comparison of the target measurements of the average extinction coefficient to the results of the segment slope calibration procedure for rainfall at Madison on 19 Sep 76. This relative frequency distribution shows agreement of these results to within a one standard deviation of ±20%

slope calibration procedure is shown in Fig. 5.6 for the data of 19 September, 1976. These results were obtained using Eqs. 4.19 to approximate the multiple scattering correction factor, and Eq. 2.24 to describe the relation of $\mathbb{P}_r(\pi)$ to β_r with $k_2 = -0.025$. The phase function ratio $\mathbb{P}_o(\pi)/\mathbb{P}_r(\pi)$ and the background extinction coefficient were estimated to be 0.4 and 0.7 km^{-1}, respectively. Linear segments were accepted in step 1 of the calibration procedure when profile lengths of 450 m had linear

correlation coefficients greater than 0.70. In addition, the optical depth contribution in the regions where lidar signals were not available was estimated by extrapolating the mean solution value $\langle \beta_r \rangle_{alg}$. Useable signals were not obtained at ranges less than 0.9 km due to the lateral separation of the transmitter and receiver optic axes. In addition, useable signals were not obtained from regions near the target when the signal was less than or comparable to the noise due to the large degree of optical attenuation. The relative frequency distribution of Fig. 5.6 shows agreement between the tower measurements and the calibration procedure to within one standard deviation of $\pm$20%. The distribution of the fractional error of algorithm estimates and target measurements of the average optical extinction coefficient is shown in Fig. 5.7. These results show that the linear segment calibration procedure correctly estimates the average value of the optical extinction coefficient during rainfall.

5.3 RHI Depictions of the Optical Extinction Coefficient in a Thunderstorm

An RHI time sequence of lidar returns from the leading edge of a thunderstorm on 11 July, 1975 at Madison is shown in Figs. 5.8. This data was obtained by the

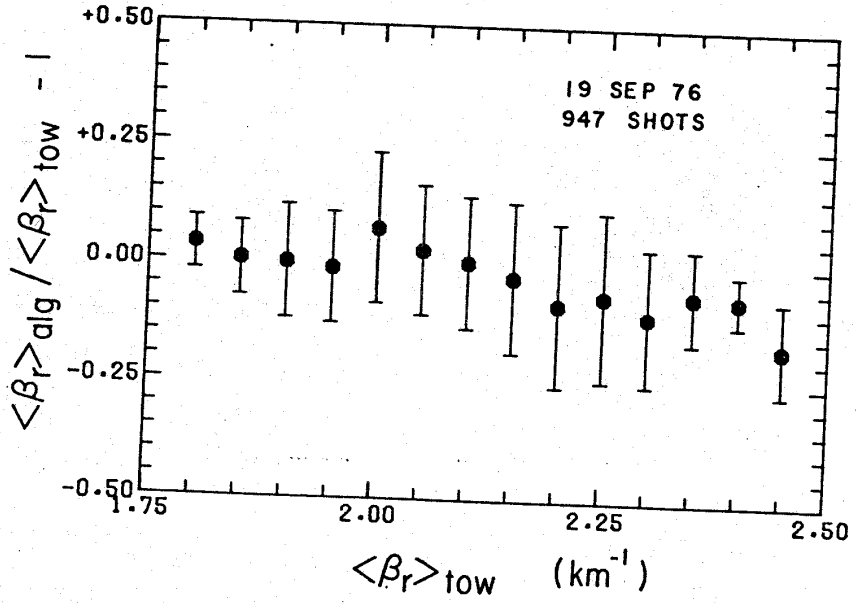

Fig. 5.7 The distribution of calibration procedure error in average extinction coefficient when compared to the target measurements of total optical depth (dots). This procedure error is shown as a function of the target measurement of the average optical extinction coeffficient. The vertical intervals represent the standard deviation of this calibration procedure error. The results of this figure and Fig. 5.6 show that the linear segment calibration algorithm correctly predicts the average value of the optical extinction coefficient during rainfall. The slight downward trend of the calibration procedure error with increasing $\langle\beta_r\rangle_{tow}$ may be due to the approximation of the multiple scattering correction factor by Eqs. 4.19.

UW lidar using an elevation scan from 3.0° to 25.0° in steps of 0.5° at a repetition rate of 1 Hz. The UW lidar was pointed into the direction of the mean wind. A tipping bucket rain gage with an accumulation resolution of 0.25 mm was located under the lidar beam propagation path at a range of 2.7 km. These RHI scans were obtained in 45 s

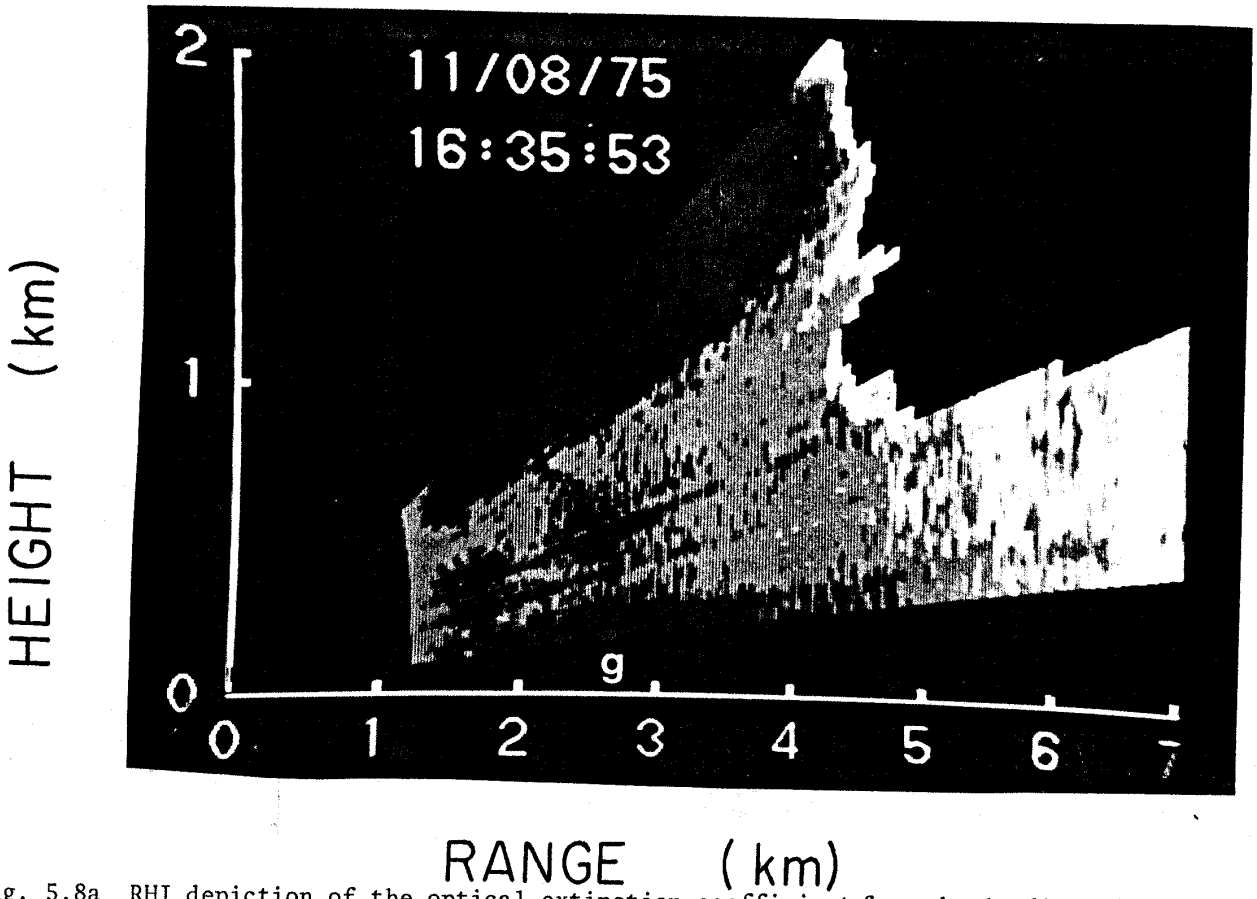

Fig. 5.8a RHI depiction of the optical extinction coefficient from the leading edge of a thunderstorm at 1635,53 CDT on 11 JUL 75 at Madison, Wisconsin. A tipping bucket rain gage "g" was located on the surface at a range of 2.7 km. These pictures were obtained from lidar signals using the linear segment calibration procedure described in section 5.2b. The RHI cross section was then reconstructed using the McIDAS system.

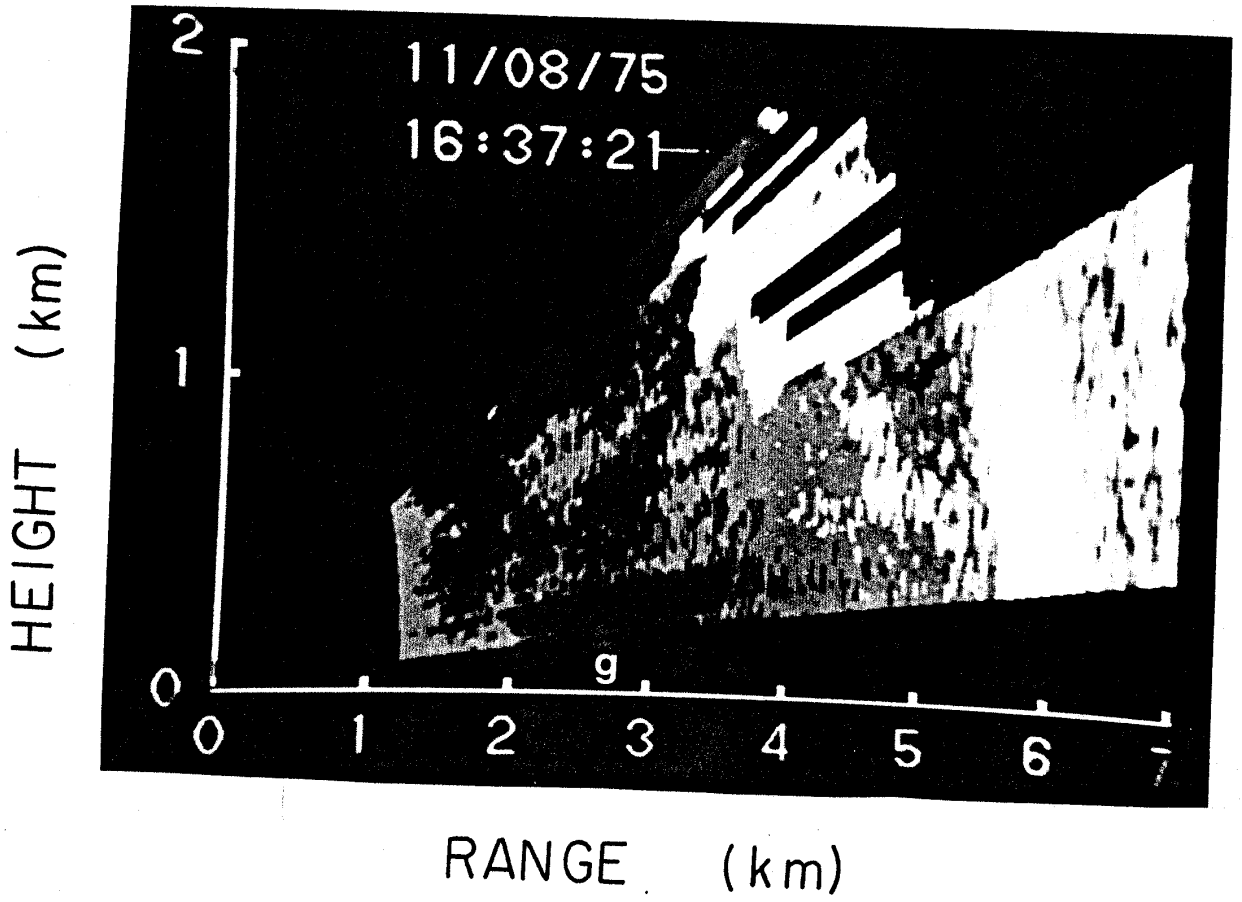

Fig. 5.8b RHI scan at 1637,21 CDT on 11 JUL 75 at Madison, Wisconsin. The "roll cloud" at 3 km range, 1 km height is moving from the NW at approximately 18 m s^{-1} (40 mph).

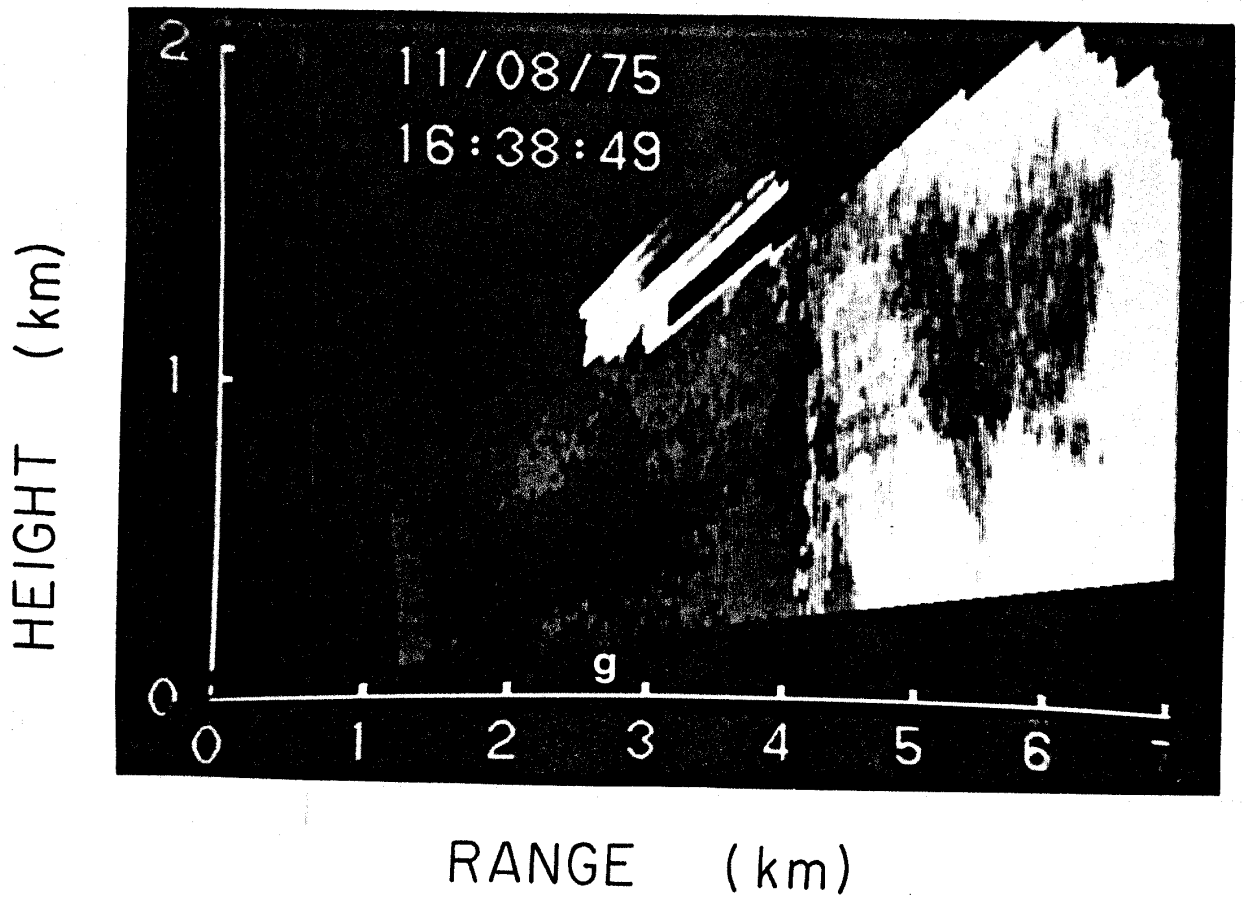

Fig. 5.8c RHI scan at 1638,49 CDT on 11 JUL 75 at Madison, Wisconsin.

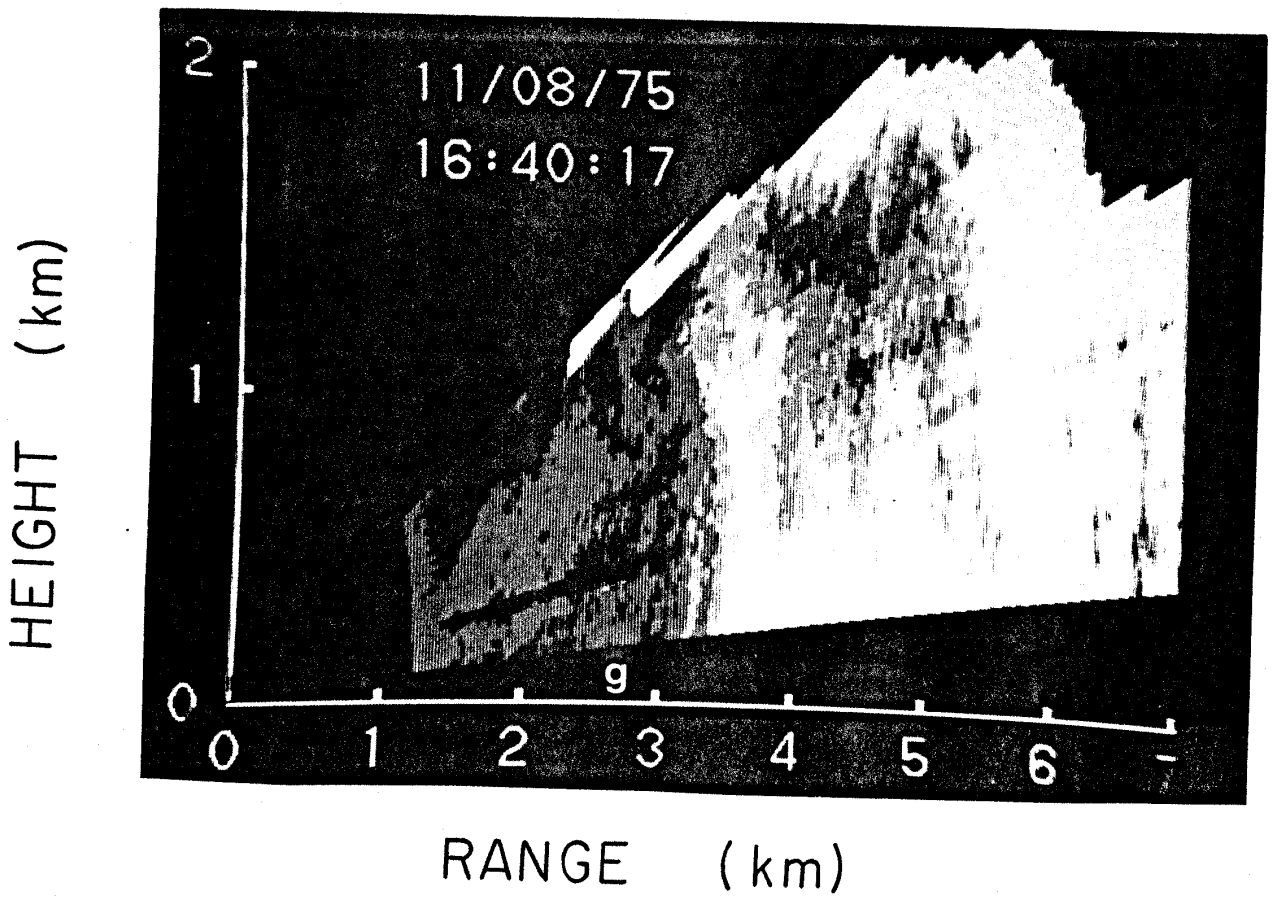

Fig. 5.8d RHI scan at 1640,17 CDT on 11 JUL 75 at Madison, Wisconsin. The tipping bucket rain gage "g" at 2.7 km range detected the initiation of rainfall at the surface at 1641 CDT.

as the elevation angle was decreased from 25 to 3 degrees, and it must be borne in mind that the rapid motion of rainfall features has resulted in a considerable distortion of the spatial distribution. The local time of each scan is given for the last lidar sample at 3.0° elevation.

The RHI depictions of the optical extinction coefficient in Figs. 5.8 were obtained using the linear segment calibration procedure of section 5.2b, where the multiple scattering correction procedure was approximated by Eqs. 4.19. A contour map of the vertical distribution of β_r (km^{-1}) for the data of Fig. 5.8d is given in Fig. 5.8e. It is evident from Figs. 5.8 that precipitation can be tracked by lidar as it falls from cloud base to the surface. For example, the tipping bucket rain gage ("g" in Figs. 5.8) detected the initiation of rainfall at 1641 CDT with an average rainfall rate ~ 5 mm hr^{-1} at 1643 CDT. This rainfall rate measurement is consistent with the rainfall optical extinction coefficient $\beta_r \sim 0.5$ km^{-1} which was observed by the lidar above the gage (cf. Eq. 1.1). These results demonstrate the capability for lidar to measure the optical extinction coefficient of rainfall in the subcloud environment over ranges ~ 10 km . These results also show that lidar is capable of providing rainfall information with a spatial resolution ~ 10 m . Lidar therefore provides rainfall

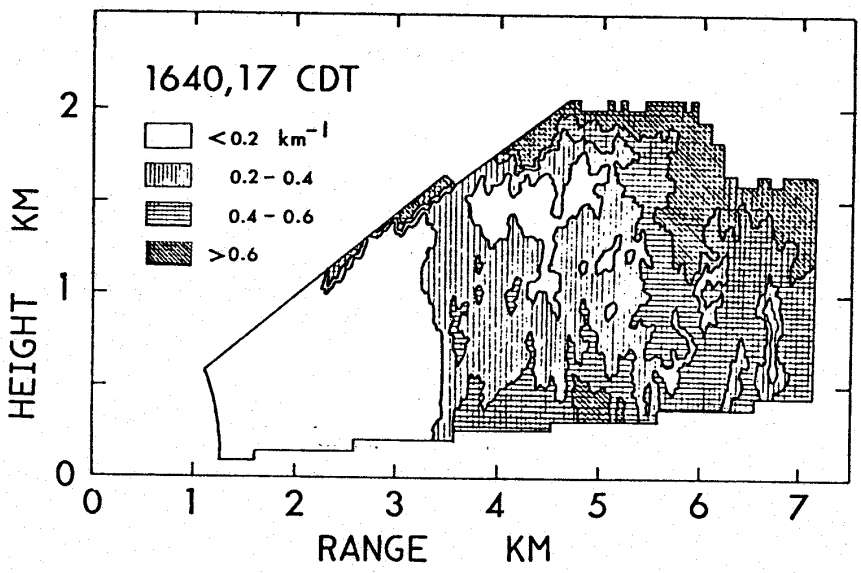

Fig. 5.8e Contour plot of the optical extinction coefficient for the RHI scan of Fig. 5.8d. Contours are plotted for optical extinction coefficient values which are integer multiples of 0.20 km^{-1}. The value of $\beta_r \sim 0.5$ km^{-1} "above" the rain gage at 2.7 km range is consistent with the gage measurement of the rainfall rate ~ 5 mm hr^{-1} at 1643 CDT.

information which can be used to complement that derived from radar and rain gages.

5.4 Summary

This study demonstrates the utility of lidar for the study of rainfall in the subcloud environment. The optical extinction coefficient of rain β_r (km^{-1}) is directly related to the rainfall rate by Eq. 1.1. As

was shown by Atlas and Ulbrich (1974), the radar reflectivity factor Z ($mm^6 m^{-3}$) and the optical extinction coefficient of rain are independent estimates of the drop size distribution of rainfall. The simultaneous measurement of both Z and β_r will therefore provide more information about rainfall than when radar is used alone or with rain gages.

The scattering properties of large dielectric spheres relevant to the lidar problem were examined in chapter 2. It was shown that the forward scatter and backscatter phase functions of a Marshall-Palmer size distribution of spherical water drops can be modeled by a simple sum of Gaussian functions, cf. section 2.5. When the drop size distribution is modeled after the "instantaneous" measurements of Joss and Gori (1978), then the value of the backscatter phase function at π radians is effectively independent of the rainfall rate or the optical extinction coefficient. The mean square angles for forward scattering and backscattering are inversely proportional to the characteristic drop size D_{max} (cf. Eq. 2.15a), and their ratio $Q = \langle\theta_f^2\rangle/\langle\theta_b^2\rangle$ is relatively independent of the detailed structure of the drop size distribution.

A general Neumann solution for the contribution of N^{th} order scattering to the return signal of a monostatic

lidar was derived in chapter 3. This solution assumes that multiple large angle scattering is negligible. It was shown that the return power ratio of N^{th} order scattering to single scattering can be expressed by a simple power law relationship to the optical penetration depth, namely

$$\boxed{\frac{P_N}{P_1} = 2^{N-1}\langle a\rangle^{N-1}\,\frac{\langle \mathbb{P}(\pi)\rangle_N}{\mathbb{P}(\pi)}\,A_N \cdot \frac{\tau^{N-1}}{(N-1)!}} \qquad (3.5)$$

where

$\langle a\rangle$ mean value of the fraction of total scattered energy which is defined by the forward scattering phase function, where the average is taken over penetration depth $0 \leq x \leq R\text{-}R_c$

$\frac{\langle \mathbb{P}(\pi)\rangle_N}{\mathbb{P}(\pi)}$ average value of the backscatter phase function

A_N dimensionless coefficient which describes the variation of multiple scattering with the dimensionless receiver field of view

τ optical depth between the location of the backscattering event and the lidar.

The multiple scattering coefficients A_N are defined by the ratio of N^{th} order scattering to single scattering signal contributions in the limit of isotropic backscattering $(\frac{\langle \mathbb{P}(\pi)\rangle_N}{\mathbb{P}(\pi)} = 1)$. The coefficients A_N are given as a function of a dimensionless receiver field of view in Figs. 3.2 and 3.3, and in Table 3.1. The value of

the average backscatter phase function was examined in chapter 4, and a comprehensive set of simple approximations for $\frac{\langle P(\pi)\rangle_N}{P(\pi)}$ was derived, cf. section 4.4. Finally, these results were used to derive a multiple scattering correction factor to the lidar equation for rain. It was shown that the effective attenuation is decreased by the presence of multiple scattering. It was also shown that the multiple scattering correction factor is a function of the optical penetration depth, the geometry of the lidar system, and the spatial distribution of the scattering medium.

Section 5.1 indicates that receiver field of view techniques which measure the angular variation of the multiple scattering contribution can be used to derive information on the size distribution of atmospheric particulates. In particular, the effective diameter $\langle D\rangle$ produces a measureable field of view difference signal when

$$\langle D\rangle \sim \frac{2}{\pi\sqrt{3}} \frac{\lambda}{\psi} \tag{5.10}$$

where λ is the transmitter wavelength and ψ is the half width receiver field of view. Lidars can currently employ transmitters with wavelengths from 280 nm (quadrupled Nd:YAG) to 10^4 nm (CO_2), and receiver fields

of view from 10^{-6} to 10^{-1} rad. It is therefore possible for lidar instrumentation to obtain atmospheric particle size information over a wide range of particle sizes, provided that enough particles are present in the size range of interest to produce a measureable contribution to the optical depth.

Lidar returns from rainfall can be used to derive the spatial distribution of the optical extinction coefficient using Eq. 5.10 only when an independent estimate of β_r is provided at some calibration range along the lidar beam propagation path. An algorithm which provides this calibration in the absence of such an independent measurement was presented in section 5.2b, and it was applied to several lidar RHI scans from the leading edge of a thunderstorm to derive the spatial distribution of β_r, cf. section 5.3. The RHI pictures of Figs. 5.8 demonstrate the ability of lidar to track precipitation as it falls from cloud base to rain gages located on the surface. It can be concluded that the spatial distribution of the optical extinction coefficient can be measured by lidar over extended ranges (several km) with high spatial resolution (several m). Such information can be used to depict the distribution of precipitation in the sample volumes which are used by radar and rain gages.

BIBLIOGRAPHY

Atlas, D. (1953) "Optical Extinction by Rainfall", J Meteor, 10, pp 486-488.

Atlas, D. and Ulbrich, W. (1974) "The Physical Basis for Attenuation-Rainfall Relationships and the Measurement of Rainfall by Combined Attenuation and Radar Methods", J de Recherches Atmos, 8, pp 275-298.

Barrett, E. W. and Ben-Dov, O. (1967) "Application of Lidar to Air Pollution Measurements", J Appl Meteor, 6, pp 500-515.

Battan, L. J. (1976) "Vertical Air Motions and the Z-R Relation", J Appl Meteor, 15, pp 1120-1121.

Best, A. C. (1950) "The Size Distribution of Raindrops", Quart J Roy Meteor Soc, 76, pp 16-36.

Bryant, H. C. and Cox, A. J. (1966) "Mie Theory and the Glory", J Opt Soc Amer, 56, pp 1529-1532.

Chu, T. S. and Hogg, D. C. (1968) "Effects of Precipitation on Propagation at 0.63, 3.5, and 10.6 Microns", Bell Sys Tech J, 47, pp 723-759.

Curcio, J. A. and Knestrick, G. L. (1958) "Correlation of Atmospheric Transmission with Backscattering", J Opt Soc Amer, 48, pp 686-689.

Dave, J. V. (1968) "Subroutines for Computing the Parameters of the Electromagnetic Radiation Scattered by a Sphere", IBM Sci Ctr Rep No. 320-3237, 65 pp.

Deirmendjian, D. (1969) Electromagnetic Scattering on Spherical Polydispersions, Amer Elsevier, New York, 290 pp.

Derr, V. E., Abshire, N. L., Cupp, R. E. and McNice, G. T. (1976), "Depolarization of Lidar Returns from Virga and Source Cloud", J Appl Meteor, 15, pp 1200-1203.

Eloranta, E. W. (1972) "Calculation of Doubly Scattered Lidar Returns", Ph.D. Thesis, Univ Wisconsin, Madison, 115 pp.

Eloranta, E. W., (1978) personal communication, cf. Appendix A.

Fahlen, T. S. and Bryant, H. C. (1968) "Optical Back Scattering from Single Water Droplets", J Opt Soc Amer, 58, pp 304-310.

Fermi, E. (1950) Nuclear Physics, Univ Chicago Press, 248 pp.

Fernald, F. G., Herman, B. M. and Reagan, J. A. (1972) "Determination of Aerosol Height Distributions by Lidar", J Appl Meteor, 11, pp 482-489.

Hitschfeld, W. and Bordan, J. (1954) "Errors Inherent in the Radar Measurement of Rainfall at Attenuating Wavelengths", J Meteor, 11, pp 58-67.

Jones, D. M. A. (1959) "The Shape of Raindrops", J Meteor, 16, pp 504-510.

Joss, J. and Gori, E. G. (1978) "Shapes of Raindrop Size Distributions", J Appl Meteor, 17, pp 1054-1061.

Khare, V. and Nussenzveig, H. M. (1977) "Theory of the Glory", Phys Rev Lett, 38, pp 1279-1282.

Kunkel, K. E. and Weinman, J. A. (1976) "Monte Carlo Analysis of Multiply Scattered Lidar Returns", J Atmos Sci, 33, pp 1772-1781.

Marshall, J. S., Langille, R. C. and Palmer, W. M. (1947) "Measurement of Rainfall by Radar", J Meteor, 4, pp 186-192.

Marshall, J. S. and Palmer, W. M. (1948) "The Distribution of Raindrops with Size", J Meteor, 5, pp 165-166.

Mason, B. J. (1971) The Physics of Clouds, Oxford Univ Press, 671 pp.

Mueller, E. A. and Silha, E. J. (1978) "Unique Features of the CHILL Radar System", 18th Conf Radar Meteor, Atlanta, Ga., pp 381-382.

Murphy, G. M. (1960) Ordinary Differential Equations and their Solutions, D Van Nostrand Co, New York, 451 pp.

Nussenzveig, H. M. (1969) "High-Frequency Scattering by a Transparent Sphere, II. Theory of the Rainbow and the Glory", J Math Phys, 10, pp 125-176.

Plass, G. N. and Kattawar, G. W. (1971) "Reflection of Light Pulses from Clouds", Appl Opt, 10, pp 2304-2310.

Platt, C. M. R. (1973) "Lidar and Radiometric Observations of Cirrus Clouds", J Atmos Sci, 30, pp 1191-1204.

Puhakka, T. (1978) "On the Accuracy of Radar Point Measurements of Rainfall Intensity", 2nd Nordic IHP Meeting, Helsinki, 14 pp.

Sassen, K. (1977a) "Optical Backscattering from Near-Spherical Water, Ice, and Mixed Phase Drops", Appl Opt, 16, pp 1332-1341.

Sassen, K. (1977b) "Lidar Observations of High Plains Thunderstorm Precipitation", J Atmos Sci, 34, pp 1444-1457.

Shifrin, K. S. and Rabinovich, Ya. I. (1957) "The Spectral Indicatrices of Large Water Drops and the Spectral Polarization of Rainbows", Bull Acad Sci USSR, No. 12, pp 73-89.

Shipley, S. T., Eloranta, E. W. and Weinman, J. A. (1974) "Measurement of Rainfall Rates by Lidar", J Appl Meteor, 13, pp 800-807.

Shipley, S. T. and Weinman, J. A. (1978) "A Numerical Study of Scattering by Large Dielectric Spheres", J Opt Soc Amer, 68, pp 130-134.

Smith, E. (1975) "The McIDAS System", IEEE Trans Geosci Electron, GE-13, pp 123-136.

Titschmarsh, E. C. (1948) Introduction to the Theory of Fourier Integrals, Oxford Univ Press, 394 pp.

Van de Hulst, H. C. (1957) Light Scatterings by Small Particles, John Wiley and Sons, New York, 470 pp.

Viezee, W., Uthe, E. E. and Collis, R. T. H. (1969) "Lidar Observations of Airfield Approach Conditions: An Exploratory Study", J Appl Meteor, 8, pp 274-283.

Viezee, W., Oblanas, J. and Collis, R. T. H. (1973) "Evaluation of the Lidar Technique of Determining Slant Range Visibility for Aircraft Landing Applications", AFCRL-TR-73-0708, 132 pp.

Volz, F. (1961) "Der Regenbogen", Handbuch der Geophysik, 8, Borntraeger, 932 pp.

Weinman, J. A. (1976) "Effects of Multiple Scattering on Light Pulses Reflected by Turbid Atmospheres", J Atmos Sci, 33, pp 1763-1771.

Wilson, J. (1970) "Integration of Radar and Raingage Data for Improved Rainfall Measurement", J Appl Meteor, 9, pp 489-497.

Appendix A

A Ray Tracing Solution for the Contribution of N^{th} Order Scattering to the Return Signal of a Monostatic Lidar

by E. W. Eloranta, Edited by S. T. Shipley (1978)

This derivation considers all combinations of N-1 forward scatterings and one large angle scattering to calculate the return signal of a coaxial monostatic lidar due to N^{th} order scattering. It is assumed that N-1 scatterings are small angle forward scatterings which give rise to small angular deflections. It is also assumed that the lidar return signal is comprised of photons which have undergone only one large angle scattering. The forward scattering phase function is represented by a single Gaussian function, whereas the backscattering phase function is restricted to be isotropic in angle. The restriction of isotropic backscattering is not applied to the calculation of the double scattering contribution in section A.4.

The forward phase function is defined by

$$\frac{P_f(\Theta)}{4\pi} = \frac{a}{\pi\langle\Theta_f^2\rangle} \exp\left[-\frac{\Theta^2}{\langle\Theta_f^2\rangle}\right] \qquad (A.1)$$

where a is that fraction of the total scattered energy whcih is explained by the forward phase function and

$\langle\theta_f^2\rangle$ is the mean square angle for forward scattering. The scattering phase function and the total extinction cross section of the scattering medium are general functions of the penetration depth but they are not allowed to vary in directions normal to the axis of propagation. The initial energy distribution of the lidar transmitter is represented by a single Gaussian function in angle and by a Dirac delta function in time.

The return signal power $P_{n,m}$ due to N^{th} order scattering is determined for n forward scatterings prior to the large angle scattering event, followed by m forward scatterings on the return path, such that

$$N = n + m + 1 \qquad (A.2)$$

The energy distribution in a backscattering plane at range R from the lidar due to n small angle forward scatterings is obtained as a function of the radial distance from the lidar axis of propagation. The angular structure of this energy distribution is not retained since the forward directed energy is scattered isotropically at range R to simulate the large angle scattering. The energy emenating isotropically from each location in the backscattering plane is subjected to an additional m small angle forward scatterings before it is traced back to the receiver. All combinations of return signal

trajectories are then integrated to obtain the total return signal as a function of the scattering order.

A.1 Energy Distribution in a Plane Due to Forward Scattering of a Collimated Light Source

In this section, the spatial distribution of photons in a plane normal to the lidar propagation axis at range R after n small angle forward scatterings is obtained as a function of the radial distance from the lidar axis of propagation. Since the n forward scatterings cause only small angular deflections, the small angle approximation is applied and the forward directed energy can be assumed to lie in a plane normal to the axis of propagation. Referring to the geometry of Fig. A.1, let

x_i penetration depth of the i^{th} scattering event

x_o distance of the cloud boundary from the backscattering plane

θ_i scattering angle of the i^{th} scattering event in the plane of the event

ϕ_i azimuthal component of the i^{th} scattering event with respect to the plane of the last scattering event

Θ_t initial propagation angle due to transmitter beam divergence

R_c distance between the lidar and the cloud boundary

$R = x_o + R_c$.

A single scattering at the transmitter location is included to simulate the finite transmitter beam width.

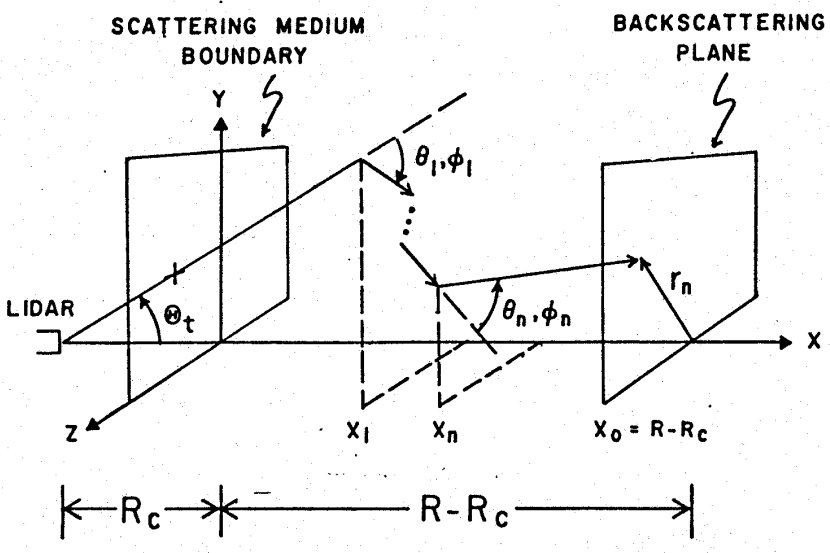

Fig. A.1 Geometry for the forward scattering of the initial laser beam from the lidar to the backscattering plane at range R. The initial propagation angle Θ_t accounts for the transmitter beam divergence.

Using the small angle approximation, the projected transverse displacement in the backscattering plane caused by the i^{th} forward scattering event is

$$(\Delta y_i^2+\Delta z_i^2)^{\frac{1}{2}} = (x_o-x_i)\tan\theta_i \simeq (x_o-x_i)\theta_i \qquad (A.3)$$

where Δy_i and Δz_i are the components of the transverse displacement with respect to the y and z axes, respectively. The radial projection r_2 of the scattered energy in the backscattering plane after two of the n forward scattering events is shown in Fig. A.2, where the initial radial displacement $\theta_t R$ is included to account for the finite transmitter beam width. The accumulated radial

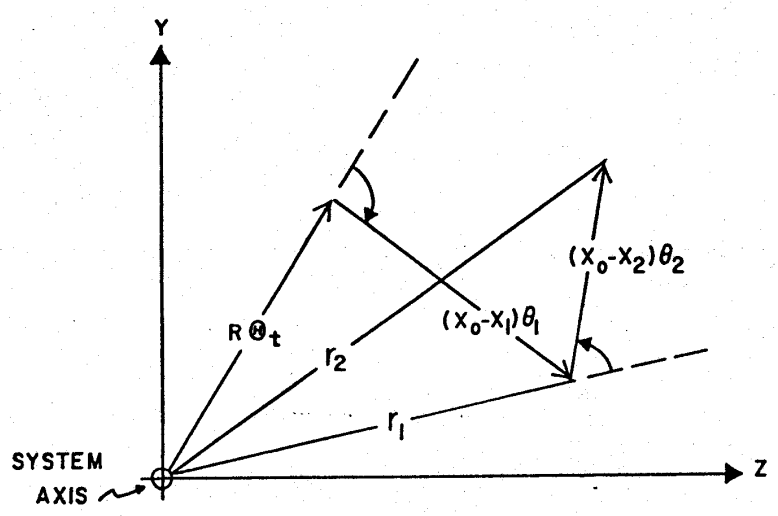

Fig. A.2 The radial projection r_2 in the backscattering plane after two of the n forward scattering events.

projection r_n of the forward scattered energy in the backscattering plane after n small angle forward scatterings can then be computed using the cosine law, such that

$$
\begin{aligned}
r_t^2 &= (\Theta_t R)^2 \\
r_1^2 &= r_t^2 + (x_o - x_1)^2\theta_1^2 - 2r_t(x_o - x_1)\theta_1 \cos(\pi - \phi_1) \\
r_2^2 &= r_1^2 + (x_o - x_2)^2\theta_2^2 - 2r_1(x_o - x_2)\theta_2 \cos(\pi - \phi_2 + \tilde{\phi}_1) \\
&\vdots \qquad\qquad\qquad\qquad \vdots \\
r_n^2 &= r_{n-1}^2 + (x_o - x_n)^2\theta_n^2 - 2r_{n-1}(x_o - x_n)\theta_n \cos(\pi - \phi_n + \tilde{\phi}_{n-1})
\end{aligned}
\qquad \text{(A.4)}
$$

QUESTION

$r_n^2 = r_{n-1}^2 + (x_o - x_n)^2 \theta_n^2 \ldots$

x_{n-1}

x_o IS POINT ALONG $R\Theta_t$ INITIALLY; IN DOING COSINE LAW, EACH NEW DISTANCE SHOULD BE $(x_{n-1} - x_n)$

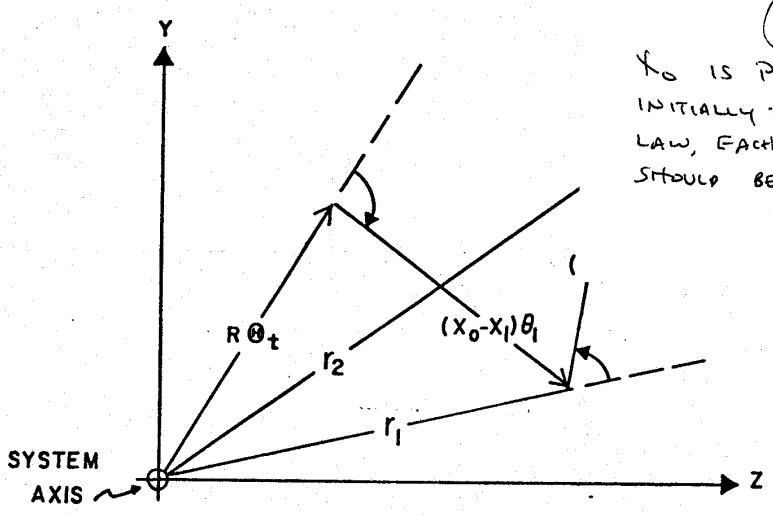

Fig. A.2 The radial projection r_2 in the backscattering plane after two of the n forward scattering events.

projection r_n of the forward scattered energy in the backscattering plane after n small angle forward scatterings can then be computed using the cosine law, such that

$$r_t^2 = (\Theta_t R)^2$$

$$r_1^2 = r_t^2 + (x_o - x_1)^2\theta_1^2 - 2r_t(x_o - x_1)\theta_1 \cos(\pi - \phi_1)$$

$$r_2^2 = r_1^2 + (x_o - x_2)^2\theta_2^2 - 2r_1(x_o - x_2)\theta_2 \cos(\pi - \phi_2 + \tilde{\phi}_1)$$

$$\vdots \qquad\qquad \vdots$$

$$r_n^2 = r_{n-1}^2 + (x_o - x_n)^2\theta_n^2 - 2r_{n-1}(x_o - x_n)\theta_n \cos(\pi - \phi_n + \tilde{\phi}_{n-1}) \qquad (A.4)$$

It can be seen by inspection of Fig. A.2 that the azimuthal angles $\tilde{\phi}_j$ are functions of all previous angles and distances with subscripts $k \leq j$. Since the θ_i and ϕ_i are independent, an average over all realizations of each ϕ_i will eliminate each term which includes the factor $\cos(\pi-\phi_i+\tilde{\phi}_{i-1})$, and it follows from Eqs. A.4 that

$$r_n^2 = (\Theta_t R)^2 + (x_o-x_1)^2\theta_1^2 +\ldots+ (x_o-x_n)^2\theta_n^2 \qquad (A.5)$$

The mean radial displacement after n forward scatterings at the fixed positions (x_o-x_i) for $i=1,\ldots,n$ can then be found by convoluting the scattering angles θ_i with the forward scattering phase function at each fixed scattering position. It follows that

$$\langle(x_o-x_i)^2\theta_i^2\rangle = \frac{2(x_o-x_i)^2}{\langle\Theta_f^2\rangle_i}\int_0^\infty \exp\left[\frac{-\theta_i^2}{\langle\Theta_f^2\rangle_i}\right]\theta_i^3 d\theta_i$$

$$= (x_o-x_i)^2\langle\Theta_f^2\rangle_i \qquad (A.6)$$

where $\langle\Theta_f^2\rangle_i$ is the mean square angle for forward scattering at the fixed position x_o-x_i. Similarly, the average radial displacement caused by the finite transmitter

beam width is found by convolution over the angular distribution of the transmitted power

$$P(\theta_t) = \frac{P_o}{\pi<\theta_t^2>} \exp[-\frac{\theta_t^2}{<\theta_t^2>}] \cdot \delta(t-R/c)\delta(y)\delta(z) \qquad (A.7)$$

where $<\theta_t^2>^{1/2}$ represents the half angle transmitter beam divergence and $\delta(t-R/c)$ is the Dirac delta function. It follows that the mean square radial displacement of the forward scattered radiation in the backscattering plane is

$$<r_n^2> = R^2<\theta_t^2> + \sum_{i=1}^{n} (x_o-x_i)^2<\theta_f^2>_i \qquad (A.8)$$

The probability distribution of forward scattered energy in the backscattering plane at range R is therefore a Gaussian function of the radial displacement r and is independent of the azimuthal angle ϕ, such that

$$\text{Prob}_f(r,\phi)rdrd\phi = \frac{1}{\pi} \frac{\exp\left\{\frac{-r^2}{R^2<\theta_t^2> + \sum_{i=1}^{n} (x_o-x_i)^2<\theta_f^2>_i}\right\}}{R^2<\theta_t^2> + \sum_{i=1}^{n} (x_o-x_i)^2<\theta_f^2>_i} rdrd\phi \qquad (A.9)$$

A.2 Energy Distribution due to Small Angle Multiple Forward Scattering of an Isotropic Point Source

A derivation of the angular distribution of energy from an isotropic point source after m small angle

forward scatterings is presented in this section. This distribution describes the angular spread of scattered energy at any location on the surface of a sphere with radius R centered on the point source. The central isotropic source represents the energy emanating from a point in the backscattering plane after the single large angle scattering event.

Consider a series of m forward scatterings in spherical coordinates at radial distances $\tilde{x}_j$ from an isotropic energy source with scattering angles θ_j for $j = n+1,\ldots,n+m$. Let φ_j represent the angle between the direction of propagation of the scattered energy and the radius vector from the isotropic point source to the radial position $\tilde{x}_j$. After a single small angle forward scattering through angles θ_j, ϕ_j at position $\tilde{x}_j$ as shown in Fig. A.3, the new angle φ'_{j+1} between the propagation direction and the radius vector from the isotropic point source, using small angle approximations, is

$$\varphi'_{j+1} \simeq \{\theta_j^2 + \varphi_j^2 - 2\theta_j\varphi_j \cos \phi_j\}^{\frac{1}{2}} \qquad (A.10)$$

The scattered energy continues in the new direction until it is scattered at the radial position $\tilde{x}_{j+1}$. As shown in Fig. A.4, the propagation angle with respect to the source radius vector at poistion $\tilde{x}_{j+1}$ is

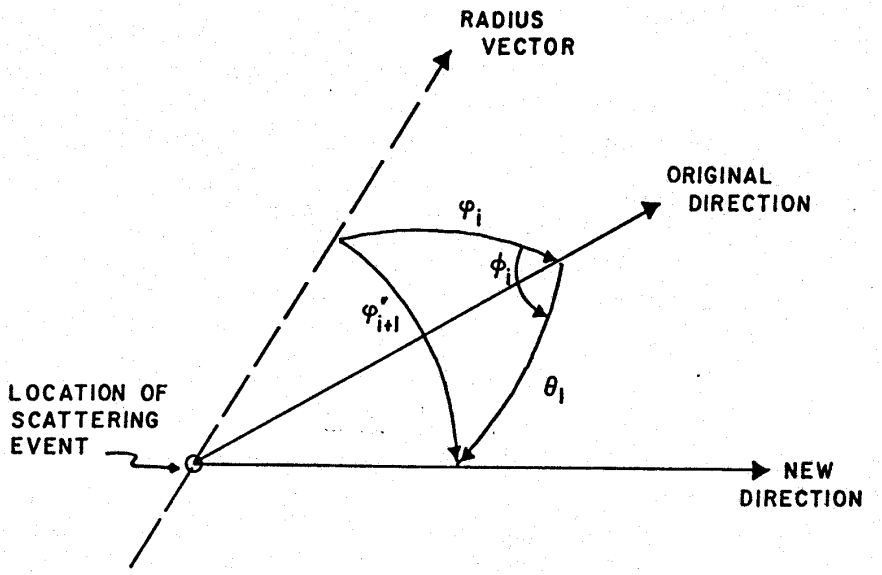

Fig. A.3 The angle φ'_{j+1} between the propagation direction and the radius vector from the isotropic point source after a single small angle forward scattering through the angles θ_j, ϕ_j .

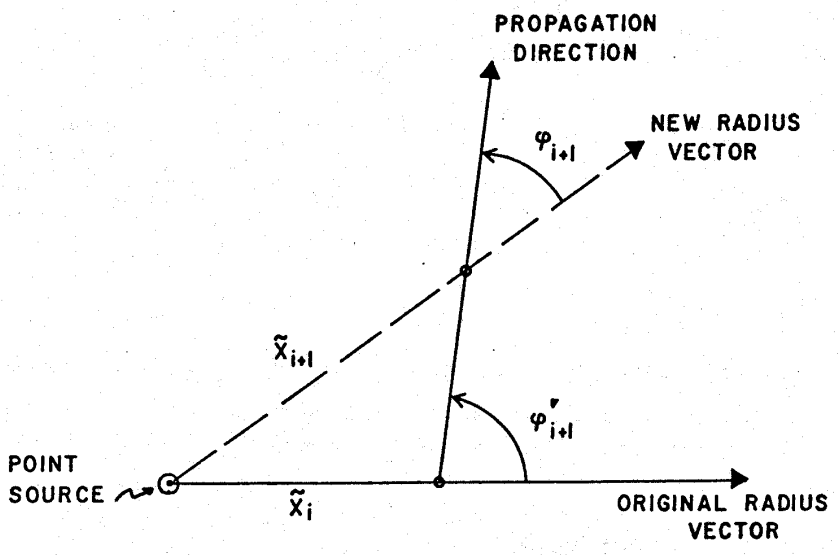

Fig. A.4 The angle φ_{j+1} between the propagation direction and the radius vector from the isotropic point source before the (j+1)rst scattering at radial position $\tilde{x}_{j+1}$.

$$\varphi_{j+1} \simeq \varphi'_{j+1} \frac{\tilde{x}_j}{\tilde{x}_{j+1}} \tag{A.11}$$

where φ'_{j+1} is given by Eq. A.10.

The azimuthal scattering angles ϕ_j are independent and randomly distributed, and an average over all realizations of the ϕ_j simplifies Eqs. A.10 and A.11 such that

$$\varphi_{j+1} \simeq \frac{\tilde{x}_j}{\tilde{x}_{j+1}} (\theta_j^2 + \varphi_j^2)^{1/2} \tag{A.12}$$

Since the source energy leaves the point source with $\varphi_0 = 0$, it follows that the propagation angle with respect to the source radius vector after m small angle forward scatterings is

$$\varphi \simeq \left\{ \sum_{j=n+1}^{n+m} \frac{\tilde{x}_j^2}{R^2} \theta_j^2 \right\}^{1/2} \tag{A.13}$$

The mean scattering angle at range R is again found by convolution with the forward scattering phase function given by Eq. A.1. Since this function is Gaussian, the resulting angular distribution at range R is also Gaussian with the characteristic mean square distribution angle

$$\langle \varphi^2 \rangle = \sum_{j=n+1}^{n+m} \frac{\tilde{x}_j^2}{R^2} \langle \Theta_f^2 \rangle_j \tag{A.14}$$

The angular distribution of photons at radial distance

R about the radius vector from the isotropic point source is then

$$\text{Prob}_b(\varphi,\phi)\varphi d\varphi d\phi = \frac{\exp\left\{\dfrac{-\varphi^2}{\sum_{j=n+1}^{n+m} \frac{\tilde{x}_j^2}{R^2} \langle\theta_f^2\rangle_j}\right\}}{\pi \sum_{j=n+1}^{n+m} \frac{\tilde{x}_j^2}{R^2} \langle\theta_f^2\rangle_i} \varphi d\varphi d\phi \qquad \text{(A.15)}$$

A.3 The N^{th} Order Scattering Contribution with a Single Isotropic Backscattering

The results of sections A.1 and A.2 are now used to obtain the contribution of N^{th} order scattering to the return signal of a monostatic lidar system. The geometry of the return path to the lidar receiver for energy from a point source at r, ϕ in the backscattering plane is shown in Fig. A.5. The result of section A.1 (Eq. A.9) is used to describe the energy distribution with respect to r and ϕ in the backscattering plane. The result of section A.2 (Eq. A.15) is used to describe the angular distribution of energy at the lidar receiver after the single large angle isotropic scattering at r, ϕ in the backscattering plane. These contributions to the lidar return signal are then integrated to obtain the total received signal due to N^{th} order scattering.

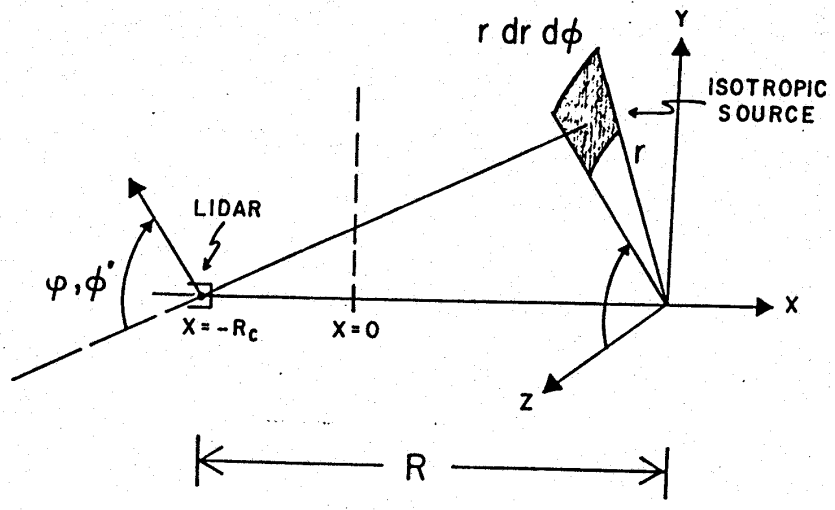

Fig. A.5 The geometry of the return path to the lidar receiver for energy emanating from a point source at r, ϕ in the backscattering plane.

The total energy from the backscattering plane element $r\ dr\ d\phi$ which is collected by the lidar receiver can be determined by integration over the receiver field of view. This integration can be carried out over the spherical coordinates φ, ϕ' between the limits φ_ℓ, φ_u and ϕ'_ℓ, ϕ'_u which are to be determined. The energy which is collected by the receiver from all sources of scattered light in the backscattering plane is then proportional to

$$\text{Prob}_{rec} = \int_0^{2\pi} d\phi \int_0^{\infty} r\,dr\ \text{Prob}_f(r,\phi) \cdot \int_{\phi'_\ell}^{\phi'_u} d\phi' \int_{\varphi_\ell}^{\varphi_u} \varphi\, d\varphi\ \text{Prob}_b(\varphi,\phi') \qquad (A.16)$$

where $\text{Prob}_f(r,\phi)$ and $\text{Prob}_b(\varphi,\phi')$ are given by Eqs.

A.9 and A.15, respectively. Eq. A.16 can be readily solved if the polar integration coordinates r, ϕ are transformed to the cartesian coordinates y', z'. Letting α' and γ' represent displacements in the direction φ, ϕ' along the y', z' axes, respectively, then Eq. A.16 becomes

$$\text{Prob}_{rec} = \int_{-\infty}^{\infty} dy' \cdot \int_{-\infty}^{\infty} dz' \, \frac{1}{\pi} \frac{\exp\left\{ - \dfrac{y'^2 + z'^2}{R^2\langle\theta_t^2\rangle + \sum_{i=1}^{n} (x_o - x_i)^2 \langle\theta_f^2\rangle_i} \right\}}{R^2\langle\theta_t^2\rangle + \sum_{i=1}^{n} (x_o - x_i)^2 \langle\theta_f^2\rangle_i} \cdot \text{Prob}_{y'z'} \qquad \text{(A.17)}$$

where

$$\text{Prob}_{y'z'} = \int_{\alpha_\ell'}^{\alpha_u'} d\alpha' \int_{\gamma_\ell'}^{\gamma_u'} d\gamma' \, \frac{1}{\pi} \frac{\exp\left\{ - \dfrac{\alpha'^2 + \gamma'^2}{\sum_{j=n+1}^{n+m} \dfrac{\tilde{x}_j^2}{R^2} \langle\theta_f^2\rangle_j} \right\}}{\sum_{j=n+1}^{n+m} \dfrac{\tilde{x}_j^2}{R^2} \langle\theta_f^2\rangle_j} \qquad \text{(A.18)}$$

and

$$\alpha' = \varphi \cos \phi' \qquad \text{(A.19a)}$$

$$\gamma' = \varphi \sin \phi' \qquad \text{(A.19b)}$$

The parameters α_ℓ', α_u' and γ_ℓ', γ_u' represent the upper and lower limits of the transformed angles. These integration limits can be determined when they are transformed

to the angles α, γ about the lidar propagation axis, such that

$$\alpha \simeq \alpha' + y'/R \tag{A.20a}$$

$$\gamma \simeq \gamma' + z'/R \tag{A.20b}$$

The half width receiver field of view ψ is related to the transformed angles by

$$\psi^2 = \alpha^2 + \gamma^2 \tag{A.21}$$

If the integration over α is performed between the limits $\pm\psi$, then the integration over γ must be carried out between the limits $\gamma = \pm (\psi^2-\alpha^2)^{\frac{1}{2}}$, and Eq. A.18 becomes

$$\text{Prob}_{y'z'} = \int_{-\psi}^{+\psi} d\alpha \int_{-(\psi^2-\alpha^2)^{\frac{1}{2}}}^{+(\psi^2-\alpha^2)^{\frac{1}{2}}} d\gamma \, \frac{1}{\pi} \frac{\exp\left\{ - \frac{(\alpha-y'/R)^2+(\gamma-z'/R)^2}{\sum_{j=n+1}^{n+m} \frac{\tilde{x}_j^2}{R^2} \langle\theta_f^2\rangle_j} \right\}}{\sum_{i=n+1}^{n+m} \frac{\tilde{x}_j^2}{R^2} \langle\theta_f^2\rangle_j} \tag{A.22}$$

Eqs. A.17 and A.22 can now be readily integrated over the variables y', z', with the result

$$\text{Prob}_{rec} = \frac{R^2}{\pi \mathbb{B}} \int_{-\psi}^{+\psi} d\alpha \int_{-(\psi^2-\alpha^2)^{\frac{1}{2}}}^{+(\psi^2-\alpha^2)^{\frac{1}{2}}} d\gamma \, \exp\left(\frac{-R^2(\alpha^2+\gamma^2)}{\mathbb{B}}\right) \text{erfc}\left(\frac{-\alpha R}{\mathbb{A}}\right) \text{erfc}\left(\frac{-\gamma R}{\mathbb{A}}\right) \tag{A.23}$$

where

$$\mathbb{A} = 1 + \frac{\sum_{j=n+1}^{n+m} \tilde{x}_j^2 \langle\theta_f^2\rangle_j}{R^2\langle\theta_t^2\rangle + \sum_{i=1}^{n} (x_o - x_i)^2 \langle\theta_f^2\rangle_i} \qquad \text{(A.24a)}$$

and

$$\mathbb{B} = R^2\langle\theta_t^2\rangle + \sum_{i=1}^{n} (x_o - x_i)^2 \langle\theta_f^2\rangle_i + \sum_{j=n+1}^{n+m} \tilde{x}_j^2 \langle\theta_f^2\rangle_i \qquad \text{(A.24b)}$$

Transforming Eq. A.23 back to spherical coordinates, it follows that

$$\text{Prob}_{rec} = \frac{R^2}{\pi\mathbb{B}} \int_0^{2\pi} d\phi \int_0^{\psi} \theta d\theta \, \exp\left(-\frac{R^2\theta^2}{\mathbb{B}}\right) \text{erfc}\left(\frac{-R\theta}{\mathbb{A}} \cos\phi\right) \text{erfc}\left(\frac{-R\theta}{\mathbb{A}} \sin\phi\right) \qquad \text{(A.25)}$$

Since $\text{erfc}(x) = 1 - \text{erf}(x)$ and $\text{erf}(-x) = -\text{erf}(x)$ is an odd function, the integral over ϕ in Eq. A.25 can be eliminated using the relation

$$\int_0^{2\pi} d\phi \, \text{erfc}\left(\frac{-R\theta}{\mathbb{A}} \cos\phi\right) \text{erfc}\left(\frac{-R\theta}{\mathbb{A}} \sin\phi\right) = 2\pi \qquad \text{(A.26)}$$

Eq. A.23 is then readily integrated, such that

$$\text{Prob}_{rec} = 1 - \exp\left(\frac{-R^2\psi^2}{\mathbb{B}}\right) \qquad \text{(A.27)}$$

where $\mathbb{B}$ is given by Eq. A.24b.

Eqs. A.27 and A.24b represent the relative detection probability for energy which undergoes n forward scatterings at fixed locations $(x_o - x_i)$ for $i=1,\ldots,n$,

one large angle scattering at range R, and m small angle forward scatterings at fixed locations $\tilde{x}_j$ for $j=n+1,\ldots,n+m$ on the return path to the receiver. The energy which is collected by the receiver telescope can be obtained in absolute units by multiplying Eq. A.27 by the scattering probabilities at the fixed locations (x_o-x_i) and $\tilde{x}_j$, such that

$$dP_{n,m} = P_o e^{-2\tau} \prod_{i=1}^{n} a(x_i)\beta(x_i)dx_i \prod_{j=n+1}^{n+m} a(\tilde{x}_j)\beta(\tilde{x}_j)d\tilde{x}_j$$

$$\text{Prob}(x_1,\ldots,x_n,\tilde{x}_{n+1},\ldots\tilde{x}_{n+m}) \qquad (A.28)$$

where

P_o	transmitted power
a	the fraction of the total scattered energy which is defined by the forward scattering phase function
β	extinction coefficient
τ	optical depth between the lidar and the location of the backscattering event.

A final integration over the range of scattering event locations must be performed to obtain the total received energy due to multiple scattering throughout the entire scattering medium. Letting $\tilde{x}_j = x_o - x_{j+n}$, it follows that the ratio of N^{th} order scattering to single scattering for n small angle scatterings in the forward direction

and m small angle scatterings in the backward direction is

$$\frac{P_{n,m}}{P_o} = \int_0^{x_o} dx_1 \int_0^{x_1} dx_2 \cdots \int_0^{x_{n-1}} dx_n \cdot \int_0^{x_o} dx_{n+1} \int_{x_{n+1}}^{x_o} dx_{n+2} \cdots \int_{x_{n+m-1}}^{x_o} dx_{n+m} \cdot$$

$$\cdot \prod_{i=1}^{n+m} a(x_i)\beta(x_i)\{1-\exp[-\frac{\psi^2}{\langle\theta_t^2\rangle + \sum_{i=1}^{n+m} \frac{(x_o-x_i)^2}{R^2}\langle\theta_f^2\rangle_i}]\} \quad (A.29)$$

where $0 \leq n \leq N-1$. The solution to this problem can be written in terms of a dimensionless distance parameter $u = x/(R-R_c)$, such that

$$\frac{P_{n,m}}{P_1} = \tau^{n+m} \int_0^1 du_1 \int_0^{u_1} du_2 \cdots \int_0^{u_{n-1}} du_n \cdot \int_0^1 du_{n+1} \int_{u_{n+1}}^1 du_{n+2} \cdots \int_{u_{n+m-1}}^1 du_{n+m} \cdot$$

$$\prod_{i=1}^{n+m} a(u_i)\rho(u_i)\{1 - \exp[\frac{-\psi^2}{\langle\theta_t^2\rangle + (\frac{R-R_c}{R})^2 \sum_{j=1}^{n+m} \langle\theta_f^2\rangle_j u_j^2}]\} \quad (A.30)$$

where

$\tau = \int_{R_c}^{R} \beta(R)dr$ one way optical depth between the lidar and the backscattering event location

$a(u)$ range variation of the fraction of total scattered energy which is defined by the forward scattering phase function

$\rho(u) = \beta(u)/\langle\beta\rangle$ spatial structure of the optical extinction coefficient β about the mean value $\langle\beta\rangle = \tau/(R-R_c)$

$R-R_c$ penetration depth, where R_c is the distance between the scattering medium boundary and the lidar

$\langle\theta_t^2\rangle$ mean square angle of the transmitter beam divergence

$\langle\theta_f^2\rangle$ mean square angle for forward scattering.

Eq. A.30 can be used to estimate the contribution of multiple scattering to the lidar return signal from a spatially inhomogeneous medium of isotropically backscattering particles. The total return signal P_N due to N^{th} order multiple scattering from such a medium can be obtained by summing the various combinations $P_{n,m}$, such that

$$\frac{P_N}{P_1} = \sum_{n=0}^{N-1} \frac{P_{n,m}}{P_1} \qquad (A.31)$$

where $m = N-n-1$. When $\psi^2 >> \langle\theta_f^2\rangle$ and $\rho(u) = 1$, it can be seen by inspection of Eq. A.30 that the components $P_{n,m}$ are related to $P_{N-1,0}$ by

$$P_{n,m} = \frac{(n+m)!}{n!m!} P_{n+m,0} \qquad (A.32)$$

Assuming that Eq. A.32 holds in general, then the total return signal due to N^{th} order multiple scattering from a spatially inhomogeneous medium of isotropically backscattering particles is

$$\frac{P_n}{P_1} = 2^{N-1}\langle a\rangle^{N-1}\,\frac{\langle \mathbb{P}(\pi)\rangle_N}{\mathbb{P}(\pi)}\,A_N\,\frac{\tau^{N-1}}{(N-1)!} \tag{A.33}$$

where the non-dimensional coefficient $A_N(\psi^2, \langle\theta_f^2\rangle, \langle\theta_t^2\rangle, \frac{R-R_c}{R})$ is given by

$$A_N = (N-1)!\int_0^1 du_1 \int_0^{u_1} du_2 \cdots \int_0^{u_{N-2}} du_{N-1} \cdot \prod_{i=1}^{N-1} \frac{a(u_i)\rho(u_i)}{\langle a\rangle} \cdot$$

$$\cdot \left\{1-\exp\left[\frac{-\psi^2}{\langle\theta_t^2\rangle + (\frac{R-R_c}{R})^2 \sum_{j=1}^{N-1} \langle\theta_f^2\rangle_j\, u_j^2}\right]\right\} \tag{A.34}$$

The average value of the backscatter phase function $\frac{\langle \mathbb{P}(\pi)\rangle_N}{\mathbb{P}(\pi)}$ is included in Eq. A.33 to account for the effects of anisotropic backscattering, and it must be estimated independently in this formulation for isotropic backscattering.

A.4 The Contribution of Double Scattering with Anisotropic Backscattering

The double scattering contribution to the return signal of a monostatic lidar is obtained in this section for the case of anisotropic backscattering. Referring to the geometry of Fig. A.6, the parameters for this problem are defined as in the previous sections, with the addition

of a backscattering phase function which is Gaussian in angle, such that

$$\frac{\mathbb{P}_b(\theta)}{4\pi} = \frac{\mathbb{P}(\pi)}{4\pi} \exp\left[-\frac{(\pi-\theta)^2}{\langle\theta_b^2\rangle}\right] \tag{A.35}$$

It is still assumed that the single forward scattering gives rise to small angular deflections, and the small angle approximations are used. The initial energy distribution of the lidar transmitter is assumed to be a Dirac delta function in time and angle in this section.

The energy which is scattered in the forward direction at location x to the backscattering element at range R is

$$dI = P_o e^{-\tau} \beta(x) \frac{\mathbb{P}_f(\theta)}{4\pi} \theta d\theta d\phi dx \tag{A.36}$$

where

$$\theta = \tan^{-1} \frac{r}{x_o - x} \simeq \frac{r}{x_o - x} \tag{A.37}$$

The energy collected by the receiver after a single large angle scattering at range R is then

$$dI_{rec} = P_o e^{-2\tau} \beta(x)\beta(x_o)\Delta x \frac{\mathbb{P}_f(\theta)}{4\pi} \frac{\mathbb{P}_b(\pi-\theta+\tilde{\phi})}{4\pi} \frac{rdr}{(x_o-x)^2} d\phi dx \tag{A.38}$$

where Δx is the thickness of the backscattering plane and

$$\tilde{\phi} \simeq r/R \tag{A.39}$$

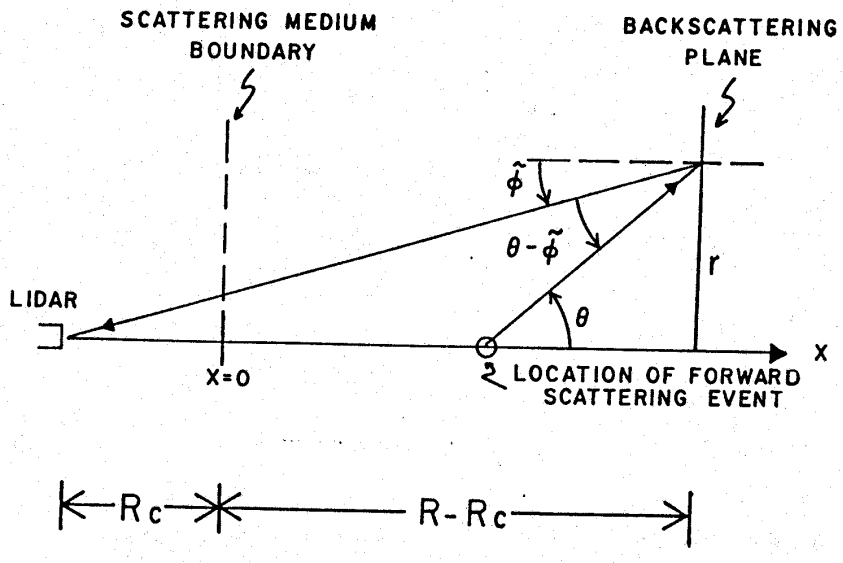

Fig. A.6 Geometry for the derivation of the double scattering contribution with one anisotropic backscattering at range R from the lidar. The small angle forward scattering occurs at penetration depth x , and the lidar transmitter is restricted to zero transmitter beam divergence.

It follows that energy which is collected by the receiver from all sources of backscattered light is

$$I_{rec} = P_o e^{-2\tau} \frac{P(\pi)}{4\pi} \beta(x_o)\Delta x \int_0^{x_o} dx \, \frac{a(x)\beta(x)}{\pi\langle\theta_f^2\rangle} \cdot$$

$$\cdot \int_0^{2\pi} d\phi \int_0^{r_o} \frac{r\,dr}{(x_o-x)^2} \exp\left\{\frac{-r^2}{(x_o-x)^2}\left[\frac{1}{\langle\theta_f^2\rangle} + \frac{(1-\frac{x_o-x}{R})^2}{\langle\theta_b^2\rangle}\right]\right\} \tag{A.40}$$

where $r_o = R\psi$ is the limit imposed by the receiver field of view. Eq. A.40 is readily integrated over r and

ϕ , such that

$$I_{rec} = P_o e^{-2\tau} \frac{\mathbb{P}(\pi)}{4\pi} \beta(x_o)\Delta x \int_0^{x_o} dx \, \frac{a(x)\beta(x)}{\langle\theta_f^2\rangle} \cdot$$

$$\cdot \frac{1}{\mathbb{D}(x)} \{1 - \exp[-\frac{\mathbb{D}(x)R^2\psi^2}{(x_o-x)^2}]\} \qquad (A.41)$$

where

$$\mathbb{D}(x) = \frac{1}{\langle\theta_f^2\rangle} + \frac{(1 - \frac{x_o-x}{R})^2}{\langle\theta_b^2\rangle} \qquad (A.42)$$

The ratio of double scattering to single scattering for the case of a single forward scattering prior to the large angle scattering is then

$$\frac{P_{1,0}}{P_0} = \int_0^{x_o} dx \, \frac{a(x)\beta(x)}{\mathbb{D}(x)\langle\theta_f^2\rangle} \{1 - \exp[-\frac{\mathbb{D}(x)R^2\psi^2}{(x_o-x)^2}]\} \qquad (A.43)$$

It can be seen by inspection of Fig. A.6 that the case for forward scattering after the single large angle scattering will produce a result identical to Eq. A.43, such that $P_{1,0} = P_{0,1}$.

Transforming the Eq. A.43 result to the dimensionless penetration depth $u = x/(R-R_c)$, the ratio of second order scattering to single scattering with anisotropic backscattering is

$$\frac{P_2}{P_1} = \tau \int_0^1 du\ 2a(u)\rho(u) \frac{1-\exp\left\{ -\dfrac{1+Q(1-\frac{R-R_c}{R}u)^2}{u^2} \dfrac{\psi^2}{\langle\theta_f^2\rangle} \right\}}{1+Q(1-\frac{R-R_c}{R}u)^2} \qquad \text{(A.44)}$$

where $Q = \langle\theta_f^2\rangle/\langle\theta_b^2\rangle$. Eq. A.44 reduces to Eq. A.30 in the case of a spatially homogeneous medium with isotropic backscattering [$\lim \langle\theta_b^2\rangle \to \infty$] . With an additional limit of large receiver field of view, Eq. A.44 can be readily integrated such that

$$\lim_{\psi\to\infty} \frac{P_2}{P_1} = 2\langle a\rangle\tau \frac{R}{R-R_c} \frac{1}{\sqrt{Q}} \{\tan^{-1}\sqrt{Q} - \tan^{-1}(\frac{R_c}{R}\sqrt{Q})\} \qquad \text{(A.45)}$$

Appendix B

Derivation of the Neumann Solution for the Multiple Scattering Contribution to a Monostatic Lidar Signal

The Neumann solution for the contribution of multiple scattering to a monostatic lidar signal is derived in this appendix. This derivation follows the procedure outlined in section 3.2, and it uses the parameter definitions which are given in that section and Fig. 3.1. Due to the large number of parameters required to characterize this problem, the following definitions are used to reduce the number of terms:

1. Combinations of Gaussian phase function parameters

$$\Gamma_{n,s,\ell} = \gamma_{f,i_{n+\ell}} \Gamma_{n,s,\ell-1} \; ; \qquad 1 \leq \ell \leq m \qquad \text{(B.1a)}$$

$$\Gamma_{n,s,0} = \gamma_{b,s} \Gamma_{n,0,0} \qquad \text{(B.1b)}$$

$$\Gamma_{\ell,0,0} = \gamma_{f,i_{\ell}} \Gamma_{\ell-1,0,0} \; ; \qquad 1 \leq \ell \leq n \qquad \text{(B.1c)}$$

$$\Gamma_{0,0,0} = \gamma_{t} \qquad \text{(B.1d)}$$

$$\Delta_{n,s,\ell} = \gamma_{f,i_{n+\ell}} \Delta_{n,s,\ell-1} + \Gamma_{n,s,\ell-1} \; ; \qquad 1 \leq \ell \leq m \qquad \text{(B.2a)}$$

$$\Delta_{n,s,0} = \gamma_{b,s} \Delta_{n,0,0} + \Gamma_{n,0,0} \qquad \text{(B.2b)}$$

$$\Delta_{\ell,0,0} = \gamma_{f,i_{\ell}} \Delta_{\ell-1,0,0} + \Gamma_{\ell-1,0,0} \; ; \qquad 1 \leq \ell \leq n \qquad \text{(B.2c)}$$

$$\Delta_{0,0,0} = 1 \qquad \text{(B.2d)}$$

2. Polynomials in penetration depth

$$\left.\begin{aligned} A_{n,s,\ell} &= (x_{n+\ell}-x_{n+\ell+1}) + \gamma_{f,i_{n+\ell}} \frac{\Delta_{n,s,\ell-1}}{\Delta_{n,s,\ell}} A_{n,s,\ell-1} \\ &\qquad 1 \le \ell \le m \end{aligned}\right\} x_{n+m+1} = 0 \qquad \text{(B.3a)}$$

$$A_{n,s,0} = (R-R_c-x_{n+1}) - \gamma_{b,s} \frac{\Delta_{n,0,0}}{\Delta_{n,s,0}} A_{n,0,0} \qquad \text{(B.3b)}$$

$$\left.\begin{aligned} A_{\ell,0,0} &= (x_{\ell+1}-x_\ell) + \gamma_{f,i_\ell} \cdot \frac{\Delta_{\ell-1,0,0}}{\Delta_{\ell,0,0}} A_{\ell-1,0,0} \\ &\qquad 1 \le \ell \le n \end{aligned}\right\} x_{n+1} = R-R_c \qquad \text{(B.3c)}$$

$$A_{0,0,0} = (x_1 + R_c) \qquad \text{(B.3d)}$$

$$B_{n,s,\ell} = B_{n,s,\ell-1} + \frac{\Delta_{n,s,\ell-1}}{\Delta_{n,s,\ell}} A^2_{n,s,\ell-1}, \qquad 1 \le \ell \le m \qquad \text{(B.4a)}$$

$$B_{n,s,0} = B_{n,0,0} + \frac{\Delta_{n,0,0}}{\Delta_{n,s,0}} A^2_{n,0,0} \qquad \text{(B.4b)}$$

$$B_{\ell,0,0} = B_{\ell-1,0,0} + \frac{\Delta_{\ell-1,0,0}}{\Delta_{\ell,0,0}} A^2_{\ell-1,0,0}, \qquad 1 \le \ell \le n \qquad \text{(B.4c)}$$

$$B_{0,0,0} = 0 \qquad \text{(B.4d)}$$

3. Integral operators

$$\square_{n,s,\ell} = \exp\left[-\int_{x_{n+\ell+1}}^{x_{n+\ell}} \beta(x)dx\right] \cdot \int_{x_{n+\ell+1}}^{R-R_c} dx_{n+\ell}\beta(x_{n+\ell}) \cdot \sum_{i_{n+\ell}=1}^{I} a_{i_{n+\ell}}(x_{n+\ell}) \cdot$$

$$\cdot \gamma_{f,i_{n+\ell}}(x_{n+\ell})\, \square_{n,s,\ell-1} \quad \text{for } 1 \le \ell \le m \qquad \text{(B.5a)}$$

$$\square_{n,s,0} = \exp\left[-\int_{x_{n+1}}^{R-R_c} \beta(x)dx\right] \cdot \beta(R-R_c) \sum_{s=1}^{S} \frac{P_s(\pi)}{4\pi} \cdot \square_{n,0,0} \qquad \text{(B.5b)}$$

$$\square_{\ell,0,0} = \exp\left[-\int_{x_\ell}^{x_{\ell+1}} \beta(x)dx\right] \cdot \int_0^{x_{\ell+1}} dx_\ell \beta(x_\ell) \cdot \sum_{i=1}^{I} a_{i_\ell}(x_\ell)\gamma_{f_{i_\ell}}(x_\ell)\square_{\ell-1,0,0}$$

$$\text{for } 1 \le \ell \le n \text{ and } x_{n+1} = R-R_c \qquad \text{(B.5c)}$$

$$\square_{0,0,0} = \exp\left[-\int_0^{x_1} \beta(x)dx\right] \qquad \text{(B.5d)}$$

The symbols $\boldsymbol{\xi}$ and $\boldsymbol{\xi}'$ are used to represent the parameter sets $[p,q,\eta,\zeta]$ and $[p,q,\eta',\zeta']$, respectively. From Eq. 3.23

$$\hat{i}_o(0,\boldsymbol{\xi}) = \frac{\gamma_t}{2\pi^2} \exp\{-\gamma_t(\eta^2+\zeta^2)+\hat{j}(\eta p+\zeta q)R_c\} \qquad \text{(B.6a)}$$

From Eq. 3.24a

$$\hat{i}_o(x_1,\boldsymbol{\xi}) = \hat{i}_o(0,\boldsymbol{\xi}) \exp\left\{-\int_0^{x_1} \beta dx+\hat{j}(\eta p+\zeta q)x_1\right\} \qquad \text{(B.6b)}$$

$$\boxed{\hat{i}_o(x_1,\boldsymbol{\xi}) = \frac{\gamma_t}{2\pi^2} \frac{\square_{0,0,0}}{\Delta_{0,0,0}} \exp\left\{-\frac{\Gamma_{0,0,0}}{\Delta_{0,0,0}}(\eta^2+\zeta^2)+\hat{j}(\eta p+\zeta q)A_{0,0,0}\right\}} \qquad \text{(B.6c)}$$

From Eqs. 3.24b and 3.24c

$$\hat{i}_1(x_2,\boldsymbol{\rho}) = \int_0^{x_2} dx_1\ \beta(x_1) \sum_{i_1=1}^{I} \frac{a_i\ \gamma_{f,i_1}}{\pi} \int_{-\infty}^{\infty}\int_{-\infty}^{\infty} \hat{i}_o(x_1,\boldsymbol{\rho}')\cdot\exp\{-\gamma_{f,i_1}[(\eta'-\eta)^2+(\zeta'-\zeta)^2]$$

$$-\int_{x_1}^{x_2} \beta dx + \hat{j}(\eta p+\zeta q)(x_2-x_1)\}d\eta' d\zeta' \qquad \text{(B.7a)}$$

or

$$\boxed{\hat{i}_1(x_2,\boldsymbol{\rho}) = \frac{\gamma_t}{2\pi^2}\frac{\square_{1,0,0}}{\Delta_{1,0,0}} \exp\{-\frac{\Gamma_{1,0,0}}{\Delta_{1,0,0}}(\eta^2+\zeta^2)+\hat{j}(\eta p+\zeta q)A_{1,0,0} - \frac{1}{4}(p^2+q^2)B_{1,0,0}\}} \qquad \text{(B.7b)}$$

By induction, it follows that

$$\boxed{\hat{i}_n(R-R_c,\boldsymbol{\rho}) = \frac{\gamma_t}{2\pi^2}\frac{\square_{n,0,0}}{\Delta_{n,0,0}} \exp\{-\frac{\Gamma_{n,0,0}}{\Delta_{n,0,0}}(\eta^2+\zeta^2) + \hat{j}(\eta p+\zeta q)A_{n,0,0} - \frac{1}{4}(p^2+q^2)B_{n,0,0}\}} \qquad \text{(B.8)}$$

Now perform the large angle scattering at $R-R_c$. From Eq. 3.27

$$\hat{\hat{i}}_{n,0}(x_{n+1},\boldsymbol{\rho}) = \beta(R-R_c) \sum_{s=1}^{S} \frac{P_s(\pi)}{4\pi} \cdot\exp\{-\int_{x_{n+1}}^{R-R_c} \beta dx + \hat{j}(\eta p+\zeta q)(x_o-x_{n+1})\}\cdot$$

$$\cdot\int_{-\infty}^{\infty}\int_{-\infty}^{\infty} \hat{i}_n(R-R_c,\boldsymbol{\rho}')\ \exp\{-\gamma_{b,s}[(\eta'+\eta)^2+(\zeta'+\zeta)^2]\}d\eta' d\zeta' \qquad \text{(B.9a)}$$

or

$$\boxed{\hat{\hat{i}}_{n,0}(x_{n+1},\xi) = \frac{\gamma_t}{2\pi}\frac{\square_{n,s,0}}{\Delta_{n,s,0}}\exp\left\{-\frac{\Gamma_{n,s,0}}{\Delta_{n,s,0}}(\eta^2+\zeta^2)+\hat{j}(\eta p+\zeta q)A_{n,s,0}-\frac{1}{4}(p^2+q^2)B_{n,s,0}\right\}} \qquad \text{(B.9b)}$$

From Eqs. 3.28

$$\hat{\hat{i}}_{n,1}(x_{n+2},\xi) = \int_{x_{n+2}}^{R-R_c} dx_{n+1}\beta(x_{n+1}) \sum_{i_{n+1}=1}^{I} \frac{a_{i_{n+1}}\gamma_{f,i_{n+1}}}{\pi} \int_{-\infty}^{\infty}\int_{-\infty}^{\infty} \hat{\hat{i}}_{n,0}(x_{n+1},\xi')\cdot\exp\{-\gamma_{f,i_{n+1}}[(\eta'-\eta)^2+(\zeta'-\zeta)^2]$$

$$-\int_{x_{n+2}}^{x_{n+1}}\beta dx + \hat{j}(\eta p+\zeta q)(x_{n+1}-x_{n+2})\}d\eta' d\zeta' \qquad \text{(B.10a)}$$

or

$$\boxed{\hat{\hat{i}}_{n,1}(x_{n+2},\xi) = \frac{\gamma_t}{2\pi}\frac{\square_{n,s,1}}{\Delta_{n,s,1}}\exp\left\{-\frac{\Gamma_{n,s,1}}{\Delta_{n,s,1}}(\eta^2+\zeta^2)+\hat{j}(\eta p+\zeta q)A_{n,s,1}-\frac{1}{4}(p^2+q^2)B_{n,s,1}\right\}} \qquad \text{(B.10b)}$$

Again, by induction it follows that

$$\boxed{\hat{\hat{i}}_{n,m}(x_{n+m+1}=0,\xi) = \frac{\gamma_t}{2\pi}\frac{\square_{n,s,m}}{\Delta_{n,s,m}}\exp\left\{-\frac{\Gamma_{n,s,m}}{\Delta_{n,s,m}}(\eta^2+\zeta^2)+\hat{j}(\eta p+\zeta q)A_{n,s,m}-\frac{1}{4}(p^2+q^2)B_{n,s,m}\right.} \qquad \text{(B.11)}$$

Position the receiver off-axis at $y_o = z_o = \frac{L}{\sqrt{2}}$. From Eqs. 3.32 and 3.33

$$P_{n,m} = \int_{-\psi}^{\psi}\int_{-\psi}^{\psi} d\eta d\zeta \int_{-\infty}^{\infty}\int_{-\infty}^{\infty} dpdq\ \hat{\hat{i}}_{n,m}(x=0,\mathbf{r})\cdot\tilde{r}(x=0,\mathbf{r}) \qquad \text{(B.12a)}$$

or

$$P_{n,m} = \int_{-\psi}^{\psi}\int_{-\psi}^{\psi} d\eta d\zeta\ \frac{\gamma_t}{4\pi^3\psi^2}\frac{\square_{n,s,m}}{\Delta_{n,s,m}}\exp\{-\frac{\Gamma_{n,s,m}}{\Delta_{n,s,m}}(\eta^2+\zeta^2)\}\cdot\int_{-\infty}^{\infty}\int_{-\infty}^{\infty} dpdq\cdot$$

$$\cdot\exp\{-\frac{B_{n,s,m}}{4}(p^2+q^2)+\hat{j}p[\eta(A_{n,s,m}+R_c)+\frac{L}{\sqrt{2}}]+\hat{j}q[\zeta(A_{n,s,m}+R_c)+\frac{L}{\sqrt{2}}]\} \qquad \text{(B.12b)}$$

Integrating over (p,q) and transforming the normal coordinates (η,ζ) to spherical coordinates (θ,φ), the final solution is

$$\boxed{P_{n,m} = \frac{2\gamma_t}{\pi\psi^2}\frac{\square_{n,s,m}}{\Delta_{n,s,m}B_{n,s,m}}\int_0^{\psi}\theta d\theta\ \exp\{-[\frac{(A_{n,s,m}+R_c)^2}{B_{n,s,m}}+\frac{\Gamma_{n,s,m}}{\Delta_{n,s,m}}]\theta^2-\frac{L^2}{B_{n,s,m}}\}\cdot \mathbf{I}_0[2L\theta\frac{(A_{n,s,m}+R_c)}{B_{n,s,m}}] \quad \text{for } L\geq 0} \qquad \text{(B.13)}$$

where $\mathbf{I}_0(f(\theta))$ is the modified Bessel function [cf. Abramowitz and Stegun (1965), Eq. 9.6.16]. When the lidar transmitter and receiver are coaxial, then $L = 0$ and $\mathbf{I}_0(0) = 1$, and Eq. B.13 is readily integrated over θ with the result

$$P_{n,m} = \frac{\gamma_t}{\pi\psi^2} \square_{n,s,m} \frac{1 - \exp\{-[\frac{(A_{n,s,m}+R_c)^2}{B_{n,s,m}} + \frac{\Gamma_{n,s,m}}{\Delta_{n,s,m}}]\psi^2\}}{\Delta_{n,s,m}(A_{n,s,m}+R_c)^2 + \Gamma_{n,s,m}B_{n,s,m}} \tag{B.14}$$

for $L = 0$ and where

$$\square_{n,s,m} = \exp[-2\int_0^{R-R_c} \beta(x)dx]\beta(R-R_c) \sum_{s=1}^{S} \frac{P_s(\pi)}{4\pi} \int_0^{R-R_c} dx_1 \int_0^{x_1} dx_2 \cdots \int_0^{x_{n-1}} dx_2 \cdot$$

$$\cdot \int_0^{R-R_c} dx_{n+1} \int_0^{x_{n+1}} dx_{n+2} \cdots \int_0^{x_{n+m-1}} dx_{n+m} \prod_{k=1}^{n+m} \beta(x_k) \cdot \sum_{i_k=1}^{I} a_{i_k}(x_k)\gamma_{f,i_k}(x_k) \tag{B.15}$$

Corrections to "The Measurement of Rainfall by Lidar," Ph.D. thesis by Scott T. Shipley

Some errors have been found in the multiple scattering theory. These errors are confined to Chapter 3 and Appendix B, as follows:

1. p82: Eqs. (3.36)-(3.37c) are incorrect and should be replaced by the equations given on p82a.

2. p83: Eq. (3.38) should read

$$\mathcal{L}_N = \frac{\prod_{i=1}^{N-1} a(u_i)\rho(u_i)}{D_N} \{1-\exp[\frac{-D_N\psi^2}{C_N + \langle\theta_t^2\rangle D_N}]\} \cdot \{1-\exp[-\frac{\psi^2}{\langle\theta_t^2\rangle}]\}^{-1} \qquad (3.38)$$

3. p84: The bottom line of Eq. (3.39a) should read

$$- \frac{L^2}{R^2}(\frac{1}{\langle\theta_t^2\rangle} + \frac{1}{\langle\theta_b^2\rangle}) \cdot \Pi_o(2\frac{L}{R}\frac{\theta}{\langle\theta_t^2\rangle}) \qquad (3.39a)$$

4. p87: Eq. (3.36) should be labeled (3.38), and note correction #2.

5. p183: The subscript of the summation sign in Eq. (B.5c) is $i_\ell = 1$.

6. p184: The term a_i in Eq. (B.7a) should read a_{i_1}.

7. p187: Eq. (B.15) should read

$$\square_{n,s,m} = \exp[-2\int_0^{R-R_c} \beta(x)dx]\beta(R-R_c) \sum_{s=1}^{S} \frac{P_s(\pi)}{4\pi} \int_0^{R-R_c} dx_1 \int_0^{x_1} dx_2 \cdots \int_0^{x_{n-1}} dx_n \cdot$$

$$\cdot \int_0^{R-R_c} dx_{n+1} \int_{x_{n+1}}^{R-R_c} dx_{n+2} \cdots \int_{x_{n+m-1}}^{R-R_c} dx_{n+m} \prod_{k=1}^{n+m} \beta(x_k) \cdot \sum_{i_k=1}^{I} a_{i_k}(x_k)\gamma_{f,i_k}(x_k)$$

(B.15)

$$\mathcal{L}_N = \frac{\dfrac{\prod_{i=1}^{N-1} a(u_i)\rho(u_i)}{C_N + \langle\Theta_t^2\rangle D_{N,1}} \int_0^{\psi} \theta d\theta \exp\left\{ - \dfrac{D_{N,1}\theta^2 + E_N\theta_L^2}{C_N + \langle\Theta_t^2\rangle D_{N,1}} \right\} \cdot I_0 \left\{ \dfrac{2\theta\theta_L D_{N,2}}{C_N + \langle\Theta_t^2\rangle D_{N,1}} \right\}}{\dfrac{1}{\langle\Theta_t^2\rangle} \int_0^{\psi} \theta d\theta \exp\left\{ - \dfrac{\theta^2}{\langle\Theta_t^2\rangle} - \left(\dfrac{1}{\langle\Theta_t^2\rangle} + \dfrac{1}{\langle\Theta_b^2\rangle}\right)\theta_L^2 \right\} I_0\left\{ \dfrac{2\theta\theta_L}{\langle\Theta_t^2\rangle} \right\}} \tag{3.36}$$

$$C_N(u_1,\ldots,u_{N-1}) = \left(\frac{R-R_c}{R}\right)^2 \left[\sum_{i=1}^{N-1} \langle\Theta_f^2\rangle u_i \cdot u_i^2 + \sum_{j=1}^{N-2} \sum_{k=j+1}^{N-1} \frac{\langle\Theta_f^2\rangle u_j \langle\Theta_f^2\rangle u_k}{\langle\Theta_b^2\rangle} (u_j - u_k)^2 \right] \tag{3.37a}$$

$$D_{N,M}(u_1,\ldots,u_{N-1}) = 1 + \sum_{i=1}^{N-1} \frac{\langle\Theta_f^2\rangle u_i}{\langle\Theta_b^2\rangle} \left(1 - \frac{R-R_c}{R} u_i\right)^M \tag{3.37b}$$

$$E_N = 1 + \frac{\langle\Theta_t^2\rangle + \sum_{i=1}^{N-1} \langle\Theta_f^2\rangle u_i}{\langle\Theta_b^2\rangle} \tag{3.37c}$$

where $\theta_L = L/R$